

# REPORT DOCUMENTATION PAGE

AFRL-SR-BL-TR-01-

Public reporting burden for this collection of information is estimated to average 1 hour per response, including the time for reviewing instructions, searching existing data sources, gathering the data needed, and completing and reviewing this collection of information. Send comments regarding this burden estimate or any other aspect of this collection of information, including suggestions for reducing this burden, to Washington Headquarters Services, Directorate for Information Operations and Reports (0704-0188), Washington, DC 20540-6001. Respondents should be aware that notwithstanding any other provision of law, no person shall be subject to any penalty for failing to provide any information if it does not have an OMB control number. PLEASE DO NOT RETURN YOUR FORM TO THE ABOVE ADDRESS.

0418

the  
re  
nly

<b>1. REPORT DATE (DD-MM-YYYY)</b> 16-07-2001		<b>2. REPORT TYPE</b> Final Report		<b>3. DATES COVERED (From - To)</b> 01-09-2000 to 30-08-2001	
<b>4. TITLE AND SUBTITLE</b>  Effective Actuation:  High Bandwidth Actuators and Actuator Scaling Laws				<b>5a. CONTRACT NUMBER</b> F49620-00-C-0046	
				<b>5b. GRANT NUMBER</b>	
				<b>5c. PROGRAM ELEMENT NUMBER</b> 65502F	
				<b>5d. PROJECT NUMBER</b> 66STTR	
<b>6. AUTHOR(S)</b> A. B. Cain, G. R. Raman, and E. J. Kerschen				<b>5e. TASK NUMBER</b>	
				<b>5f. WORK UNIT NUMBER</b>	
				<b>8. PERFORMING ORGANIZATION REPORT NUMBER</b> ITAC-TR-1-2001	
<b>7. PERFORMING ORGANIZATION NAME(S) AND ADDRESS(ES)</b>  Innovative Tech. Appl. Co.      Illinois Institute of Tech. P.O. Box 6971                      3300 South Federal Street Chesterfield, MO 63006          Chicago, IL 60616					
<b>9. SPONSORING / MONITORING AGENCY NAME(S) AND ADDRESS(ES)</b> Air Force Office of Sci. Res. 801 N. Randolph St. Arlington, VA 22203-1977				<b>10. SPONSOR/MONITOR'S ACRONYM(S)</b> AFOSR	
				<b>11. SPONSOR/MONITOR'S REPORT NUMBER(S)</b>	
<b>12. DISTRIBUTION / AVAILABILITY STATEMENT</b>  Available for Public Release					
<b>13. SUPPLEMENTARY NOTES</b>					
<b>14. ABSTRACT</b> This final report was developed under STTR AF00T006. The project advances active flow control to enable new Air Force capabilities. Advances in both the development of new actuator hardware and in understanding the flow physics have been achieved. Four key new advances have been achieved in Phase I of this AFOSR/STTR Program. First, a new high power (125-160dB), high bandwidth (factor of 8.6), high dynamic range (15-20 dB), computer automated actuator hardware system has been developed and demonstrated. Second, the first simulations of the powered resonance tube have been completed; these provide new insights into the details of the actuator flow physics. Third, a simplified analytical model of the powered resonance tube has been developed; this provides important design guidance and information on the effects of parametric variations. Finally, breakthrough computational simulations that advance our understanding of the effects of high frequency excitation on turbulent shear layers have been completed. These simulations show that the high frequency excitation reduces turbulent production rate and increases the turbulent dissipation rate to dramatically reduce the turbulent kinetic energy.					
<b>15. SUBJECT TERMS</b> Active Flow Control, Actuators, Powered Resonance Tubes, Acoustics, High Frequency Excitation, Asymptotic Analysis, Direct Numerical Simulation					
<b>16. SECURITY CLASSIFICATION OF:</b>			<b>17. LIMITATION OF ABSTRACT</b>	<b>18. NUMBER OF PAGES</b>	<b>19a. NAME OF RESPONSIBLE PERSON</b> Alan B. Cain
<b>a. REPORT</b>	<b>b. ABSTRACT</b>	<b>c. THIS PAGE</b>			<b>19b. TELEPHONE NUMBER (include area code)</b> (314) 576-1639

AIR FORCE OFFICE OF SCIENTIFIC RESEARCH (AFOSR)  
NOTICE OF TRANSMITTAL DTIC. THIS TECHNICAL REPORT  
HAS BEEN REVIEWED AND IS APPROVED FOR PUBLIC RELEASE  
LAW AFR 190-12. DISTRIBUTION IS UNLIMITED.

<b>TABLE OF CONTENTS</b>	<b>i</b>
<b>ABSTRACT</b>	<b>1</b>
<b>Introduction</b>	<b>2</b>
<b>The DARPA MAFC and Boeing HIFEX Programs</b>	<b>3</b>
<b>Development of the high bandwidth resonance tube</b>	<b>5</b>
<b>Summary</b>	<b>5</b>
<b>The powered resonance tube actuator</b>	<b>5</b>
<b>Order of magnitude variation in frequency</b>	<b>6</b>
<b>Computer controlled high bandwidth actuator</b>	<b>6</b>
<b>Experimental set-up</b>	<b>7</b>
<b>Experimental results</b>	<b>7</b>
<b>Simulations of the powered resonance tube</b>	<b>9</b>
<b>Simulation summary</b>	<b>9</b>
<b>Axisymmetric geometry idealization</b>	<b>9</b>
<b>Pressure (Reynolds Number) scaling</b>	<b>10</b>
<b>Simulation results</b>	<b>10</b>
<b>The wind code</b>	<b>11</b>
<b>Analytical modeling of the powered resonance tube</b>	<b>13</b>
<b>Acoustic field in resonance tube</b>	<b>14</b>
<b>Acoustic field in integration slot</b>	<b>16</b>
<b>Derivation of matching conditions</b>	<b>18</b>
<b>Solution of coupled system</b>	<b>19</b>
<b>Results for PRT resonant frequencies</b>	<b>21</b>
<b>Simulations of high frequency forcing of a plane wake</b>	<b>23</b>
<b>Overview</b>	<b>23</b>
<b>Background</b>	<b>23</b>
<b>Computational approach</b>	<b>25</b>
<b>Results</b>	<b>26</b>
<b>Fully turbulent initial condition</b>	<b>27</b>
<b>Transitional Initial condition</b>	<b>28</b>
<b>Conclusions</b>	<b>29</b>
<b>Acknowledgements</b>	<b>29</b>
<b>List of presentations, papers and publications from this program</b>	<b>30</b>
<b>Conclusions</b>	<b>31</b>
<b>Recommended future work – Jet noise reduction</b>	<b>32</b>
<b>References</b>	<b>33</b>

## List of Tables

**Table 2.1** Success of the look-up table method in achieving a prescribed frequency. The left column provides the prescribed frequency. The frequency obtained at various supply pressures and the percent errors are given in other columns.

**Table 4.1** Rigid-wall resonance tube radial eigenvalues and associated values of the Bessel function.

**Table 4.2** Pressure-release integration slot radial eigenvalues and associated values of the Bessel function.

## List of Figure Captions

**Fig. 2.1** Manually operated powered resonance tube used during the initial stages of our experiments. This apparatus was used to demonstrate the effect of changing the depth of the resonance tube and the "spacing" between the supply jet and the resonance tube.

**Fig. 2.2** Autospectrum from resonance tube at 0.5 inch spacing, 2.75" tube depth and a pressure of 37psi.

**Fig. 2.3** Autospectrum from resonance tube at 0.5in spacing, 1.75" tube depth and a pressure of 37psi.

**Fig. 2.4** Autospectrum from the resonance tube at 0.5in spacing, 1.0" tube depth and a pressure of 37psi.

**Fig. 2.5** Autospectrum from resonance tube at 0.5in spacing, .125" tube depth and a pressure of 37psi.

**Fig. 2.6** Frequency vs. depth for the resonance tube at 0.25" spacing and 37psig pressure.

**Fig. 2.7** Sound Pressure Level (SPL) vs. the depth of the tube at 0.25" spacing and 37 Psig pressure.

**Fig. 2.8** Modified computer controlled powered resonance tube.

**Fig. 2.9** Photograph of the modified powered resonance tube that could be operated by computer control.

**Fig. 2.10** Frequency vs. depth variation at 40 psig and various spacings

**Fig. 2.11** Autospectrum of the resultant sound at 35psig. The spacing was changed as shown in table(2.1-a). (a-d) target frequency = 2.2 kHz. (e-h) target frequency = 12kHz.

**Fig. 2.12** Autospectrum of the resultant sound at 0.22 in spacing (between the supply jet and the resonance tube). The pressure was changed as shown in Table(2.1-b). (a-d) the target frequency = 2.2 kHz. (e-h) target frequency = 12kHz.

**Fig. 3.1** A close-up view of zones 1-3. Supply tube is zone 1 with 101X21 points, zone 2 is the integration slot with 41X101 points, and zone 3 is the resonance tube with 61X21 points.

**Fig. 3.2** The 4 zone grid used for the powered resonance tube simulations. Zone 4 is the far field with 201X101 points. Zones 1-3 as described in Fig. 3.1.

**Fig. 3.3** Pressure contours after 5250 timesteps for case F4-viscous walls.

**Fig. 3.4** Mach contours in the supply tube, integration slot, and resonance tube corresponding to Fig. 3.3.

**Fig. 3.5** Mach contours for case in Fig. 3.4 but after only 3750 timesteps.

**Fig. 3.6** A time series of the pressure in the far field approximately  $\frac{1}{4}$ " from the edge of the integration slot. This very closely approximates the microphone position in the IIT experiments.

**Fig. 3.7** The pressure spectral density from the F4 viscous wall case indicating resonance at approximately 7,600Hz.

**Fig. 3.8** A slip wall simulation comparable to the viscous wall calculation shown in Fig. 3.5.

**Fig. 3.9** A slip wall simulation comparable to the viscous wall calculation shown in Fig. 3.4.

**Fig. 3.10** A slip wall pressure time history corresponding to Fig. 3.6 showing the lack of a sustained resonance.

**Fig. 3.11** An expanded view of the supply tube-integration slot-resonance tube region of Fig. 3.5.

**Fig. 3.12** An expanded view of the supply tube-integration slot-resonance tube region of Fig. 3.4.

**Fig 4.1** Theoretical predictions for the PRT actuator resonance frequency and comparison with IIT data. Tube radius  $a = 0.125$  in., integration slot width  $w = 0.25$  in.,  $p = 37$  psig.

**Fig 4.2** Influence of integration width on the PRT actuator resonance frequency, for slot radius  $s/a = 3$ . Frequency in the absence of an end correction is  $fd/c = 0.25$ .

**Fig. 4.3** Influence of integration slot radius on the PRT actuator resonance frequency, for tube depth  $d/a = 3$ . Frequency in the absence of an end correction is  $fd/c = 0.25$ .

## 1. INTRODUCTION

The Department of Defense, DARPA and the Air Force in particular, are moving future warfighter capabilities forward by application of new technologies. One new technology that offers important new capabilities is Active Flow Control (AFC). One of the most important requirements for the application of AFC is the development of actuators with high bandwidth and authority. This STTR Program has focused on producing new hardware devices with high bandwidth capabilities and strong authority. The hardware advances are complemented by computational simulations and analytical modeling. Together these efforts provide new understanding of the flow physics and guidance for future prototype and production designs of the powered resonance tube.

AFC techniques can basically be separated into two classes. The first class (AFC(I)) involves the use of unsteady forcing to excite instability waves of laminar flows, or the large-scale structures of turbulent flows. AFC(I) techniques have been explored extensively in the past decade. A recent review article that discusses many of these advances is presented by Nishri & Wygnanski (1998). The second class of active flow control techniques (AFC(II)), which have been developed more recently, involves the use of actuators to force turbulent boundary and free-shear layers at high frequencies in the Kolmogorov inertial subrange (see Wiltse & Glezer 1998 and Cain et al. 2001). These two classes of active flow control techniques have different actuator bandwidth requirements, as discussed below.

To effect active flow control across the full operating envelope of an air vehicle, actuators with high bandwidth and large dynamic range are required. To illustrate this, consider the actuator bandwidth requirements for a transonic air vehicle. For the purposes of discussion, assume that the minimum and maximum speeds of interest differ by a factor of eight. We may also assume that the streamwise locations of interest for actuators vary by a factor of 8. An estimate of the variation in boundary layer thickness is required. For laminar boundary layers, the boundary layer thickness  $\delta$  scales with the square root of the downstream distance  $x$  and the inverse square root of the flow speed  $U$ . The thickness  $\delta$  of turbulent boundary layers scales roughly with the  $6/7$  power of the downstream distance  $x$  and the inverse  $1/7$  power of the flow speed  $U$ .

For AFC(I) techniques (which have the most stringent requirements), the actuator must produce an unsteady flow disturbance at a frequency that is near the frequency of the naturally occurring instability waves or large-scale structures. The required frequency scales as  $f \propto U/\delta$ . Thus, for a laminar boundary layer we obtain  $f \propto U^{3/2}x^{-1/2}$ , while for a turbulent boundary layer we obtain  $f \propto U^{8/7}x^{-6/7}$ . Consider an actuator at a fixed location on the vehicle. In order for the actuator to be effective for the first class of AFC techniques over a speed range of 8, a bandwidth range of  $8^{3/2} \approx 23$  would be required for a laminar boundary layer, while a bandwidth range of  $8^{8/7} \approx 11$  would be required for a turbulent boundary layer. In reality, the laminar scaling overestimates the requirement in many situations, since one would anticipate a significant shift in transition location over a speed range of 8. Thus, for AFC(I) techniques, a reasonable estimate for the desired bandwidth range for an actuator at a fixed location is, say 16.

We can also consider the possibility of AFC(I) applications using the same actuator at all locations on a vehicle. In this case the desired bandwidth range increases to 64, for both the laminar and turbulent cases. Presently available mechanical or flow-based actuator designs typically do not possess such a large bandwidth. Thus, for AFC(I) applications we have chosen to focus on the goal of developing an actuator with a bandwidth of 16 and a large dynamic range. The progress achieved in this Phase 1 effort is substantial, and indicates that this goal is within sight.

AFC(II) techniques involve excitation of disturbances in the inertial subrange of the turbulent boundary or free-shear layer. Here the bandwidth requirements are more modest. The instability modes or large-scale structures that are excited in AFC(I) techniques have a fairly narrow frequency band (at a given point in the boundary or free-shear layer). In contrast, the inertial subrange of a turbulent layer typically extends over a frequency range of say, an order of magnitude. It is only necessary to force the turbulent flow at some frequency within this range. Therefore, for AFCII techniques, the possibility of effecting flow control using the same actuator at a variety of locations on a vehicle appears realistic.

The present focus of this STTR is on development of high bandwidth powered resonance tubes. Thus, the important question of what type of actuation can be achieved by application of the powered resonance tube arises. The short history of the powered resonance tube as an actuator points to the obvious answer of applying it to high frequency excitation (AFCII). We believe that the powered resonance tube is currently the most robust actuator type for application to high frequency excitation. However, it must also be remembered that the powered resonance tube produces high acoustic levels. Acoustic excitation has been used by many researchers to directly control instabilities (AFCI) and separation (see Greenblatt & Wygnanski 2000). Therefore we believe that the high bandwidth powered resonance tube actuator has enormous promise as both a high frequency actuator and an instability control actuator (AFCI) with tremendous control authority in both applications.

#### THE DARPA MAFC AND BOEING HIFEX PROGRAMS

DARPA is advancing the application of Active Flow Control (AFC) through the Micro Adaptive Flow Control (MAFC) Program. The present STTR program complements an ongoing Boeing effort that is part of the DARPA MAFC Program. The DARPA/Boeing technology development program is motivated by two possible applications.

The first application is for problems related to Short Take-Off and Vertical Landing (STOVL) aircraft. These problems include lift loss due to suck-down effects, hot gas re-ingestion, ground erosion and sonic fatigue. In addition, high acoustic levels and wall jet flows on aircraft carriers are serious problems for ground personnel. There is a need to develop AFC methods to improve the aerodynamic performance of STOVL aircraft in the ground environment. This includes improvements in aircraft stability and lift optimization, and improvements related to ground impingement properties (fountain location, suck-down and pressure distribution on wings).

The second application is for problems related to weapons release from aircraft internal weapons bays. Current military aircraft use passive suppression (spoilers) for reducing the intensity of the acoustic environment in weapons bays. However, these spoilers are ineffective above Mach 1. The goal of the USAF is to release weapons at speeds above  $M = 1$  since this represents a tactical advantage in combat. Boeing is focused therefore on developing active flow control techniques for cavities that are effective at  $M > 1$ .

The powered resonance tube shows great promise as an AFC actuator for applications such as these. Initial demonstrations of its effectiveness in Class II AFC applications have been carried out at IIT, Boeing Saint Louis and DERA (UK). The integrated multiple actuator systems used in conjunction with the high frequency idea was applied to high speed impinging jets at Boeing Saint Louis. Unlike traditional Class I AFC methods that can suppress some tones but enhance others, the present technique has the ability to suppress all tones. Other Class II AFC experiments were performed at DERA (Defense Evaluation and Research Agency, UK) to demonstrate the success of this technique in suppressing cavity tones (see Stanek et al. 2000, 2001).

The present Phase 1 STTR Program has advanced the capabilities of powered resonance tubes and provided insights into the physics of their operation. This work will benefit numerous DoD applications in the coming years. The Phase 1 hardware development and experiments have demonstrated that a single actuator can provide a frequency bandwidth of an order of magnitude with 15-20dB of dynamic range. The simulations of the powered resonance tube have identified important flow details that may significantly impact actuator performance. The analytical work has provided a tool for predicting the resonance frequencies and their dependence on actuator geometry. Together, these advances provide important information for guiding the development of more effective actuators. Finally, direct numerical simulations of high frequency forcing have given new insights into the physics and scaling laws for the application of the second class of AFC techniques. The following sections of this report provide more detail on these important advances in actuator physics and technology development.

## 2. DEVELOPMENT OF THE HIGH BANDWIDTH RESONANCE TUBE

### SUMMARY

This section describes the development of a computer controlled high bandwidth resonance tube device. Adaptive high bandwidth actuators are required to adapt to changes in flow speed and conditions during flight. Our approach consisted of first selecting a candidate actuator and then devising a method to extend its bandwidth. Our search for an actuator revealed that excitation devices that produced high amplitude signals generally leveraged a resonance mechanism. For example, piezo elements mounted on structural members and devices that exhibited aeroacoustic resonance. The former type of actuator (piezo) was considered briefly but was dropped in favor of the latter type (aeroacoustic). The actuator selected for bandwidth enhancement was the Powered Resonance Tube (PRT) actuator. This device is capable of producing high frequency and high amplitude oscillations. The frequency produced depends primarily on the quarter wavelength frequency of a tube that is closed at one end. First, we demonstrated that high bandwidth could be produced by manually varying the depth of the PRT. This was followed by a more refined effort using a computer controlled mechanism that varied the depth of the tube in response to user selected frequencies. We were successful in obtaining an order of magnitude variation in frequency over a wide range of amplitudes.

### THE POWER RESONANCE TUBE ACTUATOR

The resonance tube phenomenon was first described by Hartmann in 1918. The Hartmann whistle apparatus consists of a jet aimed at the open end of a tube closed at the other end. There are two phases during the operation of this device. In the first phase, the jet penetrates the tube and compresses the air within the tube. In the second phase the compressed air in the tube empties itself. Thus the cycle perpetuates itself. Following earlier efforts at Boeing our goal is to use the oscillatory pressures and velocities produced by this device to design a high bandwidth actuator. Examples of possible applications include the high frequency excitation for suppression of flow induced resonance in weapons bay cavities (see Raman et al. (2000) and Stanek et al. (2000)) and jet-ground impingement tones in STOVL aircraft.

The phenomena associated with such resonance tubes has been studied by several researchers include (Thompson 1992), (Brocher & Duport 1988), and (Brocher 1970). (Iwamoto 1990) and Iwamoto & Dekker 1985) studied a variation of the Hartmann tube known as the Hartmann-Sprenger tube. The resonance frequency was proposed by Brocher (1970) to be equal to approximately the acoustic frequency  $f = a/(4L + \Delta O)$ , Where  $f$  is the resonance frequency,  $L$  is the length of the tube, and  $\Delta O$  is the end correction factor. Note that the frequency of excitation produced by this device depends primarily on its depth. Secondary factors that can alter frequency include the nozzle pressure ratio of the supply nozzle and the spacing between the jet exit and the open end of the resonance tube. (Brocher 1987) derived the maximum amplitude using linear acoustic theory to be  $(\Delta p_{\max} = 2 \cdot k \cdot M \cdot p_a)$ , where  $k$  is the specific heat ratio,  $p_a$  is the ambient pressure, and  $M$  is the jet mach number.

## ORDER OF MAGNITUDE VARIATION IN FREQUENCY

The primary goal of our work was to develop a high bandwidth actuator for use with active flow control systems. Adaptive high bandwidth actuators are required to adapt to changes in flow speed and conditions during flight. Raman et al. (2000) and Stanek et al. (2000) have shown that such high frequency actuators with no moving parts are very effective in the suppression of flow impingement and cavity noise. However, fixed geometry actuators can only produce effective actuation over a small range of frequencies. This poses a problem because we require a new actuator every time there is a change in geometric or fluid dynamic parameters. Based on these results, our idea is to use a variable depth powered resonance tube actuator where the depth of the resonance tube changes the frequency, and the distance between the supply jet and the resonance tube as well as the supply pressure alter the sound pressure level. All of these parameters were varied in the present experiment.

## COMPUTER CONTROLLED HIGH BANDWIDTH ACTUATOR

Our actuator consists of a modified Hartmann tube that incorporates a resonance tube of variable depth and a variable gap between the supply jet and resonance tube. Earlier work done by Raman et al. (2001) with various fixed depth resonance tubes had determined the approximate lower and upper frequency bounds of such a device. Our high bandwidth actuator consisted of a jet aimed at a hollow tube (open from both ends) that was fitted with an air-tight piston. The piston could be moved to change the depth and in turn the frequency. Tube depths variations from 3/6" to 6" produced frequency changes from about 14 kHz to 500 Hz. The final stage of our development was to control the depth and jet to resonance tube spacing using a computer controlled traverse mechanism. Our present results demonstrate that on prescribing a frequency (at a fixed supply jet nozzle pressure ratio) the computer automatically adjusts the depth and tuning parameter to produce a high amplitude disturbance at a frequency close to that prescribed.

A Visual BASIC program was written in order to implement the look-up table database. The resonance tube database consisted of measured frequencies at various depths. The frequency was measured for depths ranging from 0.1" to 0.4" in steps of 0.05." From a depth of 0.4" to 1.1" a depth increment of 0.1" was used. The spacing between the supply jet and the resonance tube was varied from 0.1" to 0.7" in steps of 0.1." The data base covered a pressure range from 27.5-42.5psig in 2.5psig increments. Thus, we had 686 data points describing the behavior of the resonance tube at various depths, spacings and pressures.

This database is then used to generate a look up table program for controlling the resonance tube such that the desired frequency is obtained at the highest amplitude. The traversing mechanism was calibrated before the look up table program was run. When a desired frequency is input to the program it calculated the depth and moved the piston to the appropriate depth. Using this method, it was found that the error at low frequencies was small (0.5%) while the error at high frequencies was larger (5%) over the range of frequencies from 2.5 to 12 kHz.

Other ideas examined included a tapered piston within the tube that allowed for higher frequencies to be produced by the device. For example, with the tapered piston the highest frequency increased from 12.5 kHz (flat end piston) to 13.5 kHz (tapered end piston) for a tube depth of 0.1". A 1/8" diameter tube was also tested to demonstrate that the high bandwidth actuator can also operate at lower mass flow rates. Note that in most applications the mass flow rate is of concern because excessive mass flows can make this actuator unattractive for practical applications.

#### EXPERIMENTAL SETUP

The experimental set-up of the device shown in Fig. 2.1, consists of a 1/4" diameter jet with a chamfered exit facing the open end of the resonance tube that is closed at the other end. Note that the chamfer was necessary for the production of high amplitude oscillations. A piston fitted inside the tube changes the tube depth. The piston has an O-ring built in to prevent leakage of air. This setup was used as a prototype to test the parameters of the powered resonance tube. The jet is fixed, while the tube part is free to move in the direction of the jet axis. The distance between the jet and the tube (gap), referred to as the "spacing parameter" or "spacing" was changed to see its effect on both the frequency and the amplitude of the sound. The position of the piston inside the tube changes the depth of the tube. Microphone and pressure sensor located at various locations in the vicinity of actuation were used to measure the frequency and amplitude of the fluctuations produced by this device and the power spectrum of the acoustic signal was computed at various depths and spacings. A computer controlled traversing mechanism moves both the piston (for changing depth) and the supply jet for changing the spacing (for tuning). We then generated a detailed experimental database that was used as a lookup table for our computer controlled experiment.

#### EXPERIMENTAL RESULTS

Our first efforts involved using the apparatus shown in Fig. 2.1 and changing the depth of the resonance tube manually from 2.75" to 0.125" by pushing the piston in.

Figures 2.2-2.5 show time averaged microphone spectra for resonance tubes of lengths 2.75", 1.75", 1", and 0.125". For all cases the supply pressure was 37 psig and the spacing parameter was 0.5". Note the change in frequency from about 1.6 kHz to about 14 kHz (approximately one order of magnitude). A summary of a similar set of data (but with a spacing parameter of 0.25") is shown in Figs. 2.6 and 2.7. Note that the frequency could be changed from 14 kHz to about 1.6 kHz and amplitude varied from 125 dB to 160 dB. A decrease in frequency from 14 KHz to 7 kHz resulted in a corresponding amplitude increase from 125 to 160 dB. Further decrease in frequency did not increase amplitude. When the frequency was lowered further from 7 to 2 kHz the amplitude decreased from 160 to 152 dB.

Figures 2.8 and 2.9 show the set-up for the computer controlled tube depth variation experiment. In the photograph the L shaped piece on the left is the supply jet and the microphone is attached to the resonance tube. The rod protruding from the resonance tube provided the depth variability. The bandwidth capability is demonstrated for various jet to resonance tube spacings at 40 P<sub>ig</sub> operating pressure in Fig. 2.10. The quarter wavelength frequency curve and a data point from the simulations of Cain are shown for

comparison. In addition to demonstrating the frequency bandwidth (1.5 to 15 kHz). Fig. 2.10 shows frequency jumps that occur under certain conditions. Through Figs. 2.11 and 2.12 we demonstrate the computer controlled high bandwidth actuator. For the data in Fig. 2.11 the supply pressure was held constant at 35 psig. The red line shown at the top of each column denotes the prescribed frequency. The spectra below the red lines are the experimentally obtained data using the look up table. A frequency of 2.2 kHz (or 12kHz, right hand column) was input to the computer. Data are shown for various spacing parameters. As shown in Table 2.1 the error in obtaining the prescribed frequency is 0.45% for 2.2 kHz and 6.67% for 12kHz. In Fig 2.12 similar data are shown for a constant spacing parameter (0.22") and various supply pressures. Based on these results, our idea is to use a variable depth powered resonance tube actuator where the depth of the resonance tube changes the frequency, and the distance between the supply jet and the resonance tube changes the sound pressure level. And both of these parameters can be controlled actively during the experiment

In many situations the actuator frequency did not change smoothly with change in piston location. In some cases frequency jumps were observed and in other case two dominant frequencies were observed. In addition, at very small depths (0.1") the device did not produce a tone.

#### NOTES ON THE APPENDIX

The appendix provides a detailed compilation of data obtained during this effort. Frequencies and amplitudes produced at various supply pressures and for various resonance tube depths and spacings (supply jet to resonance tube) are tabulated. Regions shaded yellow in the tables represent situations where frequency does not vary with change in tube depth or situations where frequency jumps occur. Figures A1 to A2 document the set-up. Figures A4 to A15 are sound pressure level maps under various operating conditions. A point worth noting is that as the pressure increases, the high amplitude tone regions gets larger. Figures A16 to A23 depict the bandwidth obtained for various operating conditions. The quarter wavelength frequencies are also plotted for comparison. Finally, Figs. A24 to A37 document microphone spectra for various cases.

### 3. SIMULATIONS OF THE POWERED RESONANCE TUBE

The first simulations of the powered resonance tube have been performed as part of our effort to better understand powered resonance tube behavior.

#### a. SIMULATION SUMMARY

Scaled simulations of the powered resonance have been performed with remarkable correspondence to laboratory experiments (see Fig. 2.10) in terms of the frequency (simulated at 7.6 kHz) and amplitude (a simulation value of 163dB) of their resonant response. New insights into the complexity and flowfield details are suggested. The simulations show that the flow in the integration slot is primarily on the resonance tube side with almost no flow on the supply tube side of the integration slot. The preliminary indications suggest that the acoustic waves from resonance in the resonance tube drive an unsteady separation at the supply tube. The unsteady separation at the supply tube in turn drives the observed large oscillations in the shock structure. The unsteady separation seems to be a key aspect of the resonance phenomena. These behaviors should be considered speculative and challenges remain to gain certainty in understanding the governing mechanisms.

#### b. AXISYMMETRIC GEOMETRY IDEALIZATION

The geometry fabricated in the laboratory has a number of complexities that would require an unreasonably large grid and enormous computational resources to simulate. The ability to do meaningful simulations requires simplifying approximations to reduce the computational resource requirements. The first such approximation is to assume an axisymmetric geometry and flowfield.

The basic geometry for the computation consists of a supply tube feeding the integration slot and resonance tube and then an axisymmetric far field. The supply begins with a  $\frac{1}{2}$ " diameter at the reservoir end that tapers conically to a  $\frac{1}{4}$ " diameter constant section and then a brief flare into the integration slot. The length of the conical section is  $\frac{1}{2}$ " and the constant diameter section is also  $\frac{1}{2}$ " long.

A look at the grid for supply tube, integration slot, and resonance tube is given in Fig. 3.1. The grid in the supply tube, integration slot, and resonance tube has nominally square cells roughly 0.00625" on a side. The lower left horizontal region is zone 1 and the supply tube. The vertical segment is the integration slot and zone 2. At the upper boundary between zones 1 and 2 the chamfer in the supply tube is evident. It will play an important role in the resonance phenomena. The right horizontal segment is the resonance tube and is zone 3. The full grid for these calculations is given in Fig. 3.2, the upper region is for farfield propagation and is zone 4. The cells in the farfield region expand from these small cells 0.00625" on a side to roughly 0.1" on a side. This means acoustic waves have roughly 280 cells per wavelength in the supply tube, integration slot, and resonance tube and at least 16 cells per wavelength at the far edges of the outer grid. Grid refinement and algorithm studies suggest the present results are invariant to grid and algorithm for modest changes.

### c. PRESSURE (REYNOLDS NUMBER) SCALING

The simulations are focused on approximating the experimental case (examined at IIT by Dr. Ganesh Raman) of a 40 psig supply pressure. Since this supply tube ultimately vents to atmospheric conditions we can expect the supply tube to contain choked flow. To reduce the computational requirements the simulated freestream pressure is reduced to 0.03 psia. The ratio of the supply pressure to the freestream pressure is in exactly the same ratio as the laboratory study. The net effect of this scaling of the pressure is to reduce the effective Reynolds number by a factor of 490. The reduced Reynolds number permits a direct numerical simulation with a more modest grid. This scaling results in a number of grid points that permits complete numerical solutions and post processing of a single case to be completed in about one week using a 500MHz desktop PC. Simulations at the laboratory conditions would require a grid with 490 times as many points in two dimensions and the simulation times would increase by a factor of  $10^4$ . Solutions are obtained using the WIND code described in a later subsection.

The effects of the reduced Reynolds number on the physics of the flow must be estimated. We can begin by considering the impulsively started flow with an infinite flat plate. In this idealized problem the thickness of the boundary layer scales with  $\sqrt{4\nu t}$ . If viscous effects are minimal then the viscous diffusion length will be much less than the radius of the supply tube, this can be stated as  $l_{diff} \ll R$ . When we consider the length of the supply tube we can estimate a convective time scale  $\tau$ . This time scale results in a free diffusion length that would exceed the radius of the supply tube. Such a scaling is overly conservative as the development of the boundary layer in a tube results in an acceleration that slows the development of the boundary layer. Another way we can use such an estimate is to determine how long the simulation can be run before boundary layer becomes significant relative to the supply tube radius. Noting that the effective choked flow kinematic viscosity is  $\nu \approx 0.0775 \text{ ft}^2/\text{sec.}$ , we find that at the time step we are using (0.7 e-07 sec.) we can compute for 9,826 times steps before free viscous diffusion is comparable to the tube radius. As we have stated this is an overly conservative approximation for flow in a tube, but we consider only the first 10,000 timesteps a reasonable approximation. In this 10,000 timesteps we have over 7 supply tube flow through times and over five cycles of the fundamental resonance.

### d. SIMULATION RESULTS

The simulation of the powered resonance tube is made more efficient by the scaling concepts discussed above. A typical sound radiation field is characterized by the pressure far field as shown in Fig. 3.3. The simulation shown in Fig. 3.3 is based on viscous no-slip boundary conditions which will be shown to be quite important. The field in Fig. 3.3 is a snapshot after the calculation has advanced 5,250 timesteps. At this point in the calculation the field has advanced approximately 3 periods of the basic 7.6 kHz resonance. It should be noted that in the first wavelength (approximately  $1\frac{3}{4}$ " ) from the integration slot there are significant asymmetries present. As the pressure wave moves into the farfield the evolution becomes more nearly symmetric. A more detailed perspective of the source field is given by Mach contours in the supply tube-integration

slot-resonance tube shown at 5,250 timesteps in Fig. 3.4. There are two major points from Fig. 3.4, first note that the flow in the integration slot is almost entirely confined to a narrow channel up the wall on the resonance tube side. This feature is present in all snapshots examined. The second important point is the shock structure that proceeds almost all the way across the integration slot. The shock structure infacts oscillates back and forth across the integration slot. These points are reinforced in Fig. 3.5, a snapshot at 3,750 timesteps, which again shows the confinement of the flow up the integration slot wall and that the supersonic region is less than half way across the integration slot at this point in time. During the course of these simulations the supersonic region is observed to vary in extent from as far as  $7/8$  of the distance across the integration slot and as little as  $1/4$  of the distance across the integration slot.

The periodic nature of the flow and acoustic field is given by a pressure measurement taken at the bottom of zone 4 about  $1/4$ " from the edge of the integration slot as was done in the laboratory measurements at IIT. Figure 3.6 shows the time history of the pressure and its basic periodic nature. The degree to which this field is periodic, is driven home by the pressure spectral density plot shown in Fig. 3.7.

An alternative problem formulation using slip wall boundary conditions was executed to gain further insight into the physics of this problem. Figure 3.8 shows the Mach contours after 3,750 timesteps as did Fig. 3.3. The main differences between Figs. 3.3 and 3.8 have to do with the flow attaching to the supply tube chamfer in 3.8 and also a smaller supersonic flow region in 3.8. Figure 3.9 is the slip wall comparison to the no-slip Fig. 3.2 after 5,250 timesteps. Note that again the slip wall case (3.9) remains attached to the end of the chamfer and also the supersonic region is shorter. In fact the slip wall flow remains attached to the edge of the chamfer and this seems to limit the oscillations of the shock system. This is somewhat speculative but Fig. 3.10 of the corresponding slip wall pressure time history shows the lack of a regular periodic response. Figures 3.11-12 show an expanded view of the chamfer region and suggest an oscillating chamfer separation in the no-slip case. We thus speculate that the unsteady chamfer separation is driven by the acoustic resonance and the unsteady separation in turn drives the unsteady shock system thus closing the loop. It is observed during this resonance cycle that the separation on the chamfer can occur as early as  $1/4$  of the chamfer distance or remain attached to the end of the chamfer.

#### e. THE WIND CODE

These simulations were performed using the flow solver WIND. WIND is a general purpose Euler and Navier-Stokes solver. WIND is available to the public through the NPARC consortium (lead by NASA GRC and AEDC) and operates in two or three dimensions with structured (patched and overlapping) and unstructured grids. Any valid grid can be utilized, Wind places no restrictions on the point or slope discontinuities at zone interfaces. A mature zone coupling technique, in production since 1985, ensures continuity of the solution across zone boundaries. Wind has a library of boundary condition routines available on a point-by-point basis.

WIND has been used for flows from nearly incompressible speeds ( $M \sim 0.05$ ) to hypersonic. It solves any subset of the full Reynolds averaged Navier-Stokes equations or time accurate laminar Navier-Stokes equations.

Wind incorporates a number of user-selectable (by zone) solution algorithms. The default time integration scheme is a first order, approximately factored implicit scheme. For inviscid flows (or, under the thin layer approximation, for directions with no viscous terms) the implicit operator is diagonalized, providing a significant speed-up. Explicit Runge-Kutta third order time integration is used in the present time accurate calculations.

The default explicit spatial operator is a second-order (in the physical domain) Roe flux difference split scheme. The standard upwind operator has been replaced by an upwind biased stencil, which improves the stability of the upwind scheme and reduces numerical dissipation. For the present simulations a fifth order (one cell upwind biased) spatial scheme is used. Based on the paper by Cain & Bower 1995 this scheme was selected as the best available in WIND for acoustic propagation problems. The paper by Cain et al. 1998 successfully applies the capabilities of the WIND code to the receptivity problem with a good match to results from linear theory.

Wind dynamically allocates memory on a zonal basis, minimizing computer hardware requirements. Distributed parallel processing is available utilizing PVM, NX or MPI message passing protocols. A keyword input interface and extensive defaults simplify Wind operation. Most Wind options may be controlled zonally allowing the user to balance the accuracy and cost of each solution.

Wind has been written in standard FORTRAN-90 and ports easily to most computer platforms. Wind is currently operational on Cray, Convex, VAX, Silicon Graphics, Hewlett Packard, Sun, Intel, and IBM platforms.

#### 4. ANALYTICAL MODELING OF THE POWERED RESONANCE TUBE

The objective of this analysis is to predict the resonant frequencies of the Powered Resonance Tube (PRT) actuator, as a function of the geometry. In particular, we wish to account for the influence of the integration slot. This effect becomes particularly important for small tube depths, as illustrated by the experimental data presented in Section 2.

PRT actuators involve unsteady nonlinear oscillations of high-speed flows, and a full analytical description of the complete phenomenon is beyond reach. However, there is a definite need to be able to predict the frequencies of operation of these devices, and to understand the influence of geometric parameters on the resonance frequencies. The analytical model presented in this section is a first step in this direction.

We consider linear acoustic motion in an axisymmetric geometry, consisting of a rigid-wall resonance tube of radius  $a$  and depth  $d$ , connected to an axisymmetric integration slot of radius  $s$  and width  $w$ . A polar cylindrical coordinate system  $(x, r, \theta)$  is utilized. The geometry is axisymmetric about the  $x$ -axis, and the origin of the coordinate system is placed at the center of the planar interface between the resonance tube and the integration slot. The resonance tube has a (rigid) closed end at  $x = d$ . The integration slot is assumed to have a rigid wall at  $x = -w$ , and a wall at  $x = 0$  that is also rigid except for the circular opening of radius  $a$  that connects the integration slot to the open end of the resonance tube. The outer edge of the integration slot at  $r = s$  is open. The exterior geometry consists of a rigid surface at  $r = s$ , i.e. the open edge of the integration slot is considered to have an infinite flange.

It may seem overly simplistic to neglect the mean flow in the integration slot of the PRT actuator. However, while the mean flow plays an important role in determining the resonance amplitude, the experimental data shows that the resonance frequency is determined primarily by the resonance tube length when  $d/a \gg 1$ . This is not unexpected, as resonance frequencies are generally determined by the ratio of the system compliance to the system mass, and for long tubes the primary compliance and mass of the system are associated with the fluid in the resonance tube. Thus, the standard quarter-wavelength formula for an open-closed resonance tube provides an adequate prediction of the resonance frequency when  $d/a \gg 1$ . However, the quarter-wavelength formula becomes increasingly inaccurate as the tube length is decreased, since the compliance and mass of the fluid in the integration slot becomes an increasingly important part of the system compliance and mass. The objective of the present modeling is to incorporate the compliance and mass of the fluid in the integration slot into the prediction of the resonance frequencies of the system.

In the actual PRT geometry, the wall of the integration slot at  $x = -w$  opens to the nozzle of the driving jet through which the mean flow enters the device. When the mean flow is neglected, an assumption must be made concerning the representation of this feature. For the strong resonance conditions of interest, the mean flow entering the integration slot through this nozzle is typically sonic or supersonic. In this situation, the choked flow

prevents acoustic waves from propagating back upstream into the nozzle of the driving jet. The rigid wall assumption at  $x = -w$  appears to be a reasonable approach to account for this feature of the physics.

The basic approach utilized in the analysis is to connect together series representations in the two separate regions: the resonance tube and the integration slot. First, we obtain a series representation for the acoustic field in each region. These two series representations satisfy the wave equation, and the boundary conditions associated with the rigid walls at  $x = d$  (resonance tube) and at  $x = -w$  (integration slot). The radial eigenfunctions for the resonance tube satisfy the rigid-wall boundary condition at  $r = a$ , while the radial eigenfunctions for the integration slot satisfy the pressure-release boundary condition at  $r = s$ . Each series contains an infinite number of undetermined coefficients, say  $D_m$ ,  $m = 0, 1, 2, \dots, \infty$  for the resonance tube, and  $S_n$ ,  $n = 1, 2, 3, \dots, \infty$  for the integration slot. These undetermined coefficients are associated with the (unknown) pressure field that exists in the vicinity of the interface ( $x = 0$ ) between the resonance tube and the integration slot.

An infinite set of linear algebraic equations for the coefficients  $D_m$  and  $S_n$  are obtained by equating the two series representations for the acoustic pressure field at  $x = 0$ . A second infinite set of linear algebraic equations for the  $D_m$  and  $S_n$  are obtained by equating the two series representations for the axial gradient of the acoustic pressure field at  $x = 0$ . Together, the two sets of equations are adequate to determine the unknown coefficients. The system of equations is homogeneous, so that a non-trivial solution exists only when the associated matrix is singular. This is the condition that determines the resonant frequencies of the system.

### ACOUSTIC FIELD IN THE RESONANCE TUBE

The acoustic field in the resonance tube satisfies the three-dimensional wave equation. Assuming time-harmonic motion, the (axisymmetric) pressure field can be written in the form

$$p'(x, r, t) = p(x, r) \cos \omega t.$$

The reduced pressure  $p(x, r)$  then satisfies the Helmholtz equation

$$\frac{\partial^2 p}{\partial x^2} + \frac{1}{r} \frac{\partial}{\partial r} \left( r \frac{\partial p}{\partial r} \right) + k^2 p = 0, \quad (1)$$

where  $k = \omega / c$  and  $c$  is the speed of sound. The solution to the Helmholtz equation can be obtained by separation of variables, in which the partial differential equation in two independent variables is converted to two ordinary differential equations, one for the radial dependence and one for the axial dependence. The radial equation is the Bessel equation of order 0, while the axial equation is a second-order equation with constant coefficients.

The solution of the radial equation that satisfies the condition of boundedness at  $r = 0$  is the Bessel function of the first kind,  $J_0$ . The separation constant (or radial eigenvalue) is

then obtained by applying the rigid-wall boundary condition at the tube wall,  $\partial p / \partial r = 0$  at  $r = a$ . There are an infinite number of radial eigenvalues, so that the solution for  $p(x, r)$  is an infinite series.

The solution to the axial equation contains two arbitrary constants, one of which is determined by the rigid-wall boundary condition at the tube end,  $\partial p / \partial x = 0$  at  $x = d$ . The solution to the axial equation takes on different forms, depending on whether the given mode is 'cut on' (and propagates without attenuation), or 'cut off' (and decays exponentially in the direction of propagation). For conditions of interest in the PRT actuator, only the  $m = 0$  'plane-wave' mode is cut on in the tube. All higher modes are cut off.

Taking these features into account, the acoustic pressure field in the resonance tube is given by the infinite series

$$p(x, r) = D_0 \cos k(x - d) + \sum_{m=1}^{\infty} D_m J_0(\gamma_m r / a) \frac{\cosh \tau_m (x - d)}{\cosh \tau_m d}, \quad (2)$$

where

$$\tau_m = \sqrt{(\gamma_m / a)^2 - k^2}.$$

The resonance tube modal coefficients  $D_m$ ,  $m = 0, 1, 2, \dots, \infty$  remain undetermined at this stage. The  $\gamma_m$  are the rigid-wall radial eigenvalues, which satisfy the transcendental equation  $dJ_0(z)/dz = 0$ . The first few rigid-wall radial eigenvalues are (Abramowitz & Stegun 1972, p. 411)

$m$	$\gamma_m$	$J_0(\gamma_m)$
0	0	1
1	3.8317	-0.4028
2	7.0156	0.3001
3	10.1735	-0.2497
4	13.3237	0.2184
5	16.4706	-0.1965

Table 4.1. Rigid-wall resonance tube radial eigenvalues and associated values of the Bessel function.

Note that the leading term on the right-hand side of Eq. (2) is the 'plane wave' mode of the resonance tube, corresponding to  $\gamma_0 = 0$ .

The axial pressure gradient at the interface plane is also required in our analysis. Differentiating Eq. (2) and setting  $x = 0^+$ , we have

$$\left. \frac{\partial p}{\partial x} \right|_{x=0^+} = k D_0 \sin kd - \sum_{m=1}^{\infty} \tau_m D_m J_0(\gamma_m r / a) \tanh \tau_m d. \quad (3)$$

Equations (2) and (3) are valid for frequencies below the cut-on frequency of the  $m = 1$  mode,  $\omega_{cr,1} = ck_{cr,1} = \gamma_1 c/a$ . To compare with the experiments performed by Raman at IIT, consider a tube of radius  $a = 1/8$  in and a speed of sound  $c = 1130$  ft/sec. We then have  $\omega_{cr,1} = 4.16 \times 10^5$  rad/sec, or  $f_{cr,1} = 66$  kHz. This frequency is well above the frequency range for the experiments, so that the only propagating mode in the resonance tube was the  $m = 0$  plane-wave mode, as assumed in deriving Eqs. (2) and (3).

#### ACOUSTIC FIELD IN THE INTEGRATION SLOT

The acoustic field in the integration slot is analyzed using an approach very similar to that for the resonance tube. The primary difference in the analysis is the boundary condition at the outer edge of the integration slot, where we assume a 'pressure release' surface,  $p = 0$  at  $r = s$ . In actuality, the three-dimensional acoustic motion in the vicinity of the outer edge of the integration slot leads to an 'end correction' of  $O(w)$ , so that the effective radius  $s_{eff}$  of the integration slot is slightly larger than the geometric radius  $s$ . For slot widths small compared to the slot radius ( $w/s \ll 1$ ), the numerical value of the end correction can be obtained by considering low-frequency theory for a two-dimensional geometry. Since this particular detail is not crucial for the present investigation, we assume that the value of  $s$  includes this end correction, and apply the boundary condition  $p = 0$  at  $r = s$ .

The separation of variables procedure follows along the same lines as for the resonance tube, except that the separation constant (or radial eigenvalue) is found by applying the boundary condition  $p = 0$  at  $r = s$ . The acoustic pressure field in the integration slot is then given by the infinite series

$$p(x, r) = \sum_{n=1}^{\infty} S_n J_0(\zeta_n r/s) F_n(x). \quad (4)$$

The integration slot modal coefficients  $S_n$ ,  $n = 1, 2, 3, \dots, \infty$  remain undetermined at this stage. The  $\zeta_n$  are the pressure-release-wall radial eigenvalues, which satisfy the transcendental equation  $J_0(z) = 0$ . The first few pressure-release-wall radial eigenvalues are (Abramowitz & Stegun 1972, p. 409)

$n$	$\zeta_n$	$J_1(\zeta_n)$
1	2.4048	-0.5191
2	5.5201	0.3403
3	8.6537	-0.2715
4	11.7915	0.2325
5	14.9309	-0.2065

Table 4.2. Pressure-release integration slot radial eigenvalues and associated values of the Bessel function.

The axial function  $F_n(x)$  takes different forms for cut-on modes ( $k > \zeta_n/s$ ) and cut-off modes ( $k < \zeta_n/s$ ). These forms are

$$F_n(x) = \begin{cases} \cos \sigma_n(x+w), & k > \zeta_n/s \\ \frac{\cosh \sigma_n(x+w)}{\cosh \sigma_n w}, & k < \zeta_n/s \end{cases}$$

where

$$\sigma_n = \begin{cases} \sqrt{k^2 - (\zeta_n/s)^2}, & k > \zeta_n/s \\ \sqrt{(\zeta_n/s)^2 - k^2}, & k < \zeta_n/s \end{cases}$$

The rigid-wall boundary condition  $\partial p / \partial x = 0$  at  $x = -w$  has been applied in deriving these expressions. The somewhat asymmetric forms of  $F_n(x)$  for the cut-on and cut-off cases have been chosen so that in each case the maximum value of  $F_n(x)$  is one.

The axial pressure gradient at the interface plane is also required in our analysis. Differentiating (4) and setting  $x = 0^-$ , we have

$$\left. \frac{\partial p}{\partial x} \right|_{x=0^-} = \sum_{n=1}^{\infty} S_n J_0(\zeta_n r/s) F_n'(0) \quad (5)$$

where

$$F_n'(0) = \begin{cases} -\sigma_n \sin \sigma_n w, & k > \zeta_n/s \\ \sigma_n \tanh \sigma_n w, & k < \zeta_n/s \end{cases}$$

The boundary between cut-off and cut-on behavior for the  $n$ -th mode in the integration slot is  $\omega_{cr,n} = ck_{cr,n} = \zeta_n c/s$ .

In the experiments performed by Raman at IIT, the geometry of the integration slot is rectangular rather than axisymmetric, and the resonance tube is located off center. Hence, a precise comparison with these experiments cannot be made. However, an approximate comparison is worthwhile. In the IIT geometry, the distance from the center of the resonance tube to the edge of the integration slot varies with azimuthal position, over a range  $0.25 \text{ in} \leq s \leq 0.707 \text{ in}$ . Consider a mid-range value,  $s = 0.5 \text{ in}$ . Using a speed of sound  $c = 1130 \text{ ft/sec}$ , the cut-on frequencies for the first two radial modes in the integration slot are  $\omega_{cr,1} = 6.52 \times 10^4 \text{ rad/sec}$  and  $\omega_{cr,2} = 1.50 \times 10^5 \text{ rad/sec}$ , or  $f_{cr,1} = 10.4 \text{ kHz}$  and  $f_{cr,2} = 23.8 \text{ kHz}$ . The experiments at IIT involved resonance frequencies in the range  $2 \text{ kHz} \leq f \leq 14 \text{ kHz}$ . Thus, the transition from cut-off to cut-on behavior for the  $n=1$  integration slot mode occurs slightly above the center of the frequency range of the experimental data, while the higher-order integration slot modes ( $n \geq 2$ ) are cut-off across the full frequency range of the experimental data. Since the critical frequencies depend on the value of  $s$ , which was not uniform in the IIT experiments, some differences in behavior between the analytical model and the experiments should be expected, particularly in the vicinity of the critical frequency  $f_{cr,1}$ .

## DERIVATION OF THE MATCHING CONDITIONS ACROSS THE INTERFACE

At this stage, the modal coefficients  $D_m$  for the acoustic pressure field in the resonance tube and the modal coefficients  $S_n$  for the acoustic pressure field in the integration slot are both unknown. Relationships between these modal coefficients are obtained by applying the matching conditions at the planar interface between the resonance tube and the integration slot ( $x = 0$ ). The quantities to be matched are the pressure field  $p$  and the axial pressure gradient  $\partial p / \partial x$ . This matching process also guarantees the continuity of higher-order derivatives, since the Helmholtz equation (1) provides an expression for the second-order derivatives of the pressure field in terms of the pressure field itself.

First consider the axial pressure gradient at  $x = 0$ . For the resonance tube, the axial pressure gradient  $\partial p / \partial x|_{x=0^+}$  at the interface is defined for the region  $0 < r < a$  by Eq. (3). For the integration slot, the axial pressure gradient  $\partial p / \partial x|_{x=0^-}$  is defined for the region  $0 < r < s$  by Eq. (5). These two expressions must be equal for the region  $0 < r < a$ , while for the region  $a < r < s$  the integration slot has a rigid wall and the axial pressure gradient (5) must vanish. For the resonance tube, the region  $a < r < s$  is out of the physical domain and therefore not of interest. Thus we have

$$\sum_{n=1}^{\infty} S_n J_0(\zeta_n r / s) F_n'(0) = \begin{cases} k D_0 \sin kd - \sum_{m=1}^{\infty} \tau_m D_m J_0(\gamma_m r / a) \tanh \tau_m d, & 0 < r < a \\ 0, & a < r < s \end{cases} \quad (6)$$

This is an equation involving the continuous variable  $r$  over the domain  $0 < r < s$ . In order to convert to a system of linear equations for the modal coefficients, we apply the orthogonality property of the integration slot radial modes. The orthogonality property is

$$\int_0^s J_0(\zeta_n r / s) J_0(\zeta_q r / s) r dr = \begin{cases} 0, & q \neq n \\ \frac{s^2}{2} [J_1(\zeta_n)]^2 & q = n \end{cases}$$

Thus, multiplying Eq. (6) by  $J_0(\zeta_q r / s) r$  and integrating over the domain  $(0, s)$ , we obtain (upon reverting from  $q$  to  $n$ )

$$S_n \frac{s^2}{2} [J_1(\zeta_n)]^2 F_n'(0) = \int_0^s \left[ k D_0 \sin kd - \sum_{m=1}^{\infty} \tau_m D_m J_0(\gamma_m r / a) \tanh \tau_m d \right] J_0(\zeta_n r / s) r dr.$$

The integrals on the right-hand side can be evaluated using the following formula involving integrals of products of Bessel functions (see Abramowitz & Stegun 1972, p. 484)

$$\int_0^z J_0(\alpha r) J_0(\beta r) r dr = \frac{z}{\alpha^2 - \beta^2} [\alpha J_1(\alpha z) J_0(\beta z) - \beta J_0(\alpha z) J_1(\beta z)]. \quad (7)$$

Evaluating these integrals, we obtain

$$S_n = D_0 \frac{2a/s}{\zeta_n} \frac{J_1(\zeta_n a/s)}{J_1^2(\zeta_n)} \frac{k \sin kd}{F_n'(0)} + \sum_{m=1}^{\infty} D_m \frac{2\zeta_n (a/s)^3}{\gamma_m^2 - (\zeta_n a/s)^2} \frac{J_0(\gamma_m) J_1(\zeta_n a/s)}{J_1^2(\zeta_n)} \frac{\tau_m \tanh \tau_m d}{F_n'(0)}, \quad (8)$$

$n = 1, 2, 3, \dots, \infty.$

This is an expression for the coefficients  $S_n$ ,  $n=1,2,3,\dots,\infty$  of the integration slot eigenfunction series in terms of infinite sums of the coefficients  $D_m$  of the resonance tube eigenfunction series.

Next, consider the condition of pressure continuity across the interface between the resonance tube and the integration slot. For the resonance tube, setting  $x = 0^+$  in Eq. (2) provides an expression for  $p(0^+, r)$  for the region  $0 < r < a$ . For the integration slot, setting  $x = 0^-$  in Eq. (4) provides an expression for  $p(0^-, r)$  for the region  $0 < r < s$ . These two expressions must be equal for the region  $0 < r < a$ . Thus we have

$$\sum_{n=1}^{\infty} S_n J_0(\zeta_n r/s) F_n(0) = D_0 \cos kd + \sum_{m=1}^{\infty} D_m J_0(\gamma_m r/a), \quad (9)$$

for  $0 < r < a$ . Since the domain of validity of Eq. (9) is limited to  $0 < r < a$ , in this case we convert to a system of linear algebraic equations for the modal coefficients by applying the orthogonality property of the resonance tube radial eigenfunctions. This orthogonality property is

$$\int_0^a J_0(\gamma_m r/a) J_0(\gamma_q r/a) r dr = \begin{cases} 0, & q \neq m \\ \frac{a^2}{2} [J_0(\gamma_m)]^2, & q = m \end{cases}$$

Thus, multiplying Eq. (9) by  $J_0(\gamma_q r/a) r$  and integrating over the domain  $(0, a)$ , we obtain (upon reverting from  $q$  to  $m$ )

$$D_0 \frac{a^2}{2} \cos kd = \int_0^a \left[ \sum_{n=1}^{\infty} S_n J_0(\zeta_n r/s) F_n(0) \right] r dr,$$

$$D_m \frac{a^2}{2} [J_0(\gamma_m)]^2 = \int_0^a \left[ \sum_{n=1}^{\infty} S_n J_0(\zeta_n r/s) F_n(0) \right] J_0(\gamma_m r/a) r dr, \quad m = 1, 2, \dots, \infty.$$

The integrals on the right-hand side of these equations can be evaluated using the general result (7). We then obtain

$$D_0 \cos kd = \sum_{n=1}^{\infty} S_n \frac{2}{\zeta_n a/s} J_1(\zeta_n a/s) F_n(0),$$

$$D_m = - \sum_{n=1}^{\infty} S_n \frac{2 \zeta_n a/s}{\gamma_m^2 - (\zeta_n a/s)^2} \frac{J_1(\zeta_n a/s)}{J_0(\gamma_m)} F_n(0), \quad m = 1, 2, \dots, \infty. \quad (10)$$

These are expressions for the coefficients  $D_m$ ,  $m=0,1,2,\dots,\infty$  of the resonance tube eigenfunction series in terms of infinite sums of the coefficients  $S_n$  of the integration slot eigenfunction series.

#### SOLUTION OF THE COUPLED SYSTEM

The next step in the analysis is to combine Eqs. (8) and (10) to solve for the modal coefficients  $D_m$  and  $S_n$ . There are three options that could be utilized:

- a. Substitute the explicit expression (8) for  $S_n$  into Eq. (10), thereby eliminating the  $S_n$  as unknowns. This leads to a single homogeneous matrix equation for the vector unknown  $\underline{D} = [D_0, D_1, D_2, \dots]^T$ .
- b. Substitute the explicit expressions (10) for  $D_m$  into Eq. (8), thereby eliminating the  $D_m$  as unknowns. This leads to a single homogeneous matrix equation for the vector unknown  $\underline{S} = [S_1, S_2, S_3, \dots]^T$ .
- c. Combine Eqs. (8) and (10) into a single homogeneous matrix equation for the vector unknown  $[D_0, D_1, D_2, \dots, S_1, S_2, S_3, \dots]^T$ .

For each of these options, the matrix equation is infinite-dimensional and must be truncated to finite order before attempting a numerical solution. Also, since the matrix equation is homogeneous, a non-trivial solution exists only when the matrix is singular. This feature is expected, since we are solving a global eigenvalue problem for the natural frequencies of the PRT actuator system.

The three options each have certain advantages and disadvantages. For options (a) and (b), the size of the vector unknown is reduced and there is only one sequence of coefficients that must be truncated to finite order. However, the entries of the matrix are given by infinite series that must be truncated in numerical evaluation. For option (c), the size of the vector unknown is larger, and one must address the issue of truncation to finite order for both  $D_m$  and  $S_n$ . However, the entries of the matrix are simpler.

We have chosen to pursue option (c), because this leads to a matrix system whose behavior is more robust over the wide range of parameter space of interest. In forming the matrix system, Eqs. (10) are multiplied by  $J_0(\gamma_m)$  and Eqs. (8) are multiplied by  $J_1^2(\zeta_n)F_n'(0)d$ . A matrix equation

$$\underline{A}\underline{u} = \underline{0} \quad (11)$$

is then formed, where

$$\underline{u} = [D_0, D_1, D_2, \dots, D_M, S_1, S_2, S_3, \dots, S_N]^T$$

and  $M$  and  $N$  are the highest resonance-tube and integration-slot modes retained, respectively. In forming the matrix system, we utilize Eqs. (10) for  $m = 0, 1, 2, \dots, M$  and Eqs. (8) for  $n = 1, 2, 3, \dots, N$ . The matrix  $\underline{A}$  is square, has size  $M+1+N$ , and exhibits a four-block structure in which two of the blocks are diagonal sub-matrices of size  $M+1$  and  $N$ , while the other two blocks are full sub-matrices of size  $(M+1) \times N$  and  $N \times (M+1)$ .

Our analysis is a spectral representation of the acoustic field, so that rapid convergence of the series with increasing mode order is anticipated. This is especially true for global (or integral) parameters such as the resonance frequencies. The spatial resolution of the series is related to the coefficient of  $r$  in the argument of the Bessel function. For moderate to large values of the mode index  $q$ , the magnitudes of  $\gamma_q$  and  $\zeta_q$  are similar. Thus, to maintain similar resolution in the tube and slot regions, the values of  $M$  and  $N$

are chosen such that  $N/M \approx s/a$ . The choice  $M = 6$  and  $N = 24$  was used for generating the results presented in Figs. 4.1 and 4.2, while the choice  $M = 5$  and  $N = 25$  was used in generating the results in Fig. 4.3, which extend to larger values of  $s/a$ .

Since the matrix equation (11) is homogeneous, non-trivial solutions  $\underline{u} \neq 0$  exist only when the coefficient matrix  $\underline{A}$  is singular, or

$$\det(\underline{A}) = 0. \quad (12)$$

For a given geometry of the resonance tube and integration slot, the system resonances correspond to the values of  $k = \omega/c$  which satisfy Eq. (12). Solutions to Eq. (12) were obtained using the Mathematica computer package (Wolfram 1996) on a Pentium personal computer. The determinant of a large matrix often takes on very small or large values. Therefore, before utilizing numerical root-finding routines, Eq. (12) was normalized using the value of  $\det(\underline{A})$  for a representative value of  $k$ .

### RESULTS FOR PRT RESONANCE FREQUENCIES

In Fig. 4.1, theoretical predictions for the resonance frequency are compared with data from the IIT experiments. The case chosen for comparison is a 37 psig supply pressure and an integration slot width  $w = 0.25$  in., also shown in Fig. 2.6. The experimentally measured frequency varies from 2.2 kHz to 14 kHz as the tube depth is decreased from 1.25 in. to 0.0938 in. The frequency increases monotonically as  $d$  is decreased, but the rate of increase exhibits some variability, with a fairly rapid variation in the vicinity of  $d = 0.5$  in. The explanation for this locally rapid variation is not known.

Three theoretical predictions are presented in Fig. 4.1. The basic resonance tube theory is the standard quarter-wavelength formula in the absence of an end correction,  $f = c/4d$ . This result is seen to lie above the experimental data, increasingly so as the tube depth is decreased. The second theoretical result is the quarter-wavelength formula modified by the end correction for the case of an infinite flange in free space,  $\Delta d = 0.82a$  (King 1936). The end correction lowers the frequency, resulting in better agreement with the experimental data. However, this theoretical prediction diverges from the experimental data for  $d < 0.25$  in., lying significantly above the data.

The third theoretical result is a prediction of the theory developed in this report, for an integration slot of radius  $s = 0.35$  in. and width  $w = 0.25$  in. In the region  $d > 0.25$  in., the prediction of our new theory is virtually indistinguishable from the standard theory with the infinite flange end correction. However, the predictions of the two theories are quite different for  $d < 0.25$  in., where our new theory remains in excellent agreement with the experimental data. It should be mentioned that the value of the integration slot radius  $s$  was chosen to achieve good agreement with the data. The value of  $s$  is ill defined in the experiments, since the geometry is not axisymmetric. For larger values of  $s$  the prediction would lie below the data in the range  $d < 0.25$  in., while for smaller values of  $s$  the prediction would lie above the data. The results demonstrate that the

geometry of the integration slot can significantly affect the resonant frequency, particularly for small values of the tube depth.

Using our new theory, the influence of integration slot geometry on the resonant frequency is further demonstrated in Figs. 4.2 and 4.3. In Fig. 4.2, the lowest resonant frequency is plotted as a function of integration slot width in non-dimensional form,  $w/a$ . Three tube depths are presented, and the slot radius is held constant at  $s/a = 3$ . In each case, the result for large  $w/a$  is very close to the result produced by the infinite flange end correction. The value of  $fd/c$  decreases as  $w/a$  decreases, the decrease becoming quite rapid at small  $w/a$ . Essentially, the unsteady velocity in the integration slot is increased as  $w/a$  decreases, leading to a higher inertia in the system and therefore a reduced resonant frequency. The non-dimensional frequency is also decreased when  $d/a$  is decreased at fixed  $w/a$ . Again, this behavior arises because the integration slot contributes a higher fraction of the total inertia in the system.

The influence of integration slot radius  $s$  on the resonant frequency of the lowest mode is illustrated in Fig. 4.3. Results are presented for the case  $d/a = 3$ , for three values of the integration slot width. The resonant frequency decreases as  $s/a$  increases. The decrease of  $fd/c$  with increasing  $s/a$  is most significant for smaller values of the slot width, because the velocities in the slot are higher in this case and therefore contribute a greater fraction of the total inertia of the system. To compare the analytical frequency prediction with the result of the numerical simulations discussed in the previous section, we see from Fig 4.3 that  $fd/c = 0.178$  for the case  $d/a = 3$ ,  $w/a = 2$  and  $s/a = 5$ . Converting this result to dimensional form, the analytical prediction for the frequency is  $f = 6.44$  kHz. The frequency estimated from the simulation time series was 7.6 kHz. Compared to the simulation result, the analytical prediction for the frequency is 15% low. This is quite reasonable agreement, considering the various approximations involved in the analysis and the simulations.

The behavior of the resonant frequency as a function of  $w/a$  or  $s/a$ , illustrated in Figs. 4.2 and 4.3, is for the lowest frequency mode of the system. For the second mode of the system, in some cases the natural frequency increases as  $w/a$  is decreased. The behavior of specific higher modes is highly dependent on the geometrical parameters of the PRT actuator, and general conclusions are not easily drawn. We have focused on the lowest frequency mode because the experiments indicate that this mode is typically most strongly excited when the PRT actuator is operating in a high-amplitude condition.

## 5. SIMULATIONS OF HIGH FREQUENCY FORCING OF A PLANE WAKE

### a. OVERVIEW

Simulations of high frequency excitation of a transitional plane wake are found to increase the turbulent dissipation rate, reduce the turbulent energy production rate, and lower the level of turbulent kinetic energy for a sustained period after the transition process is complete. An altered turbulent state seems to develop. Similar excitation of a fully turbulent plane wake shows only a weak transient effect. This work is consistent with recent experimental studies but clarifies several aspects of the phenomenon. At the end of a simulation, which started with a transitional plane wake initial condition, the following quantitative impact of high frequency forcing is observed. The integrated turbulent kinetic energy is reduced by 20%, the integrated turbulent dissipation rate is increased by 14%, and the integrated turbulent production rate is reduced by 24%. The increase in the dissipation rate due to high frequency excitation is intuitively expected, at least initially, but these simulation results show that high frequency forcing has an even more important effect in reducing the rate of production of turbulent energy. Interestingly these effects don't show up until the end of the transition process.

### b. BACKGROUND

In the early 1990's, Glezer and his co-workers (Glezer was then at University of Arizona) made a startling discovery. They found that forcing at frequencies too high to affect the production scales directly led to a dramatic alteration in the development of a turbulent shear layer. An experimental study of this phenomenon is presented in Wiltse & Glezer 1998. They used piezoelectric actuators located near the jet exit plane to force the shear layers of a square low-speed jet. The actuators were driven at a high frequency in the Kolmogorov inertial subrange, much higher than the frequencies associated with the large-scale motion (where most of the turbulent energy is produced and located), but much lower than those associated with the Kolmogorov scale (where the turbulent energy is dissipated). Measurements of shear-layer turbulence showed that the direct excitation of small-scale motion by high-frequency forcing led to an increase in the turbulent dissipation of more than an order of magnitude in the initial region of the shear layer! The turbulent dissipation gradually decreased with downstream distance, but remained above the corresponding level for the unforced flow at all locations examined. High-frequency forcing increased the turbulent kinetic energy in the initial region near the actuators, but the kinetic energy decreased quite rapidly with downstream distance, dropping to levels that were a small fraction of the level for the unforced case. Perhaps most importantly from the present standpoint, high-frequency forcing significantly decreased the energy in the large-scale motion, especially with increasing downstream distance. Wiltse and Glezer interpreted this behavior as an enhanced transfer of energy from the large scales to the small scales.

Though the research community may have been surprised by the results of the recent work by Glezer and his associates, there are, in fact, earlier hints of such behavior. Examples of relevant earlier work include Vlasov & Ginevskiy 1974, Zaman & Hussain 1981 and Zaman & Rice 1992. These earlier works studied the effect of forcing free shear flows at frequencies roughly 50% higher than the dominant natural frequency.

Zaman & Hussain 1981 and Zaman & Rice 1992 found that such forcing reduces the turbulent intensity downstream of the forcing. This result is consistent with the work of Glezer and associates; however, forcing at frequencies 50% greater than the dominant natural frequency still results in excitation of amplified instabilities of the flow. In fact, these earlier studies attribute the reduced intensities to earlier saturation of the forced instabilities. In the present work, as well as that of Glezer, the forcing frequencies are much too high to excite amplified instabilities in the flow. Nonlinear processes are an essential part of the interpretation of the phenomenon, as the results of this study will show.

The initial work Wiltse & Glezer 1998 has expanded into other applications. To explore the potential of high-frequency forcing for active acoustic suppression, Cain proposed in 1997 a set of experiments involving an edge tone shear layer and an open cavity flow. This work was funded by the US Air Force Research Laboratory and the experiments were developed and executed at Boeing by Raman and Kibens (Raman et al. 2000). These experiments involved high-frequency forcing applied to low-speed flows using wedge piezo actuators and powered resonance tubes. The system is simple, open loop, compact, potentially requires little power, and is easily integrated. Dramatic results, such as reductions of 20 dB in spectral peaks and 5-8 dB in overall levels across the entire acoustic spectrum, were obtained in some cases.

Sample results are presented in Figs. 5.1 and 5.2. Following this success in low-speed flows, an international cooperative program continued this work, performing transonic experiments in a mid-size facility in the United Kingdom. Similar reductions in noise level were obtained in these transonic experiments. Discussion of this work is given in Raman et al. 2000 and Stanek et al. 2000. Other experiments at Georgia Tech have shown significant potential of high-frequency forcing in controlling reaction rates in chemically reacting flows (see Davis 2000).

This recent work at Georgia Tech and Boeing offers a new set of control concepts that are in sharp contrast to earlier ideas on how control of free shear flows should be approached. The review by Ho & Huerre 1984 characterizes the perspectives of the 1970's and 1980's, demonstrating the link between large-scale structures and linear stability theory. Drazin & Reid 1981 identify approaches to linear stability theory that determine the scale of exponentially growing disturbances. The work by Ho & Huerre 1984 extends the earlier stability theory/large-scale structure ideas by discussing vortex pairing and the more general merging of many large-scale structures. Ho & Huerre 1984 provide convincing experimental demonstrations of flow control by excitation frequencies that produce exponentially growing disturbances according to linear stability theory. Cain & Thompson 1986 provide another example of the merits of linear stability analysis. They show that the growth rates predicted by linear theory are able to predict the evolution of finite amplitude disturbances to a saturated state as given by a full nonlinear simulation. These are a few examples of many studies that characterize the control possibilities in free shear flows using "low-frequency", stability-theory-guided frequency selections. The Georgia Tech/Boeing studies constitute a major departure from this earlier work. These recent studies do not dispute the results of the earlier work, but challenge the

assumption that turbulence theory and linear stability theory preclude interesting effects in the "high-frequency" excitation regime. Control effects using the new "high-frequency" excitation regime are currently lacking a theoretical explanation and the present study is aimed at adding detailed quantitative insight into this phenomenon.

### c. COMPUTATIONAL APPROACH

There is a need to understand the basic mechanism behind effective high-frequency forcing so that scaling laws can be developed to facilitate reliable large-scale system design. The Boeing experiments sometimes produce dramatic results, but other high-frequency control systems don't show the same improvement. An understanding of the physics is required to ensure reliable application of the technology.

We use direct numerical simulations of free shear layers to investigate the impact of high-frequency forcing on various aspects of shear layer evolution. To ensure that the results found here are representative of what would be observed in flows of practical interest, it is necessary to have the ability to simulate realistic high-Reynolds number turbulent shear flows. For this purpose, the pseudospectral free shear layer code used by Rogers & Moser 1994 and Moser, Rogers, & Ewing 1998 has been chosen (the version of the code used to generate the simulations described here actually uses a variation on the numerical representation of the flow variables in the inhomogeneous direction, as described in Rogers 2001). This code is designed to simulate incompressible, temporally evolving, plane free shear layers. By simulating a temporally evolving flow, much higher turbulence Reynolds numbers can be achieved and cleaner boundary conditions can be implemented. Although the temporally evolving flow possesses symmetries not present in spatially developing flows, the dynamics of the large-scale structures are similar in these two flows and the results obtained here should be relevant to spatially developing flows as well. Thus the incompressible flows simulated here should be comparable to the experimental flows of Wiltse & Glezer 1998.

The selection of test cases needed to take into account the consideration that high-frequency excitation is typically a technique for reducing turbulence levels, as opposed to previous approaches, which enhance turbulence production, especially in globally coherent modes. Hence, a baseline flow needs to be one that either develops a considerable level of large-scale energy content through natural growth, or one that achieves such energy content through suitable forcing. An important feature of a baseline case must be that the turbulence field must exhibit a sufficiently high energy level to permit the demonstration of the fundamental turbulence suppression effect.

The turbulent plane wake flow was selected as the first flow of investigation, with the new simulations being compared to the baseline cases presented in Moser et al. 1998. These previously simulated baseline cases include three different plane wake flows, an "unforced" case, a (weakly) "forced" case, and a "strongly forced" case, the two forced cases having additional energy added to the two-dimensional modes of the computation at the initiation of the wake. The "strongly forced" case does not achieve self-similarity and is therefore a poor choice for a baseline flow. Both the "unforced" and "forced" cases do evolve self-similarly once developed, and exhibit statistical properties similar to

experimental wakes. The "unforced" case spreads relatively slowly compared to the "forced" case and to most experiments, and has little large-scale organization. One of the goals of this work is to determine whether high-frequency forcing can reduce the spreading rate of a free shear layer (and perhaps the associated level of large-scale organization) and this may not be possible for a baseline flow that is already spreading at a minimal rate. For this reason, the "forced" case (low frequency forcing termed "fwak" by Moser et al.) was chosen as a baseline flow for the investigation described here; although spreading at a rate typical of experimental flows, it is possible for the flow spreading rate to be reduced.

This study exploits the earlier work of Spalart 1988, using his results of turbulent boundary layer calculations to develop initial conditions for these wake calculations. Further leverage is gained by using the initial conditions and wake evolution calculations of Moser et al. 1998 for a well documented reference case for the present study. The present work includes a total of six high frequency excitation cases and a reference transitional initial condition simulation. Four of the six high frequency excitation cases are started from a fully turbulent initial condition. The turbulent initial condition cases are labeled turb1, turb2, turb3, and turb4, with the differences having to do with the nature and level of the high frequency excitation. A more detailed discussion of the set-up for all cases is given in Cain et al. 2001. From a big picture point of view the turb4 case is considered the best approximation to the excitation used by Wiltse & Glezer 1998. The simulated base case or reference for the fully turbulent initial condition was labeled "fwak" by Moser et al. 1998 and the original paper by Moser et al. may be of value to those seeking a deeper understanding of how these simulations are performed.

The two other high frequency excitation cases are started from what is considered a transitional initial condition. These cases are constructed by reducing the velocity disturbance levels of the "fwak" initial condition by a factor of 10 and then adding high frequency excitation. These two cases with high frequency excitation are labeled "frans" and "htrans". In the frans case the high frequency excitation is at the same wavenumbers and spatial region as turb4 and is applied from the beginning of the transitional case. A reference case without high frequency excitation is called "trans" and is compared to the cases with high frequency excitation. The "htrans" case differs from the "frans" primarily in that the high frequency excitation is not applied until the reference disturbances have amplified substantially.

#### d. RESULTS

In order to verify that the forcing used in the computations is qualitatively similar to that found in the experiments, energy spectra from the forced flows have been examined.

The streamwise  $k_x$  wavenumber spectra for  $\overline{u'^2}$ ,  $\overline{v'^2}$ , and  $\overline{w'^2}$  at  $\tau = 12.30$  (shortly after the forcing has been initiated) in the turb4 flow are shown in Fig. 5.3. The spectra are similar to those observed by Wiltse & Glezer 1998, with the energy associated with the forcing being at about the same relative wavenumber, of similar relative width, and of similar amplitude compared to the energetic large scales of the turbulence.

### i. Fully turbulent initial conditions

In this section the impact of high-frequency forcing on a fully turbulent plane wake is investigated. The figures presented here contain results from the four "turb" simulations, as well as for the unforced baseline case "fwak". As noted above, the forcing is applied at  $\tau_f = 12.17$ . The forced runs are terminated at  $\tau \approx 15$  for turb1, turb2, and turb3, and at  $\tau = 30$  for turb4.

The evolution of the scale parameters describing the wake mean velocity profile, the magnitude of the peak mean velocity deficit  $U_0$  and the full width of the wake at the half-deficit points  $b$ , are largely unaffected. The half-width  $b$  is shown in Fig. 5.4. These parameters have been non-dimensionalized by their values at  $\tau = 12.17$ , denoted by  $U_0^0$  and  $b^0$ . The mean profile evolution for all four forced flows is virtually identical to the baseline case, with only barely perceptible differences in  $U_0$  and  $b$ .

The evolution of the turbulence is impacted to a greater degree than the mean velocity profile. The evolution of twice the cross-stream ( $y$ ) integrated turbulent kinetic energy is shown in Fig. 5.5. Relatively little turbulent kinetic energy has been added to the turb1, turb2, and turb3 cases by the forcing and what has been added starts decaying fairly rapidly. In contrast, the integrated kinetic energy has been greatly (by 49%) augmented by the forcing in turb4. In this case too, however, the energy decays rapidly, assuming a value slightly (1.2%) below that of the baseline unforced case by  $\tau = 30$ . Although this reduction in turbulent kinetic energy once the flow is developed is qualitatively similar to the experimental observations of Wiltse & Glezer 1998, the magnitude of the effect is much weaker.

The impact of the forcing on the turbulent kinetic energy dissipation rate is even more pronounced, as expected since the dissipation is associated with strong velocity gradients at small scales. The evolution of the cross-stream integrated turbulent kinetic energy dissipation rate is shown in Fig. 5.6. The relative increase in dissipation rate is thus higher than that of the kinetic energy, reaching 425% initially at  $\tau_f$  for case turb4. This increase also decays rapidly, with the turb4 dissipation level at  $\tau = 30$  being indistinguishable from the baseline case, indicating that the high-frequency forcing has not resulted in a sustained increase in dissipation level.

The impact of the forcing on the production of turbulent kinetic energy is much less pronounced, as expected since production is not strongly impacted by the small-scale motions. The evolution of the cross-stream integrated turbulent kinetic energy production rate is shown in Fig. 5.7. The turb1, turb2, and turb3 flows depart only negligibly from the baseline case. The high-frequency forcing results in a 6.7% reduction in the production for case turb4, but after initially further decreasing relative to the baseline case, the evolution becomes identical to that of fwak by  $\tau = 30$ .

ii. Transitional initial conditions

The effects of high-frequency forcing in the simulations of fully turbulent wakes die out quickly and have no lasting impact. In order to determine whether transitional wakes are more sensitive to high-frequency forcing, three additional simulations were made, as outlined in Cain et al. 2001.

The impact of the high-frequency forcing when applied early in the transition process (ftrans) is more significant than when applied later (htrans) or when applied to the fully turbulent wake examined above. Additionally, it appears that some of the effects may be sustained, persisting even once the wake turbulence has developed.

The time evolution of the wake width is shown in Fig. 5.8. The evolution of in the htrans flow is very similar to the corresponding evolution in the unforced trans case, while the behavior in the ftrans case is somewhat different. In ftrans the wake spreads more uniformly in time and ultimately is not as wide as in the trans case at the same time.

Similarly, the evolution of the  $y$ -integrated turbulent kinetic energy shown in Fig. 5.9 shows little difference between the htrans and trans cases, but forcing early in the transition, as in ftrans, results in sustained lower levels of turbulent kinetic energy after  $\tau \approx 150$ . At  $\tau = 250$  this reduction (ftrans relative to trans) is 20.0%, whereas the reduction in wake width noted above is only 5.6%. The average turbulent kinetic energy density in the wake is thus reduced by 15%.

The sustained reduced turbulent kinetic energy levels in ftrans are accompanied by sustained increased levels of turbulent kinetic energy dissipation. As seen in Fig. 5.10, the initial large increase in turbulent kinetic energy associated with the high-frequency forcing decays quickly, but in ftrans there is still a 13% increase relative to trans at  $\tau = 250$ . In contrast, the differences between htrans and trans is virtually undetectable for  $\tau > \tau_h + 20$ .

Reductions in turbulent kinetic energy come about not only as a result of sustained increased dissipation levels, but also because of sustained decreased production levels. The time evolution of the  $y$ -integrated production of turbulent kinetic energy is shown in Fig. 5.11. In both ftrans and htrans the high-frequency forcing results in a short term (for  $\Delta\tau \approx 5$  to  $7$ ) reduction in production. In ftrans the integrated production actually becomes negative; in htrans it is reduced by about 18%. As before, the evolution in htrans quickly relaxes to the unforced behavior, whereas ftrans maintains a sustained reduction of 24% at  $\tau = 250$ . For  $\tau < 100$  one effect of the high-frequency forcing in ftrans is to shift the integrated production and dissipation curves about  $\Delta\tau = 6$  to earlier times. It is thus possible that the primary effect of the forcing is to initiate an earlier transition, which in turn results in a narrower wake with reduced levels of turbulent kinetic energy. However, it seems that the most significant effect is a sustained reduction in the level of turbulence production in the post transition state. This reduction may be due to nonlinear interactions between high amplitude high frequencies and the production

scales with a net effect of reducing the correlation coefficient between the components of the Reynolds shear stress.

Given the reduced wake width and turbulent kinetic energy density in the ftrans flow, it is of interest to examine the structure of the flow to determine what, if any, structural changes are associated with the changes in wake statistics. Early in the flow evolution the differences between the ftrans and trans flows are minimal. Once the flow is developed, however, detectable differences are evident. Contours of vorticity magnitude are shown in Figs. 5.12 and 5.13 for both flows at  $\tau = 200$ .

The forced flow ftrans is less organized, with smaller, less coherent intrusions of irrotational flow into the layer from both freestreams. The reduced coherence and more homogeneous nature of the case with high frequency forcing again suggests a reduced correlation of the Reynolds shear stress components. These differences are the same as those observed in Moser et al. 1998 for wakes of differing self-similar spreading rates that arise from large scale two-dimensional forcing. Also evident in the figure is the limited statistical sample of large-scale eddies (about 2.5) in the computational domain at  $\tau = 200$ , suggesting the need for some caution when drawing conclusions from these late-time results.

#### e. CONCLUSIONS

Simulations of **fully turbulent** wakes suggest that high-frequency forcing has a minimal impact on the evolution of this developed flow after a brief transient. On the other hand, **transitional wakes** exhibit considerable sensitivity to high-amplitude, high-frequency forcing. Such forcing must be applied while the amplitudes of the growing turbulent field (especially those of coherent modes) are still small compared to their amplitudes in fully developed flow. In this case, the simulations show that sustained reduction in wake spreading and turbulent kinetic energy density is possible. In particular, reduction in y-integrated turbulent kinetic energy of up to 20% was observed in the simulations, the integrated turbulent dissipation rate increased by 14%, and the integrated turbulent production rate was reduced by 24%. The increase in the dissipation rate due to high frequency excitation is intuitively expected, at least initially, but the simulation results showed that the high frequency forcing has an even more important effect, namely, that of reducing the rate of production of turbulent energy. Longer simulations might show even more significant effects but a much costlier, larger domain calculation would be required to confirm this.

#### f. ACKNOWLEDGEMENTS

The first author wishes to acknowledge the support of the Center for Turbulence Research during the initial and middle phases of this study. This work also benefited from discussions with Prof. A. Glezer regarding the related experimental work as well as from conversations with Prof. W. C. Reynolds.

## **6. LIST OF PRESENTATIONS, PAPERS AND PUBLICATIONS FROM THIS PROGRAM**

- a. Cain, A. B., Rogers, M. M., Kibens, V., and Raman, G., "Simulations of High-Frequency Excitation of a Plane Wake," AIAA-2001-0514, Presented at the AIAA Aerospace Sciences Meeting, Reno, NV, Jan., 2001.
- b. Khanafseh, S., Raman, G., Cain, A., "Development of a High Bandwidth Hartmann-Whistle Type Actuator," Acoustical Society of America Conference held in Chicago, IL, June. 4-6, 2001.
- c. Cain, A.B., "Effects of High Frequency Forcing, Simulation of Powered Resonance Tubes, and Actuator Scaling," The Boeing/DARPA Phase 2 kick-off meeting in Chicago, IL, Aug. 7, 2001.
- d. E.J. Kerschen, "Analytical modeling of the resonant frequencies of a powered resonance tube," Division of Fluid Dynamics of the American Physical Society Meeting, Nov. 18-20, 2001, San Diego, CA
- e. A.B. Cain, G. Raman, and E.J. Kerschen, "DIRECT SIMULATION OF A POWERED RESONANCE TUBE," Division of Fluid Dynamics of the American Physical Society Meeting, Nov. 18-20, 2001, San Diego, CA
- f. Raman, G., Khanafseh, S. & Cain, A., "High bandwidth powered resonance tube actuators. Abstract submitted for the AIAA Aerospace Sciences Meeting, 2002.
- g. A.B. Cain, E.J. Kerschen, and G. Raman, "Simulation of Acoustic characteristics and Mechanism of Powered Resonance Tubes," AIAA/CEAS Aeroacoustics Conference, Breckenridge, CO, 17-19 June, 2002
- h. A. B. Cain, E.J. Kerschen, and G. Raman, "Interaction of a boundary layer with a powered resonance tube," AIAA Flow Control Conference, St. Louis, MO, 24-27 June, 2002.

## 7. CONCLUSIONS

The Department of Defense, DARPA and the Air Force in particular, are moving future warfighter capabilities forward by application of new technologies. Active Flow Control (AFC) is one of these technologies that offers important new capabilities. Actuators with high bandwidth and strong authority are required for AFC applications. In this Phase 1 STTR Program, we have developed and demonstrated a new high bandwidth actuator, based on the powered resonance tube (PRT) concept. The PRT concept involves a high-speed jet that impinges on the open end of an open-closed resonance tube. This device is capable of producing flow oscillations of high amplitude and high frequency. The hardware advances are complemented by direct numerical simulations and analytical modeling. These provide new understanding of the physics of the unsteady flow, and guidance for future prototype and production designs of PRT actuators.

The variable frequency of the PRT actuator is produced by varying the depth of the resonance tube. First, the high bandwidth capability was demonstrated by experiments in which the depth of the resonance tube was varied manually. This was followed by a more refined effort using a computer-controlled mechanism that varied the depth of the tube in response to frequencies selected by the user. The control system utilizes a look-up table based on an extensive database. The spacing between the driving jet and resonance tube is also varied, in order to obtain a high amplitude resonance. Using a  $\frac{1}{4}$  in. diameter tube, the variable-depth PRT actuator produces strong oscillations (125 dB to 160 dB) over a frequency range from 1.6 kHz to 14 kHz.

Direct numerical simulations of the unsteady flow in the PRT actuator were carried out in order to explore the flow physics and better understand the fundamental mechanisms responsible for the resonance. In particular, it was found that the flow in the integration slot (between the nozzle of the driving jet and the open end of the resonance tube) is confined to a narrow section much smaller than the full width of the slot. Analytical modeling of the acoustic resonances in the PRT geometry was carried out in order to understand how the geometrical parameters influence the resonance frequency. For the smaller tube depths associated with higher resonance frequencies, the integration slot geometry was found to play an important role in determining the resonant frequency.

One of the most promising applications of PRT actuators for active flow control is in high frequency forcing of turbulent boundary and shear layers. Strong forcing is applied at frequencies in the inertial subrange of the turbulent layer. Direct numerical simulations of this phenomenon have been carried out in transitional and turbulent wake flows (with partial support from the Center for Turbulence Research). These simulations show that the high frequency excitation reduces the turbulent production rate and increases the turbulent dissipation rate, leading to a dramatic reduction in the turbulent kinetic energy of the flow.

## **8. RECOMMENDED FUTURE WORK – JET NOISE REDUCTION**

Future work that leverages what has been accomplished in this Phase 1 STTR would produce impacts on applications that benefit DoD, and US society generally in addition to specific payoffs for the Air Force. The Phase 1 effort has succeeded in producing high bandwidth actuator hardware with strong authority. A Phase 2 program would further advance scientific knowledge and contribute to commercial applications. Several potential applications have been identified through preliminary explorations with potential commercialization partners and customers. Discussions with The Boeing Company and BF Goodrich Aerospace have focused on the application of PRT actuators for reducing aircraft noise, especially jet noise. Aircraft noise reduction is both an important problem and a multi-billion dollar market. Noise levels of both new and existing aircraft need to be reduced to meet increasingly stringent US, International and airport (such as Heathrow and Washington Reagan) standards. BFGA/AG states that they have significant and continuing interest in ITAC's technology in meeting these goals. Boeing has further expressed a desire to help with a flight test demonstration.

A Phase 2 program would also provide important scientific advances. Further development of PRT actuator systems to increase their efficiency and effectiveness is desirable. In addition, a deeper investigation of the issue of actuator effectiveness is needed. Characterization of an actuator by its acoustic decibel level in the absence of an external stream and boundary layer is inadequate for evaluating its effectiveness. In some cases an actuator can produce high dB levels but the levels of fluctuating vorticity injected into the external flow are insignificant. In Phase 2 we propose to evaluate the strength and nature of the perturbations injected into external flows by high bandwidth PRT actuators in various flow control situations. Essentially, it is this generalized receptivity, considering both instability response and high frequency excitation, which must be addressed to properly evaluate actuator effectiveness.

In closing we believe that future work should address both applications issues and scientific enabling issues. The Phase 1 effort has made a strong start on developing high bandwidth actuators with strong authority. The hardware development, simulation capability and analysis of our Phase 1 program point the way to a triad development structure that offers considerable promise.

## REFERENCES

- Abramowitz, M. & Stegun, I., 1972, *Handbook of Mathematical Functions*, Dover.
- Cain, A. B., Vaporean, C. N., and Parekh, D. E., "Computational Characterization of Receptivity in Jet Flow Control," ASME FEDSM98-5310, Washington, D.C., June 1998.
- Cain, A.B. and Bower, W.W., "Comparison of Spatial Numerical Operators for Duct-Nozzle Acoustics," Proc. of the Computational Aeroacoustics Workshop (NASA Langley), 1995.
- Cain, A. B. & Thompson, M. W., 1986, "Linear and Weakly Nonlinear Aspects of Free Shear Layer Instability, Roll-Up, Subharmonic Interaction and Wall Influence," AIAA-86-1047, May, 1986.
- Davis, S. A., 2000, "The manipulation of large and small flow structures in single and coaxial jets using synthetic jet actuators," Ph.D. thesis, Georgia Institute of Technology, May 2000.
- Drazin P.G. & Reid, W.H., 1981, "Hydrodynamic Stability," Cambridge University Press.
- Greenblatt D, Wygnanski IJ, "The control of flow separation by periodic excitation," PROGRESS IN AEROSPACE SCIENCES, 36 (7): 487-545 OCT 2000
- Ho, C. M., Huerre, P., 1984, "Perturbed Free Shear layers," Annual Review of Fluid Mechanics, vol. 16, p. 365.
- King, L. V., 1936, "On the Electrical and Acoustic Conductivities of Cylindrical Tubes Bounded by infinite Flanges," *Phil. Mag.*, 21, 128-144.
- Moser, R. D., Rogers, M. M. & Ewing, D. W., 1998 "Self-similarity of time-evolving plane wakes," vol. 367, pp. 255--289.
- Nishri, B. and Wygnanski, I. 1998 "Effects of periodic excitation on turbulent flow separation from a flap," A.I.A.A. J. 36:547-556.
- Raman, G., Kibens, V., Cain, A. & Lepicovsky, J., 2000 "Advanced actuator concepts for active aeroacoustic control." AIAA 2000-1930, 6<sup>th</sup> AIAA/CEAS Aeroacoustics Conference, June 2000, Lahaina, Hawaii.
- Rogers, M. M. & Moser, R. D., 1994, "Direct simulation of a self-similar turbulent mixing layer," *Phys. Fluids* vol. 6, pp. 903--923.
- Rogers, M. M., 2001, "The evolution of strained turbulent plane wakes," to appear in *J. Fluid Mech.*

Spalart, P. R., 1988, "Direct simulation of a turbulent boundary layer up to  $Re_{\theta}=1410$ ," J. Fluid Mech., vol.187, pp. 61--98.

Stanek, M., Raman, G., Kibens, V. & Ross, J., 2000, "Cavity tone suppression using high frequency excitation," AIAA 2000-1905, 6<sup>th</sup> AIAA/CEAS Aeroacoustics Conference, June 2000, Lahaina, Hawaii.

Stanek, M., Raman, G., Kibens, V., Ross, J., Peto, J., and Odedra, J. 2001 Suppression of cavity resonance using high frequency forcing - the characteristic signature of effective devices. AIAA paper 2001-2128.

Vlasov, Y.V. & Ginevskiy, A.S., 1974, "Generation and Suppression of Turbulence in an Axisymmetric Turbulent Jet in the Presence of an Acoustic Influence," NASA TT-F-15, 721, 1974.

White, F. M., 1974, *Viscous Fluid Flow*, McGraw-Hill

Wiltse, J.M. & Glezer, A., 1998, "Direct excitation of small-scale motions in free shear flows," Phys. Fluids, vol. 10, pp. 2026--2036.

Wolfram, S., 1996, *The Mathematica Book*, Cambridge.

Zaman, K.B.M.Q. & Hussain, A.K.M.F., 1981, "Turbulence Suppression in Free Shear Flows by Controlled Excitation," J. Fluid Mech. Vol. 103, pp. 133-159.

Zaman, K.B.M.Q. & Rice, E.J., 1992, "On the Mechanism of Turbulence Suppression in Free Shear Flows Under Acoustic Excitation," AIAA-92-0065, Presented at the 30<sup>th</sup> Aerospace Sciences Meeting.

ft (kHz)	Spacing (in) and frequency % error of each case					
	0.22 in	e%	0.37 in	e%	0.5	e%
2.2	2.19	0.45	2.41	9.55	2.24	1.82
12	12.8	6.67	15	25.00	13.12	9.33
(a) changing spacing at 35 psig						
ft (kHz)	Pressure (psig) and frequency % error of each case					
	25 psig	e%	30 psig	e%	35 psig	e%
2.2	2.24	1.82	2.18	0.91	2.19	0.45
12	15	25.00	11.65	2.92	12.8	6.67
(b) changing pressure at 0.22 in spacing						

Table 2.1 Success of the look-up table method in achieving a prescribed frequency. The left column provides the prescribed frequency. The frequency obtained at various supply pressures and the percent error are given in other columns.

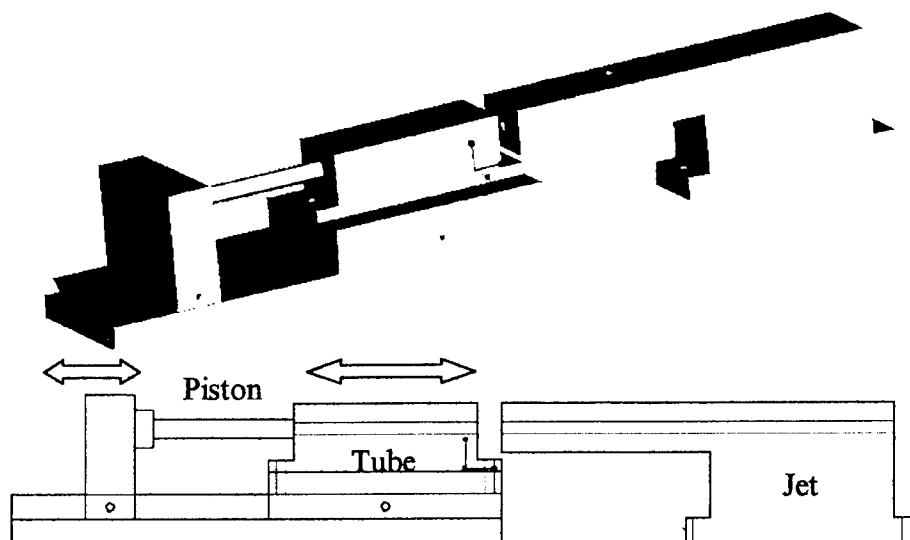


Fig. 2.1 Manually operated powered resonance tube used during the initial stages of our experiments. This apparatus was used to demonstrate the effect of changing the depth of the resonance tube and the “spacing” between the supply jet and the resonance tube.

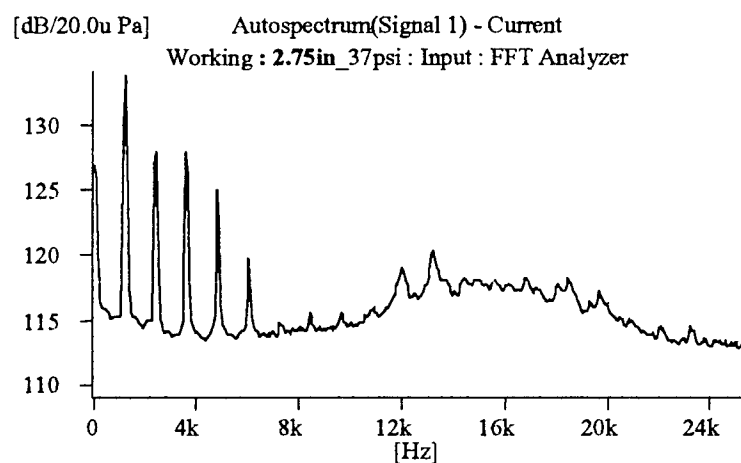


Fig. 2.2 Autospectrum from resonance tube at 0.5 inch spacing, 2.75” tube depth and a pressure of 37psi.

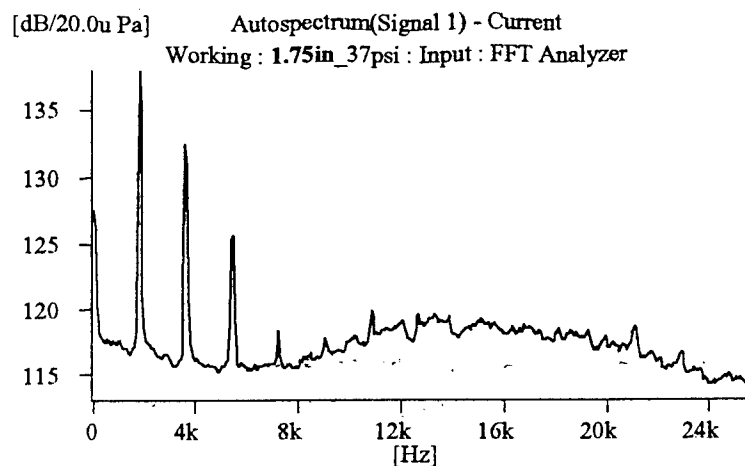


Fig. 2.3 Autospectrum from resonance tube at 0.5in spacing, 1.75" tube depth and a pressure of 37psi.

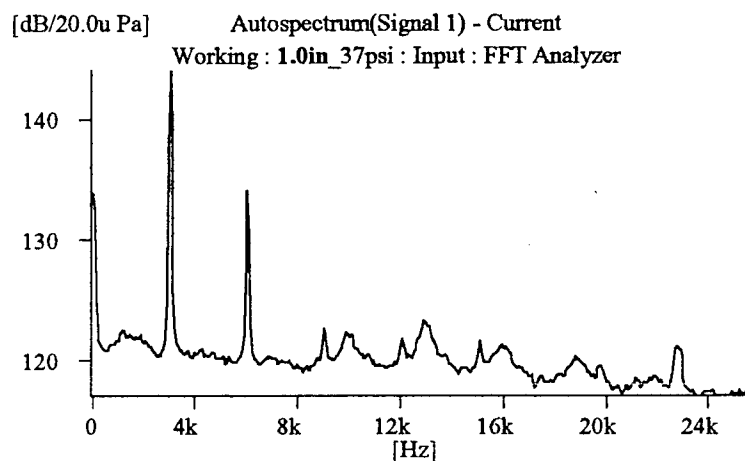


Fig. 2.4 Autospectrum from the resonance tube at 0.5in spacing, 1.0" tube depth and a pressure of 37psi.

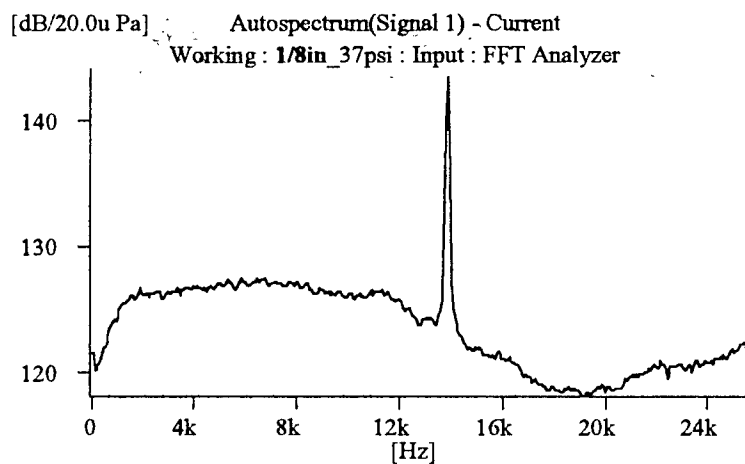


Fig. 2.5 Autospectrum from resonance tube at 0.5in spacing, .125" tube depth and a pressure of 37psi.

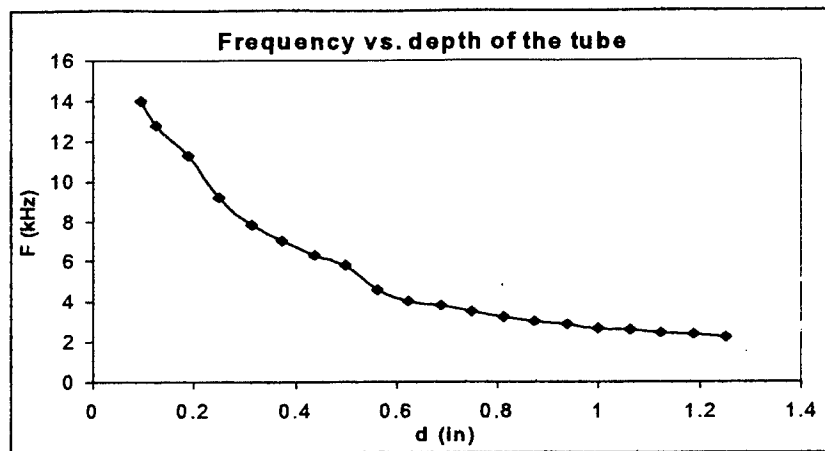


Fig. 2.6 Frequency vs. depth for the resonance tube at 0.25" spacing and 37psig pressure.

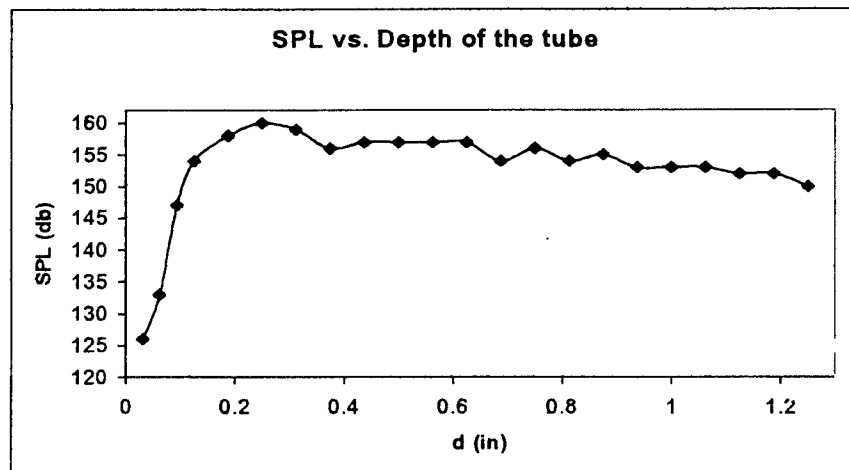


Fig. 2.7 Sound Pressure Level (SPL) vs. the depth of the tube at 0.25" spacing and 37 Psig pressure.

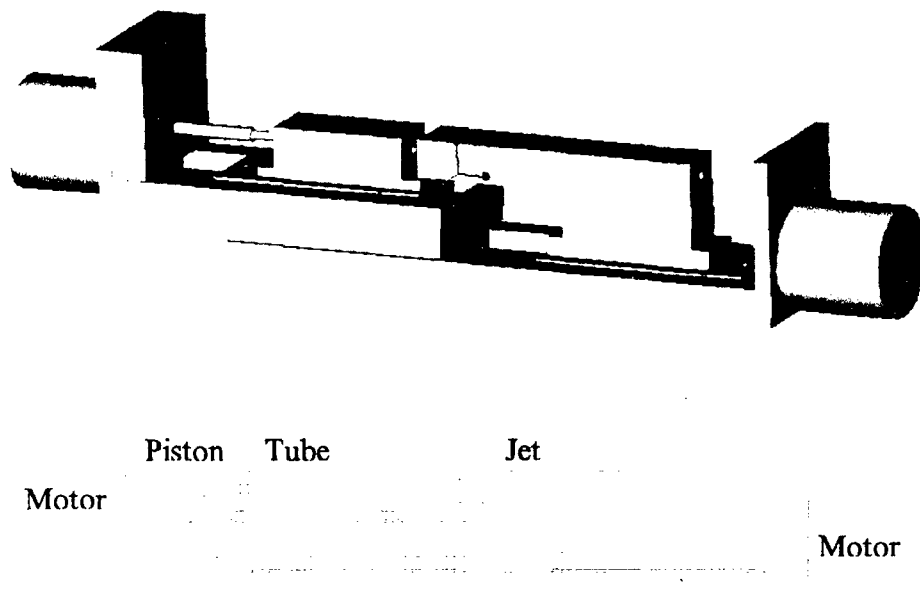


Fig. 2.8: Modified computer controlled powered resonance tube.

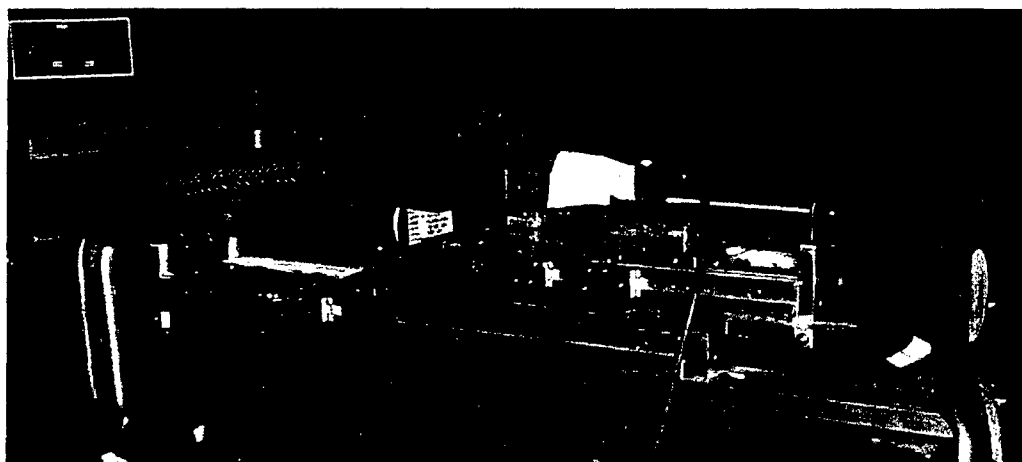


Fig. 2.9: Photograph of the modified powered resonance tube that could be operated by computer control.

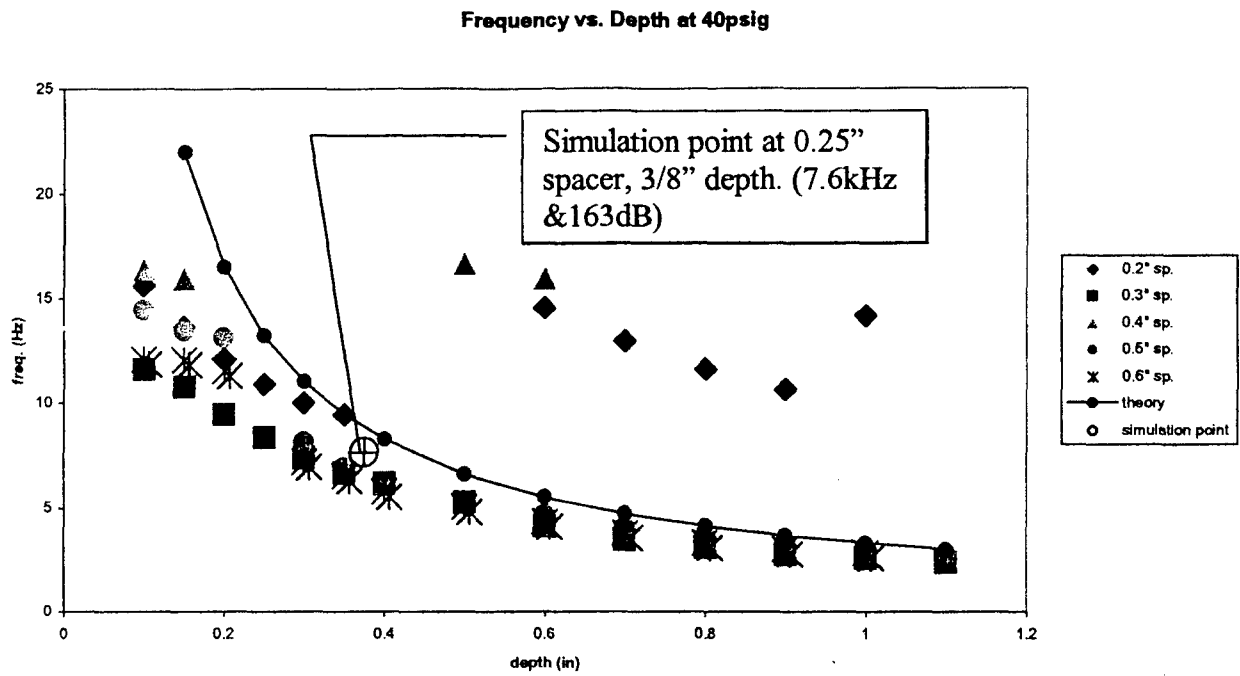


Fig. 2.10 Frequency vs. depth variation at 40 psig and various spacings

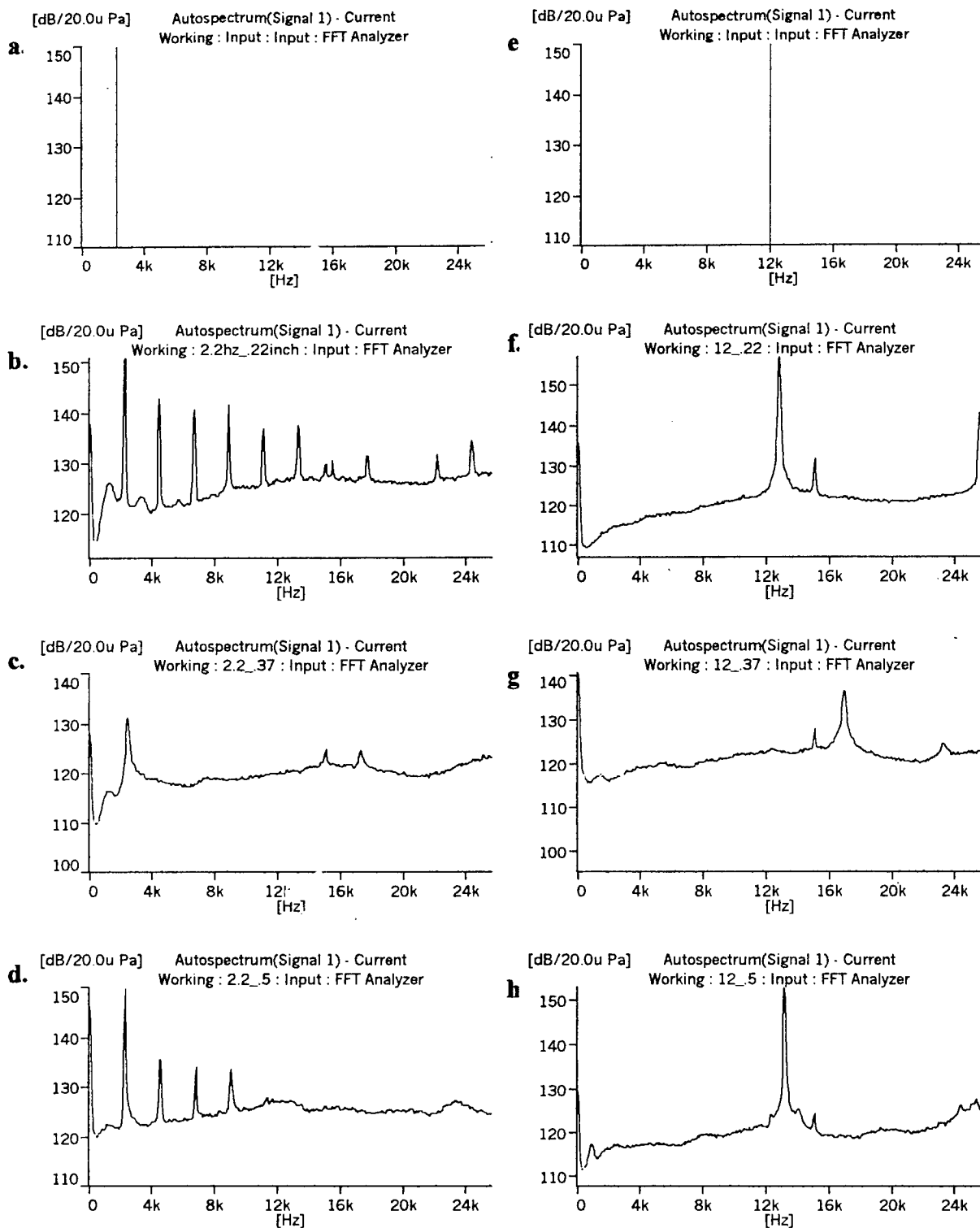


Fig. 2.11 Autospectrum of the resultant sound at 35psig. The spacing was changed as shown in table(2.1-a). (a-d) target frequency = 2.2 kHz. (e-h) target frequency = 12kHz.

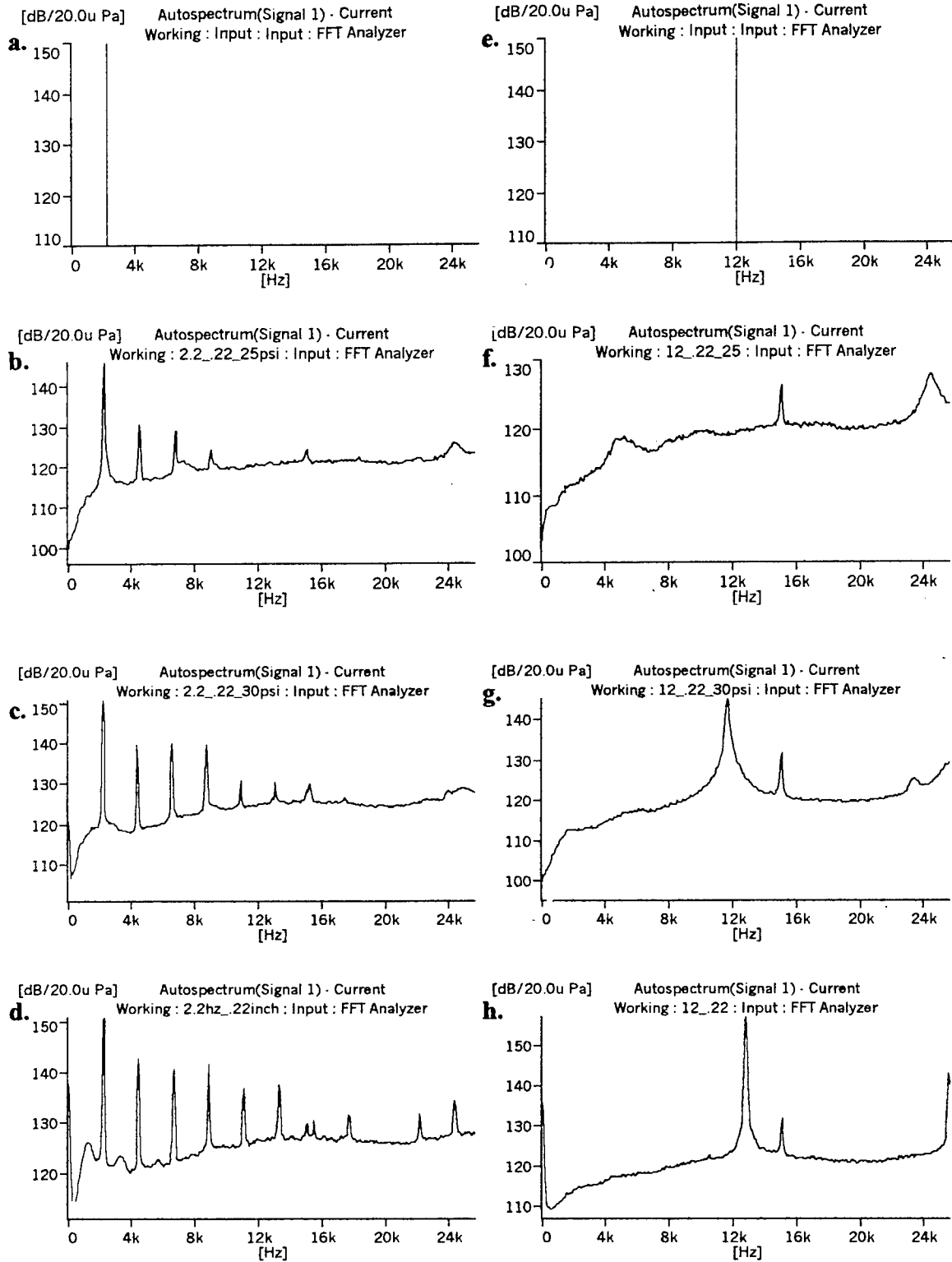


Fig. 2.12 Autospectrum of the resultant sound at 0.22 in spacing (between the supply jet and the resonance tube). The pressure was changed as shown in Table(2.1-b). (a-d) the target frequency = 2.2 kHz. (e-h) target frequency = 12kHz.

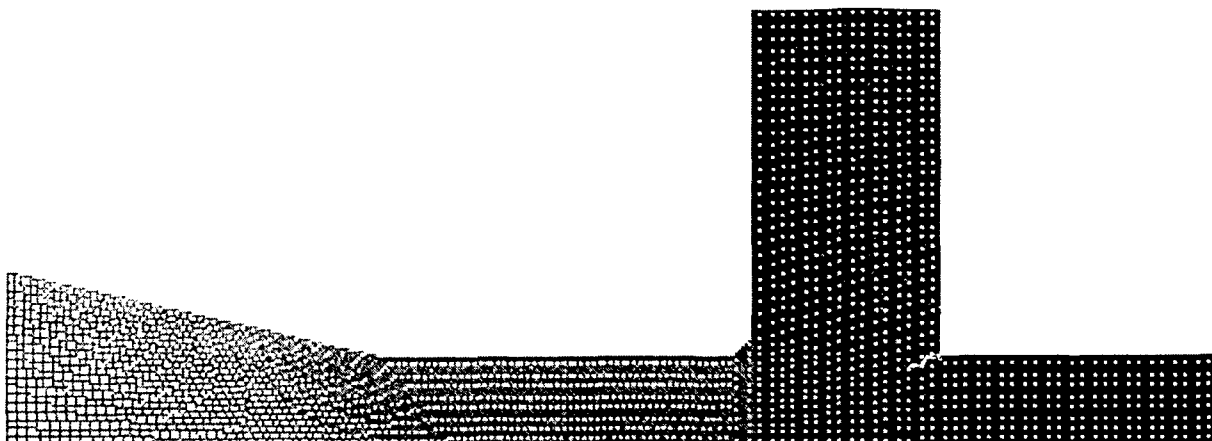


Fig. 3.1 A close-up view of zones 1-3. Supply tube is zone 1 with  $101 \times 21$  points, zone 2 is the integration slot with  $41 \times 101$  points, and zone 3 is the resonance tube with  $61 \times 21$  points.

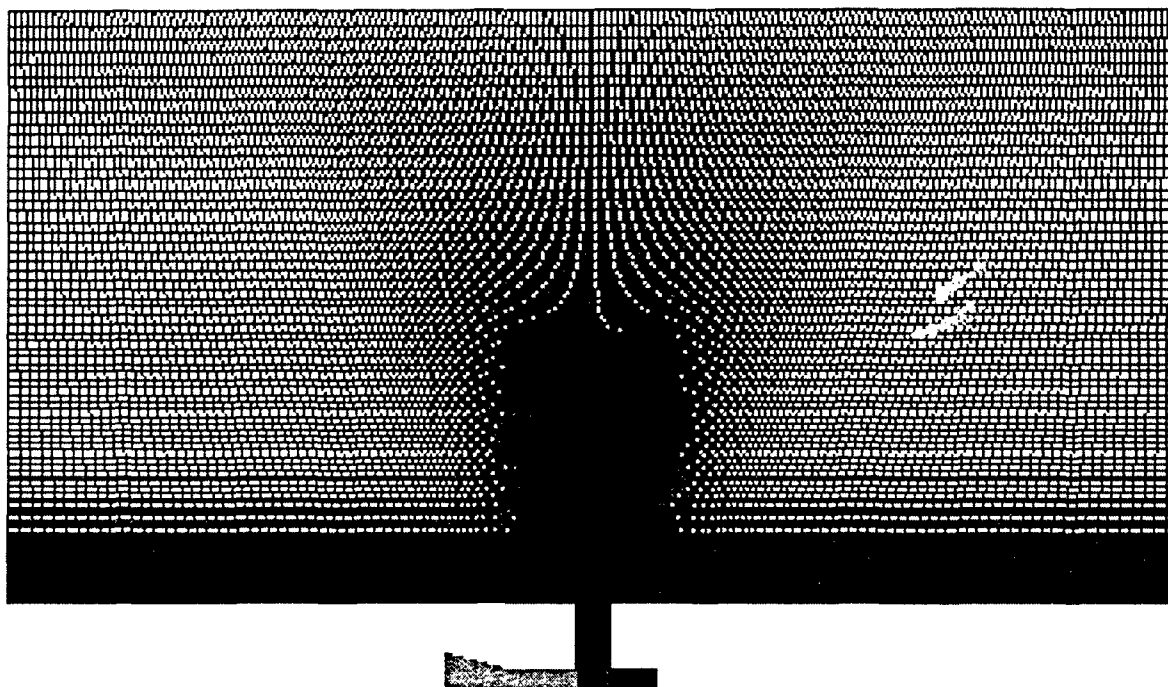
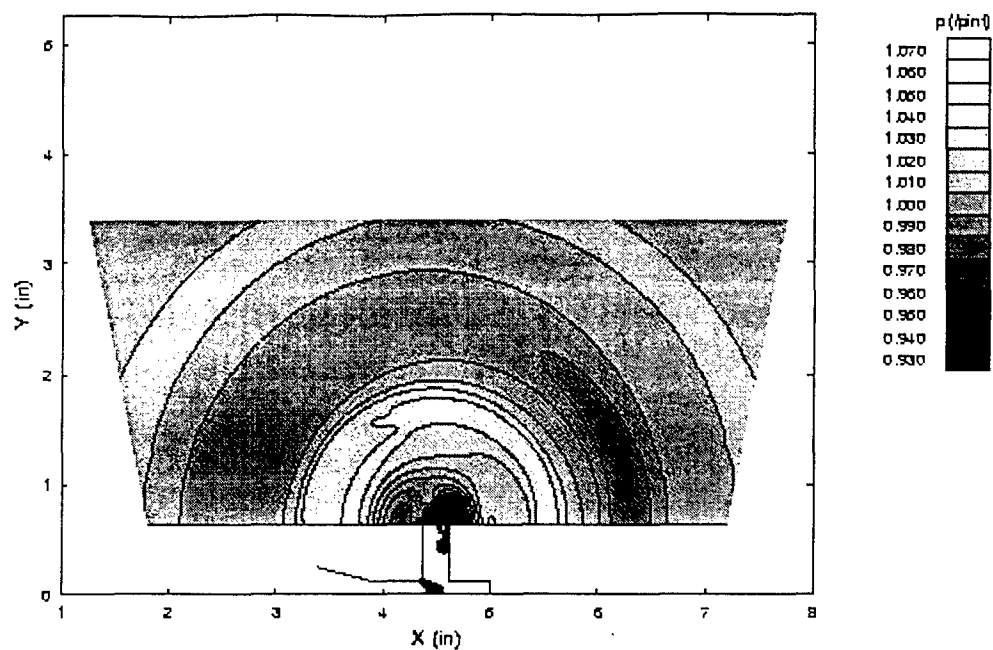
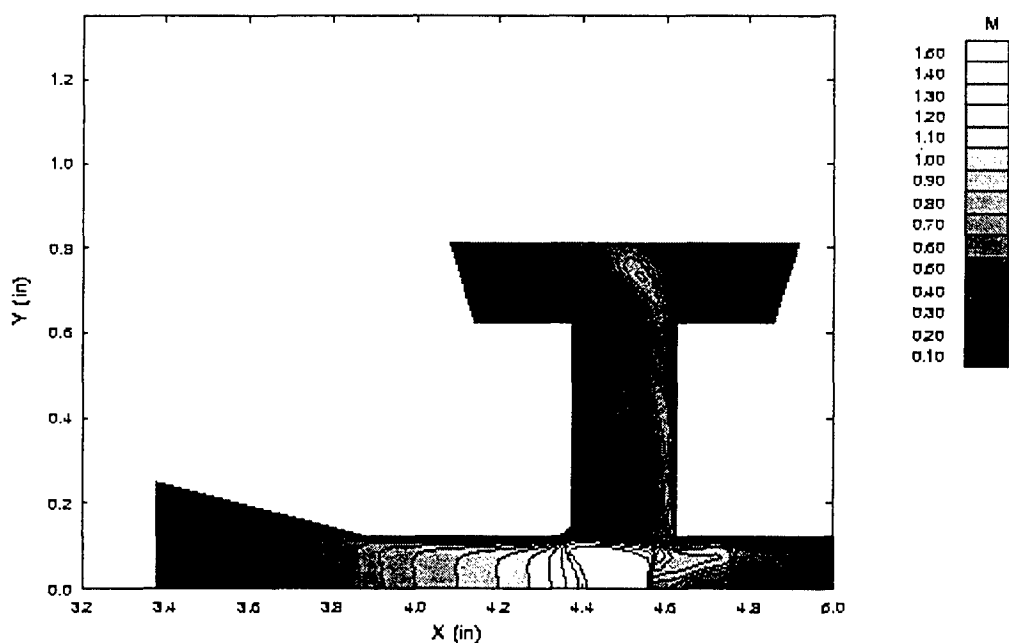


Fig. 3.2 The 4 zone grid used for the powered resonance tube simulations. Zone 4 is the far field with  $201 \times 101$  points. Zones 1-3 as described in Fig. 3.1.



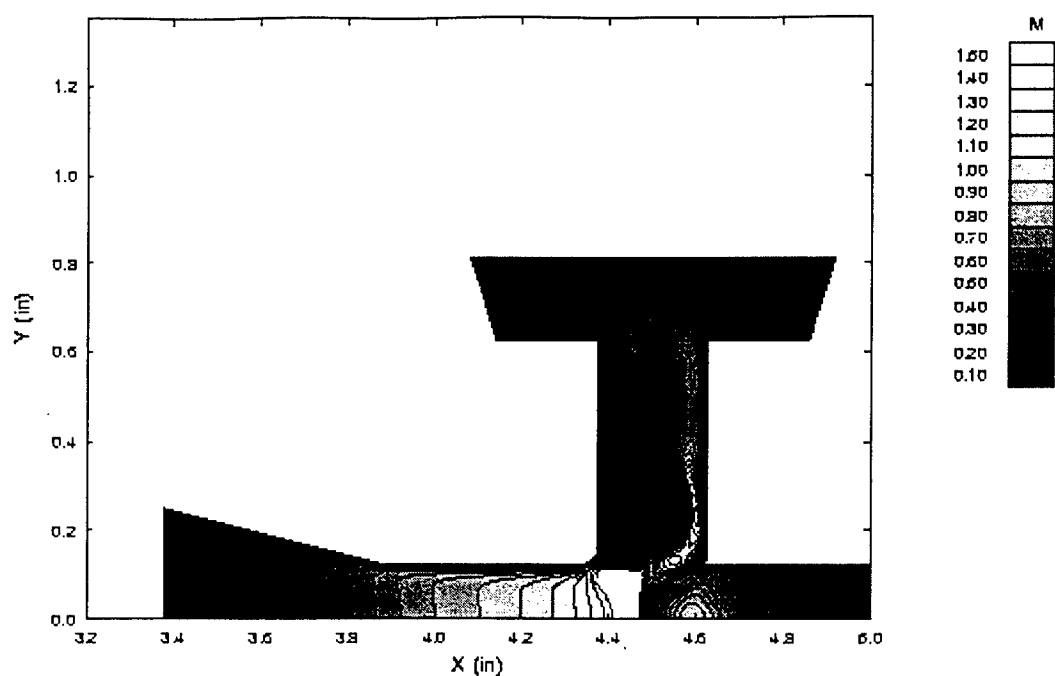
11-Jul-2001 14:17:00

Fig. 3.3 Pressure contours after 5250 timesteps for case F4-viscous walls.



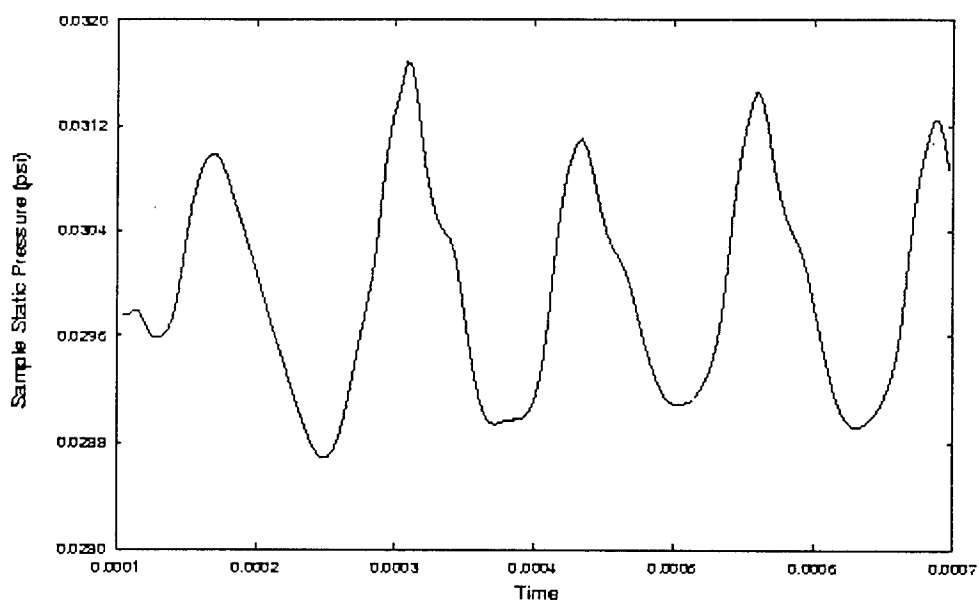
11-Jul-2001 14:16:03

Fig. 3.4 Mach contours in the supply tube, integration slot, and resonance tube corresponding to Fig. 3.3.



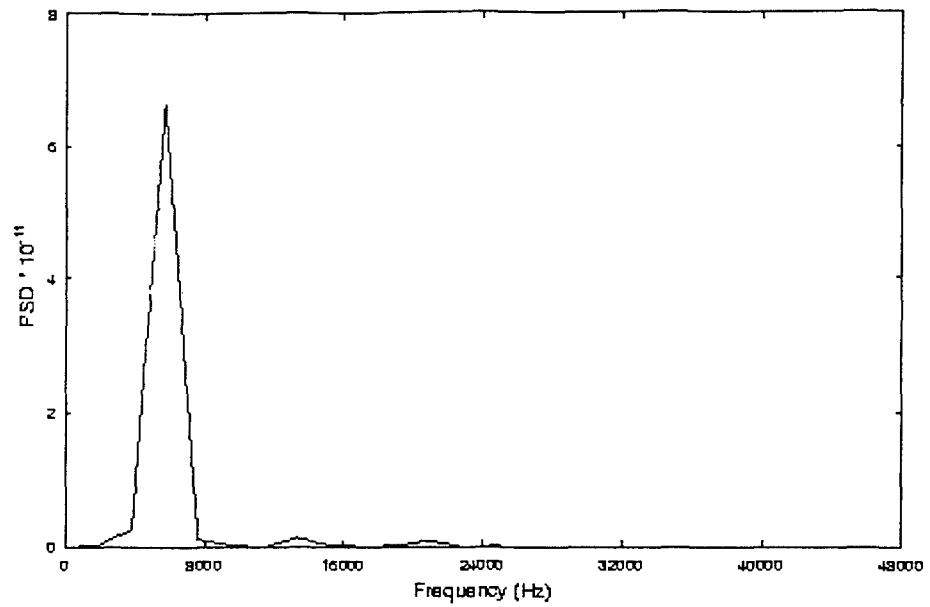
11-Jul-2001 14:19:41

Fig. 3.5 Mach contours for case in Fig. 3.4 but after only 3750 timesteps.



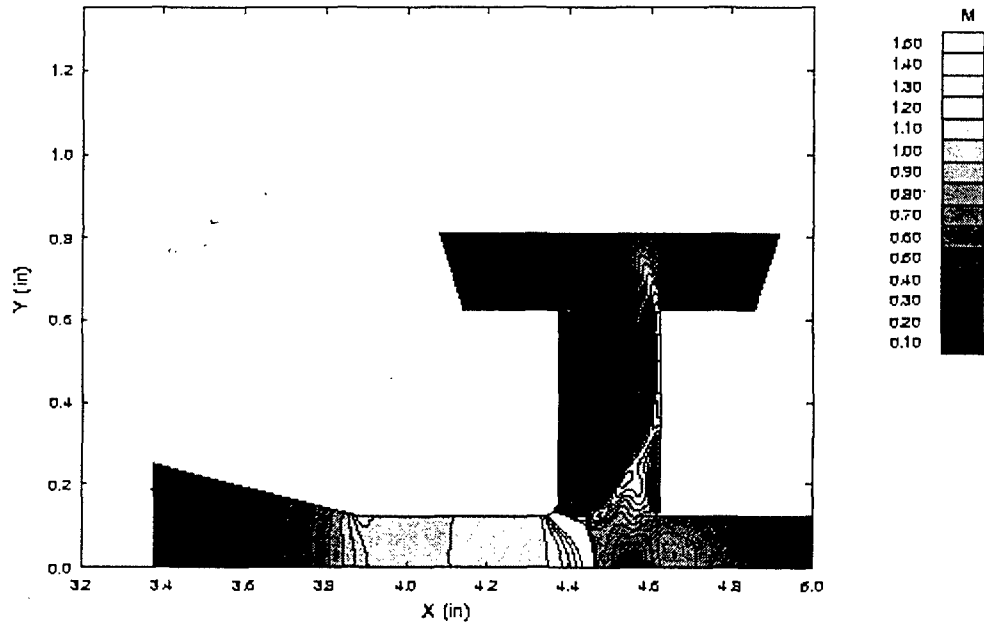
26-Jun-2001 12:24:33

Fig. 3.6 A time series of the pressure in the far field approximately 1/4" from the edge of the integration slot. This very closely approximates the microphone position in the IIT experiments.



01-Jul-2001 10:26:35

Fig. 3.7 The pressure spectral density from the F4 viscous wall case indicating resonance at approximately 7,600Hz.



11-Jul-2001 15:09:56

Fig. 3.8 A slip wall simulation comparable to the viscous wall calculation shown in Fig. 3.5.

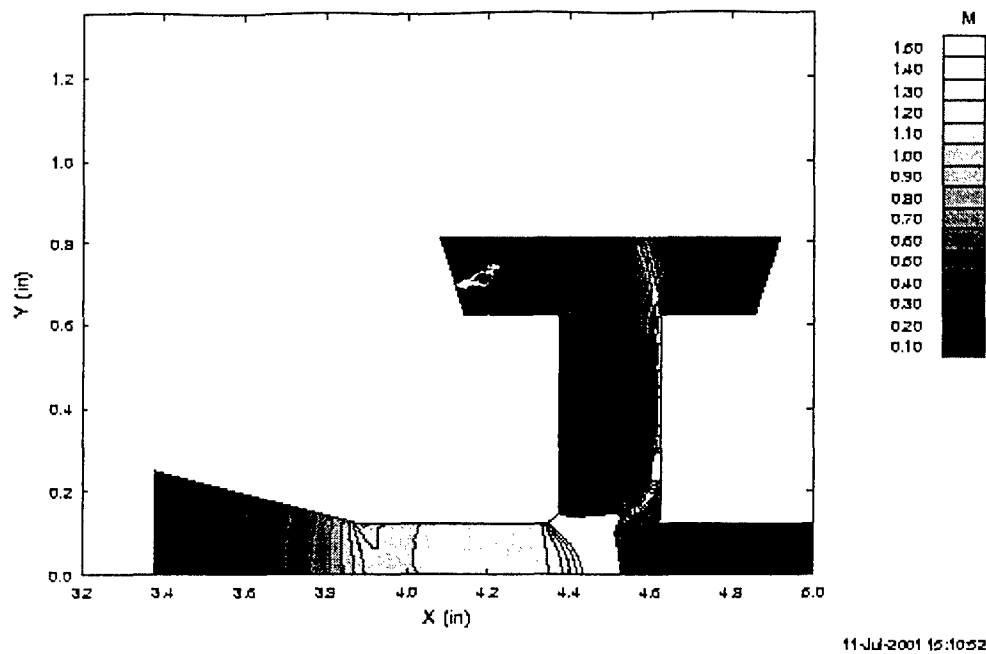


Fig. 3.9 A slip wall simulation comparable to the viscous wall calculation shown in Fig. 3.4.

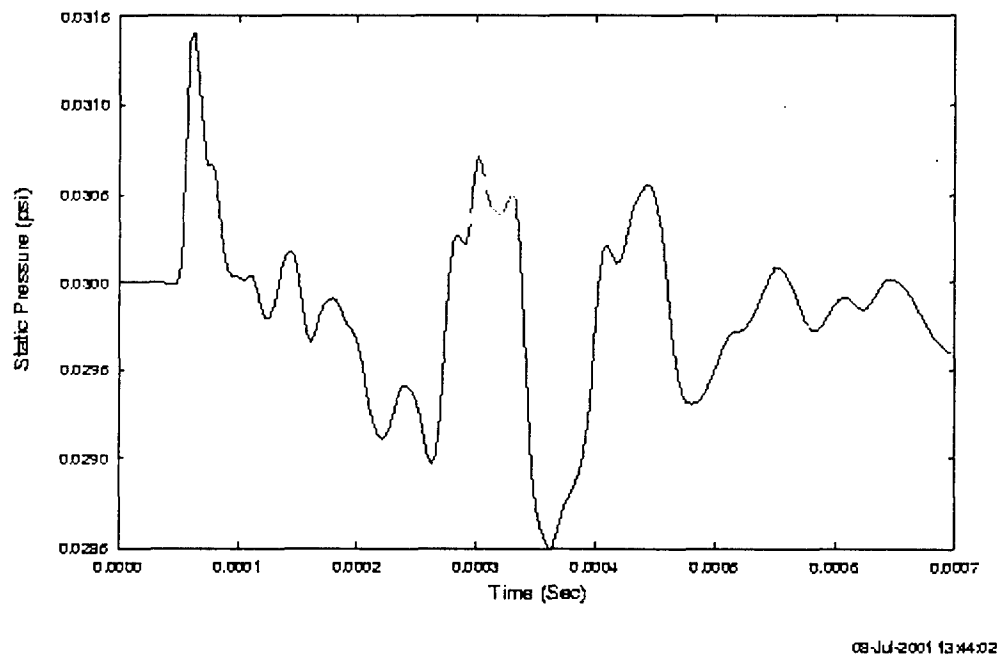


Fig. 3.10 A slip wall pressure time history corresponding to Fig. 3.6 showing the lack of a sustained resonance.

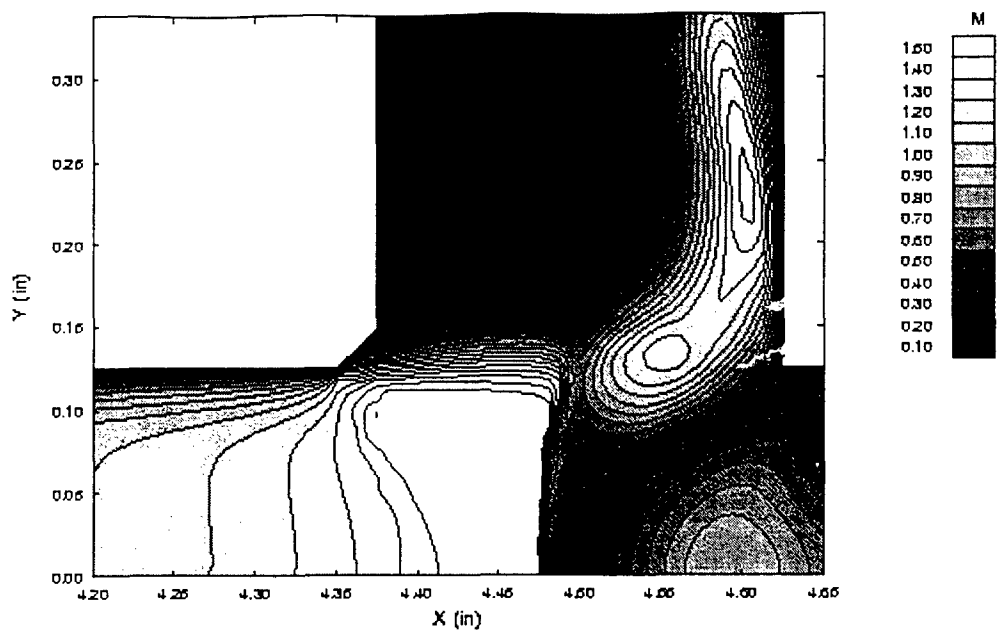


Fig. 3.11 An expanded view of the supply tube-integration slot-resonance tube region of Fig. 3.5.

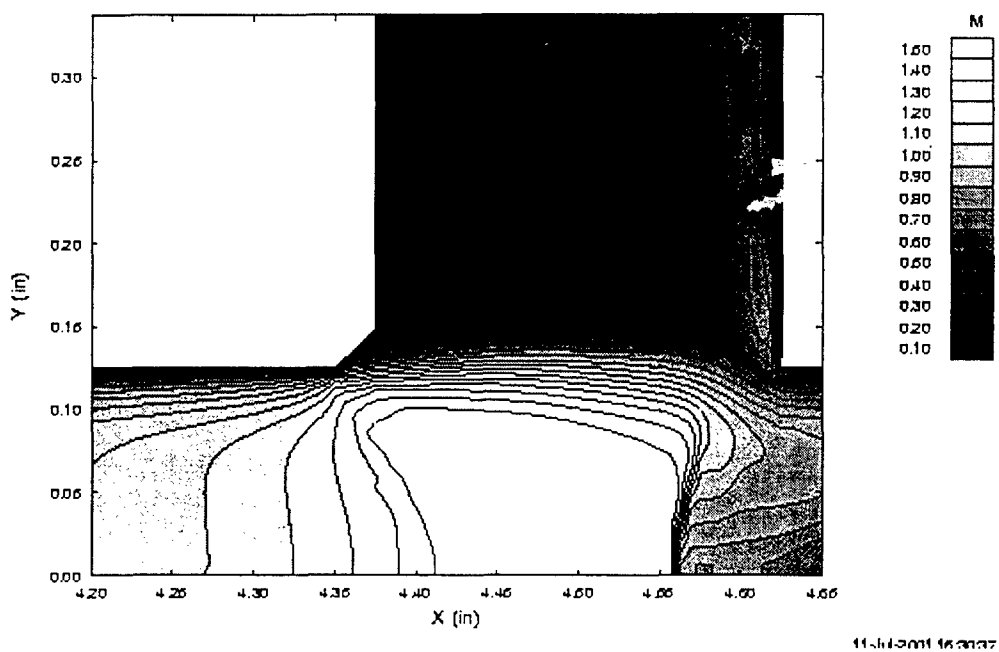


Fig. 3.12 An expanded view of the supply tube-integration slot-resonance tube region of Fig. 3.4.

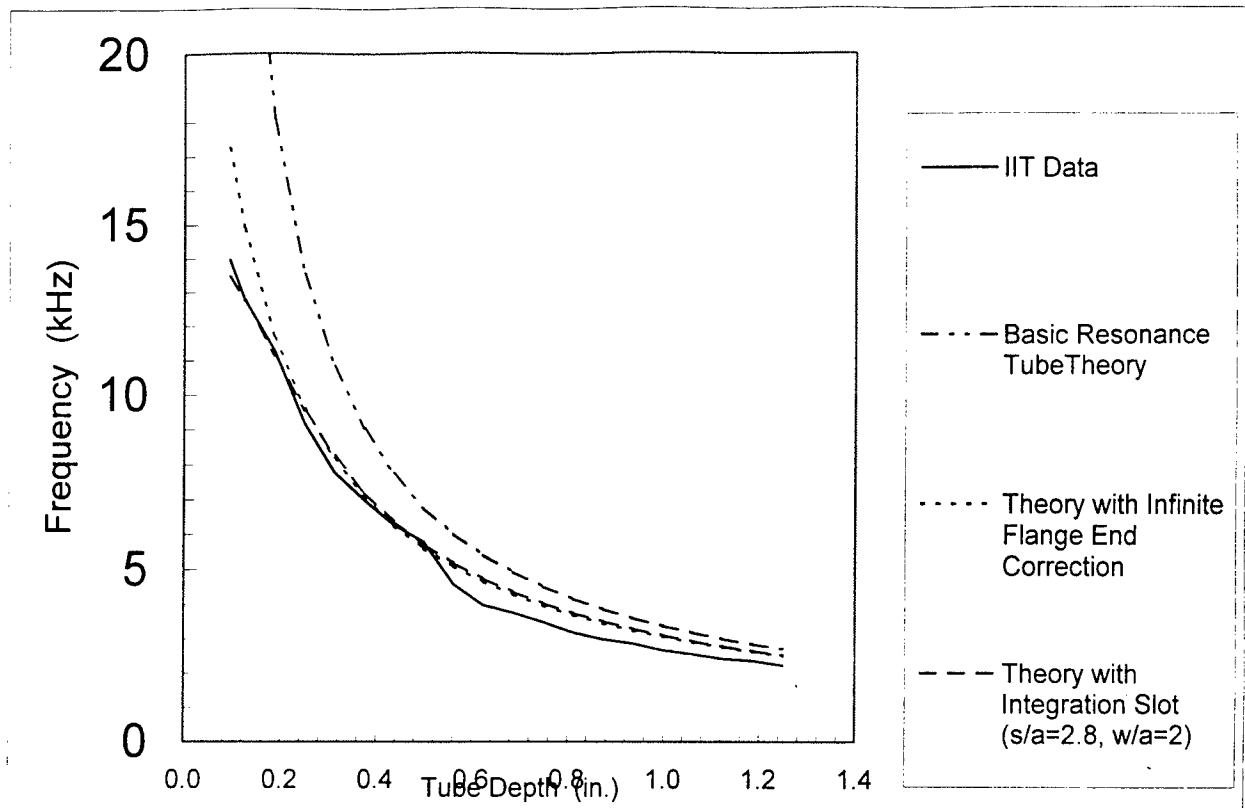


Fig 4.1 Theoretical predictions for the PRT actuator resonance frequency and comparison with IIT data. Tube radius  $a = 0.125$  in., integration slot width  $w = 0.25$  in.,  $p = 37$  psig.

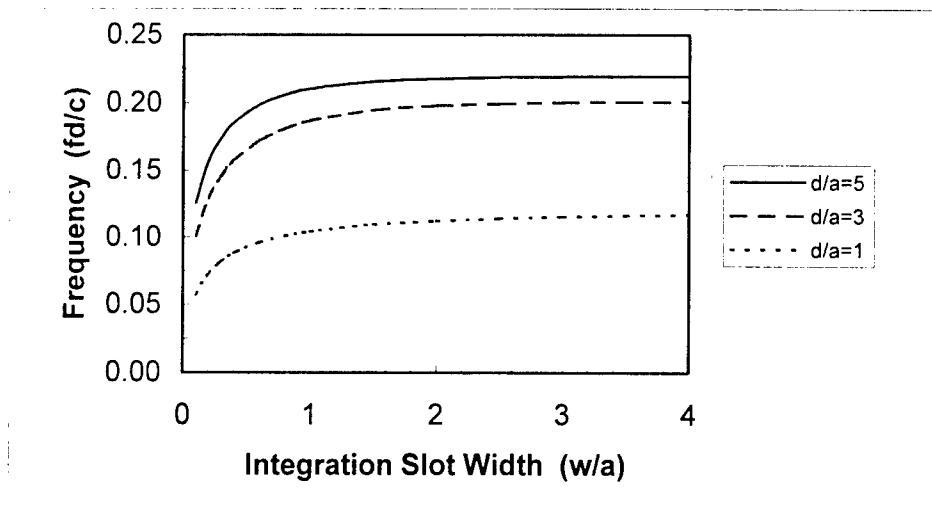


Fig 4.2 Influence of integration width on the PRT actuator resonance frequency, for slot radius  $s/a = 3$ . Frequency in the absence of an end correction is  $fd/c = 0.25$ .

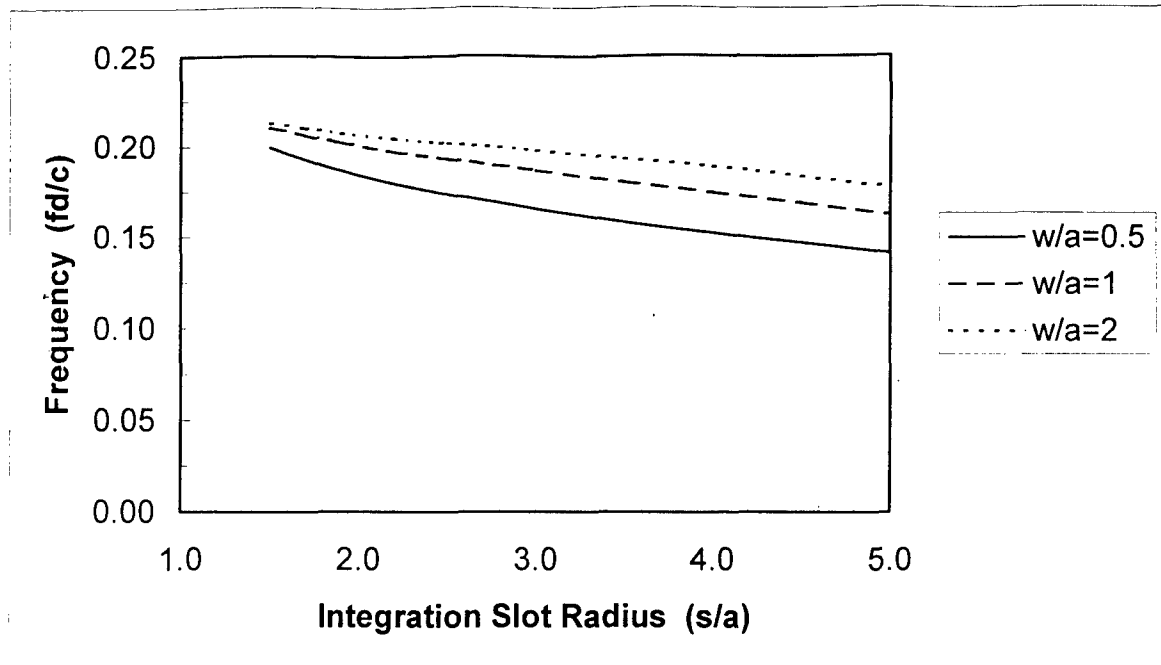


Fig. 4.3 Influence of integration slot radius on the PRT actuator resonance frequency, for tube depth  $d/a = 3$ . Frequency in the absence of an end correction is  $fd/c = 0.25$ .

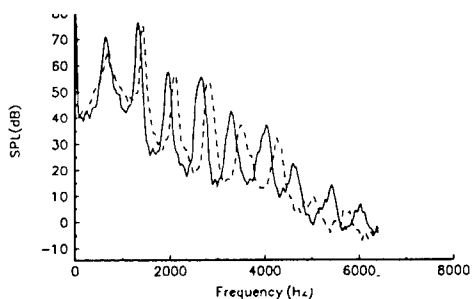


Fig. 5.1 Effect of high frequency excitation on an edgetone spectrum. Actuator: frequency 5,000Hz, displacement 0.2  $\mu\text{m}$ , Freestream speed  $M=0.07$ . Primary edgetone at 672 Hz. No forcing ———, with high frequency forcing - - - - -.

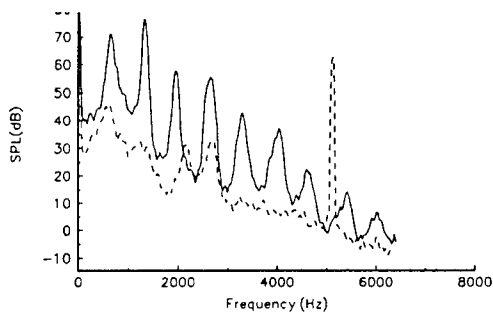


Fig. 5.2 Effect of high frequency excitation on an edgetone spectrum. Actuator: frequency 5,000Hz, displacement 6.0  $\mu\text{m}$ ,  $M=0.07$ . Primary edgetone at 672 Hz. No forcing ———, with high frequency forcing - - - - -.

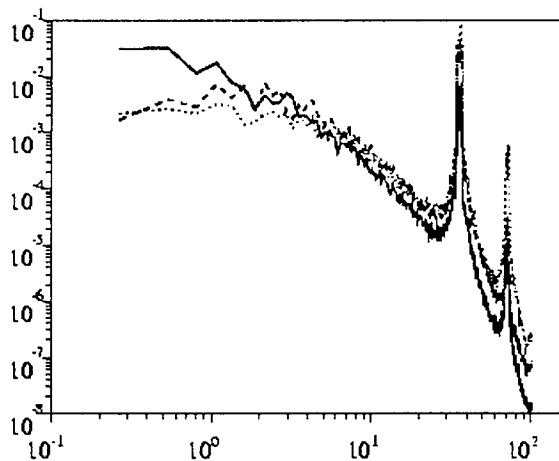


Fig. 5.3 Shear layer turbulent velocity x spectra after advancing 10 timesteps; case turb4.

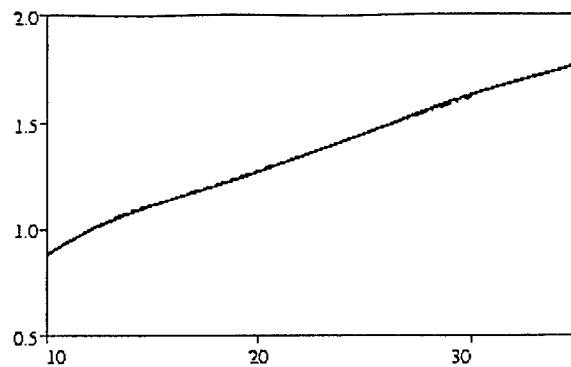


Fig. 5.4 Wake half width as a function of dimensionless time. Turb1 through turb4 and fwak cases plotted.

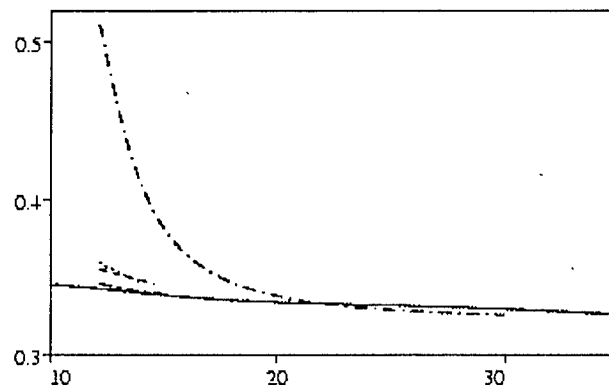


Fig. 5.5 Integrated turbulent kinetic energy, turbulent initial condition, as a function of dimensionless time. Reference case ———, turb4 high frequency forced case - - - - -.

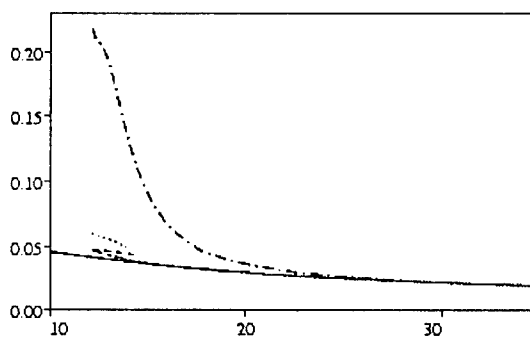


Fig. 5.6 Integrated dissipation rate as a function of dimensionless time. Turbulent initial condition. Reference case ———, turb4 case - - - - -.

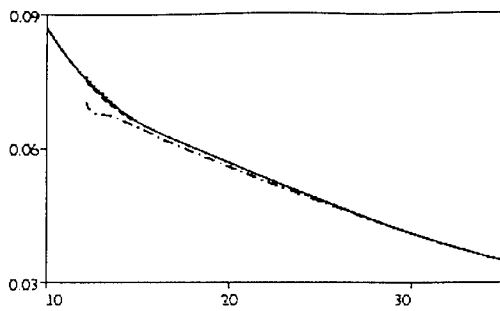


Fig. 5.7 Integrated rate of production of turbulent kinetic energy. Turbulent initial condition.  
Reference case —, turb4 case - - -.

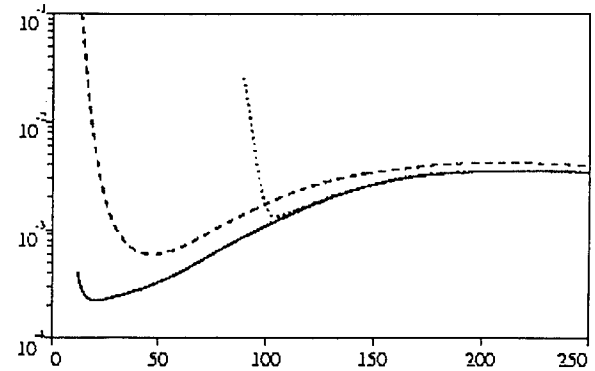


Fig. 5.10 Integrated dissipation rate as a function of dimensionless time. Transitional initial condition.  
Trans case —, ftrans case - - -, htrans case ····.

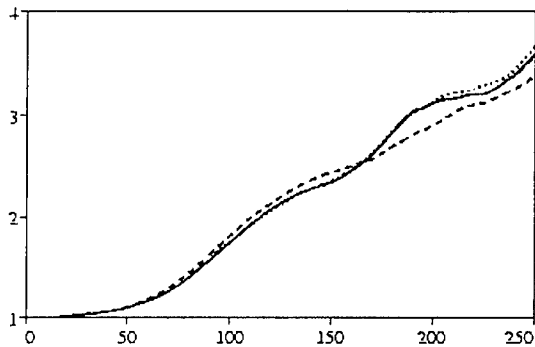


Fig. 5.8 Wake half width as a function of dimensionless time. Transitional initial conditions. Trans case —, ftrans case - - -, htrans case ····.

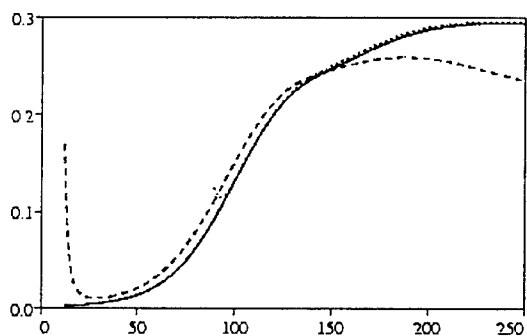


Fig. 5.9 Integrated turbulent kinetic energy as a function of dimensionless time. Transitional initial condition. Trans case —, ftrans case - - -.

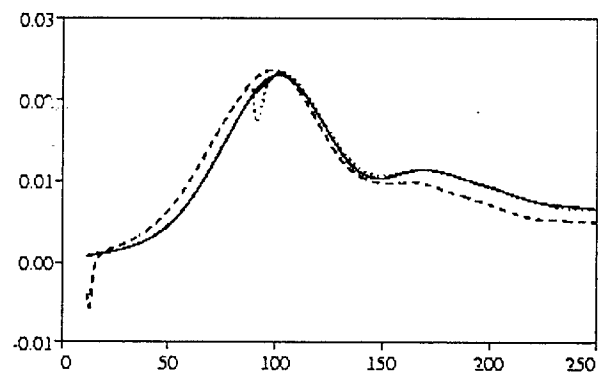


Fig. 5.11 Integrated rate of production of turbulent kinetic energy as a function of dimensionless time. Transitional initial condition.  
Trans case —, ftrans high frequency forcing - - -, htrans high frequency forcing ····.

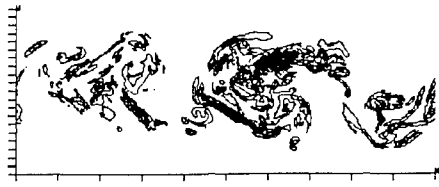


Fig. 5.12 Contours of -total vorticity at dimensionless time 200 for a transitional initial condition with **no high frequency forcing (trans)**.



Fig. 5.13 Contours of -total vorticity- at dimensionless time 200 for transitional Initial conditions with **high frequency forcing (ftrans)**.

**Appendix:**  
**Experimental data on the development of  
high bandwidth resonance tube actuators**

**List of captions for tables:**

Table 1. Frequency data at 27.5 psig supply pressure for various resonance tube depths and spacings.

Table 2. Sound Pressure Level (SPL) data at 27.5 psig supply pressure for various resonance tube depths and spacings.

Table 3. Frequency data at 30 psig supply pressure for various resonance tube depths and spacings.

Table 4. SPL data at 30 psig pressure for various resonance tube depths and spacings.

Table 5. Frequency data at 32.5 psig pressure for various resonance tube depths and spacings.

Table 6. SPL data at 32.5 psig pressure for various resonance tube depths and spacings.

Table 7. Frequency data at 35 psig pressure for various resonance tube depths and spacings.

Table 8. SPL data at 35 psig pressure for various resonance tube depths and spacings.

Table 9. Frequency data at 37.5 psig pressure pressure for various resonance tube depths and spacings.

Table 10. SPL Data at 37.5 psig pressure for various resonance tube depths and spacings.

Table 11. Frequency data at 40 psig pressure for various resonance tube depths and spacings.

Table 12. SPL data at 40 psig pressure for various resonance tube depths and spacings.

Table 13. Frequency data at 42.5 psig pressure pressure for various resonance tube depths and spacings.

Table 14. SPL data at 42.5 psig pressure pressure for various resonance tube depths and spacings.

Table 15. Frequency data for the lookup table method.

**List of figure captions:**

**Fig. 1.** Schematic drawing of a manually operated tunable high bandwidth resonance tube actuator.

**Fig. 2.** Schematic drawing of a PC controlled high bandwidth resonance tube actuator.

**Fig. 3.** Photograph of the PC controlled high bandwidth resonance tube actuator.

**Fig. 4.** Sound Pressure Level (SPL) mapping for various spacings (between the supply jet and resonance tube) and resonance tube depths at a supply pressure of 27.5 psig.

**Fig. 5.** Sound Pressure Level (SPL) mapping for various spacings (between the supply jet and resonance tube) and resonance tube depths at a supply pressure of 30 psig.

**Fig. 6.** Sound Pressure Level (SPL) mapping for various spacings (between the supply jet and resonance tube) and resonance tube depths at a supply pressure of 32.5 psig.

**Fig. 7.** Sound Pressure Level (SPL) mapping for various spacings (between the supply jet and resonance tube) and resonance tube depths at a supply pressure of 35 psig.

**Fig. 8.** Sound Pressure Level (SPL) mapping for various spacings (between the supply jet and resonance tube) and resonance tube depths at a supply pressure of 37.5 psig.

**Fig. 9.** Sound Pressure Level (SPL) mapping for various spacings (between the supply jet and resonance tube) and resonance tube depths at a supply pressure of 40 psig.

**Fig. 10.** Sound Pressure Level (SPL) mapping for various spacings (between the supply jet and resonance tube) and resonance tube depths at a supply pressure of 42.5 psig.

**Fig. 11.** Sound Pressure Level (SPL) mapping for various spacings (between the supply jet and resonance tube) and supply pressures at a resonance tube depth of 0.1 inch.

**Fig. 12.** Sound Pressure Level (SPL) mapping for various spacings (between the supply jet and resonance tube) and supply pressures at a resonance tube depth of 0.3 inch.

**Fig. 13.** Sound Pressure Level (SPL) mapping for various spacings (between the supply jet and resonance tube) and supply pressures at a resonance tube depth of 0.6 inch.

**Fig. 14.** Sound Pressure Level (SPL) mapping for various spacings (between the supply jet and resonance tube) and supply pressures at a resonance tube depth of 0.9 inch.

**Fig. 15.** Sound Pressure Level (SPL) mapping for various spacings (between the supply jet and resonance tube) and supply pressures at a resonance tube depth of 1.1 inch.

**Fig. 16.** Frequency vs. depth variation at 27.5 psig and various spacings.

- Fig. 17.** Frequency vs. depth variation at 30 psig and various spacings.
- Fig. 18.** Frequency vs. depth variation at 32.5 psig and various spacings.
- Fig. 19.** Frequency vs. depth variation at 35 psig and various spacings.
- Fig. 20.** Frequency vs. depth variation at 37.5 psig and various spacings.
- Fig. 21.** Frequency vs. depth variation at 42.5 psig and various spacings.
- Fig. 22.** Frequency vs. depth variation at 37.5 psig pressure, 0.3" spacing and 1/8" diameter.
- Fig. 23.** SPL vs. depth variation at 37.5 psig pressure, 0.3" spacing and 1/8" diameter.
- Fig. 24.** Auto spectrum at 0.2" spacing, 0.1" depth and 40psig.
- Fig. 25.** Auto spectrum at 0.2" spacing, 0.2" depth and 40psig.
- Fig. 26.** Auto spectrum at 0.2" spacing, 0.3" depth and 40psig.
- Fig. 27.** Auto spectrum at 0.2" spacing, 0.4" depth and 40psig.
- Fig. 28.** Auto spectrum at 0.3" spacing, 0.25" depth and 40psig.
- Fig. 29.** Auto spectrum at 0.3" spacing, 1.1" depth and 40psig.
- Fig. 30.** Auto spectrum at 0.4" spacing, 0.6" depth and 35psig.
- Fig. 31.** Auto spectrum at 0.5" spacing, 0.15" depth and 35psig.
- Fig. 32.** Auto spectrum at 0.6" spacing, 0.15" depth and 35psig.
- Fig. 33.** Auto spectrum at 0.2" spacing, 0.1" depth and 30psig.
- Fig. 34.** Auto spectrum at 0.2" spacing, 0.3" depth and 30psig.
- Fig. 35.** Auto spectrum at 0.2" spacing, 1.0" depth and 30psig.
- Fig. 36.** Auto spectrum at 0.4" spacing, 0.6" depth and 30psig.
- Fig. 37.** Auto spectrum at 0.5" spacing, 1.1" depth and 30psig.

**Note:** yellow regions represent situations where frequency does not vary with change in tube depth or situations where frequency jumps occur.

		p=27.5						
d \ sp		0.1	0.2	0.3	0.4	0.5	0.6	0.7
0.1				19.58	15.1	13.25	11.52	22.53
0.15				17.34	14.53	12.86	11.46	15.55
0.2					14.78	12.61	11.2	15.3
0.25			8.576					9.792
0.3			7.872		7.51			9.6
0.35			6.976	6.528	6.528		10.75	14.66
0.4			6.272		5.824			
0.5			5.184	5.12	5.056			
0.6			4.224	4.48	4.544	4.288	8.576	4.608
0.7			3.712	3.968	3.84	3.84		7.424
0.8			3.392	3.648	3.456	3.584		
0.9			3.008	3.264	3.136	3.136	3.584	
1			2.816	2.944	2.88	3.136	2.88	
1.1			2.624	2.816	2.624	2.624		

**Table 1.** Frequency data at 27.5 psig supply pressure for various resonance tube depths and spacings.

		p=27.5 psig						
d \ sp		0.1	0.2	0.3	0.4	0.5	0.6	0.7
0.1				134	143	148	133	148
0.15				129	150	146	155	148
0.2								140
0.25			127					143
0.3			126		128			132
0.35			128	125	146		130	
0.4			139		153			
0.5			126	128	152			
0.6			127	128	149	124	136	135
0.7			136	131	152	145		
0.8			134	136	150	122		
0.9			143	129	150	127	129	
1			145	129	147	119	129	
1.1			144	124	148	135		

**Table 2.** Sound Pressure Level (SPL) data at 27.5 psig supply pressure for various resonance tube depths and spacings.

		p=30						
d \ sp		0.1	0.2	0.3	0.4	0.5	0.6	0.7
0.1				19.9	15.23	13.38	11.65	22.85
0.15				20.1	14.66	12.93	11.58	15.74
0.2			9.792		14.78	12.86	11.33	10.3
0.25			8.832		8.448			9.984
0.3			7.808		7.04			9.856
0.35			7.232		6.592			22.6
0.4			6.336	20.2	5.952			22.65
0.5			5.248	5.056	5.376			22.45
0.6			4.352	4.416	4.48	4.352		22.54
0.7			3.776	3.84	3.904	3.904		22.45
0.8			3.92	3.584	3.584	3.456	11.33	22.45
0.9			3.072	3.264	3.2	3.136		10.11
1			2.816	3.008	2.944	2.944	2.88	22.45
1.1			2.624	20.1	2.752	2.624		22.55

**Table 3.** Frequency data at 30 psig supply pressure for various resonance tube depths and spacings.

		p=30 psig						
d \ sp		0.1	0.2	0.3	0.4	0.5	0.6	0.7
0.1				145	151	151	132	
0.15								148
0.2			137					145
0.25			152		135			146
0.3			155		138			131
0.35			155		146			
0.4			156		153			
0.5			150	136	149			
0.6			150	141	152	127		
0.7			152	127	152	145		
0.8			151	142	151	123		
0.9			150	140	150	124		141
1			150	138	148	124	131	
1.1			146		147	128		

**Table 4.** SPL data at 30 psig supply pressure for various resonance tube depths and spacings.

		p=32.5						
d \ sp		0.1	0.2	0.3	0.4	0.5	0.6	0.7
0.1				20.16	15.42	13.44		22.98
0.15			11.52	20.1	14.78	12.99	11.58	15.74
0.2			10.24	20.29	14.98	12.74	11.33	10.37
0.25			9.152	20.42	9.472	12.8		9.984
0.3			8.192	20.45		12.67		23
0.35			7.488	20.67	6.336			
0.4			6.784	20.48	6.016			
0.5			5.184	19.97	5.696	4.992		5.056
0.6			4.416	4.352	4.48	4.41		4.736
0.7			3.84	3.84	3.968	3.904		
0.8			3.456	3.456	3.648	3.392	11.53	
0.9			3.136	3.2	3.264	3.136		10.11
1			2.816	2.944	3.072	2.816	2.88	
1.1			2.624	2.624	2.752	2.688		

**Table 5.** Frequency data at 32.5 psig supply pressure for various resonance tube depths and spacings.

d/sp	p=32.5 psig						
	0.1	0.2	0.3	0.4	0.5	0.6	0.7
0.1			146	142	151		150
0.15		145				150	145
0.2		154					146
0.25		156		128			141
0.3		158					
0.35		158		128			
0.4		151		143			
0.5		158		140	130		131
0.6		157	133	150	137		135
0.7		156	128	148	149		
0.8		153	129	150	130		
0.9		152	135	147	134		
1		151	138	147	137	130	
1.1		150	128	145	134		

**Table 6.** SPL data at 32.5 psig supply pressure for various resonance tube depths and spacings.

		p=35						
d \ sp		0.1	0.2	0.3	0.4	0.5	0.6	0.7
0.1				20.42	15.68	13.82		
0.15			12.42	20.42	15.1	13.18	11.65	
0.2			10.94	20.61	15.36	12.8	11.39	10.43
0.25			9.6	20.61	15.42	12.99		10.24
0.3			8.96	20.61		12.93		
0.35			7.936	20.61		6.336		
0.4			7.424	20.61		5.888		
0.5			5.312	20.1	16.76	5.056		
0.6			4.544	20.16	4.416	4.48		
0.7			3.968	3.712	4.096	3.968	11.84	
0.8			3.52	3.328	3.712	3.456	11.39	
0.9			3.2	3.008	3.392	3.2		
1			2.944	2.752	3.072	2.88	2.816	
1.1			2.688	2.56	2.816	2.688		

**Table 7.** Frequency data at 35 psig supply pressure for various resonance tube depths and spacings.

		p=35 psig						
d \ sp		0.1	0.2	0.3	0.4	0.5	0.6	0.7
0.1					146	153		
0.15			154				150	
0.2			155					141
0.25			153					134
0.3			156					
0.35			152			133		
0.4			137			139		
0.5			158			140		
0.6			157		143	136		
0.7			156	128	132	146		
0.8			155	130	140	138		
0.9			154	132	130	134		
1			153	139	144	138	135	
1.1			152	141	126	134		

**Table 8.** SPL data at 35 psig supply pressure for various resonance tube depths and spacings.

		p=37.5						
d \ sp		0.1	0.2	0.3	0.4	0.5	0.6	0.7
	0.1		14.66	20.16	16.06	13.95		
	0.15		12.86		15.36	13.18	11.71	
	0.2		11.2		15.49	12.8	11.39	10.37
	0.25		9.792		15.49	12.93		10.18
	0.3		9.152			7.744		
	0.35		8.192			6.656		
	0.4		7.616		6.144	6.016		
	0.5		5.824		16.25	5.248	4.928	
	0.6		13.12		15.7	4.608	4.352	
	0.7		12.5	3.392	4.032	3.968	3.776	
	0.8		11.32	3.008	3.712	3.52	3.328	
	0.9		10.43	2.752	16.12	3.136	3.008	
	1		9.75	2.56	3.072	2.88	2.816	128
	1.1		2.688	2.368	2.816	2.688	2.56	

**Table 9.** Frequency data at 37.5 psig supply pressure for various resonance tube depths and spacings.

		p=37.5 psig						
d \ sp		0.1	0.2	0.3	0.4	0.5	0.6	0.7
0.1			139	133	147	148		
0.15			155				152	
0.2			156					136
0.25			157					135
0.3			157			130		
0.35			136			132		
0.4			144		131	139		
0.5			130			140	141	
0.6						140	131	
0.7				133	130	136	136	
0.8				152	132	140	134	
0.9				153		134	144	
1				151	140	137	143	
1.1			152	150	126	134	145	

**Table 10.** SPL Data at 37.5 psig supply pressure for various resonance tube depths and spacings.

		p=40						
d \ sp		0.1	0.2	0.3	0.4	0.5	0.6	0.7
0.1			15.62	11.58	16.38	14.46	12.08	17.79
0.15			13.63	10.75	15.94	13.44	12.03	10.88
0.2			12.1	9.408		13.12	11.52	10.56
0.25			10.88	8.32				10.37
0.3			9.984	7.36		8.128	7.168	
0.35			9.408	6.656		6.912	6.528	
0.4				6.144	6.08	6.144	5.76	7.808
0.5				5.248	16.64	5.312	5.056	
0.6			14.53	4.096	15.95	4.672	4.352	
0.7			12.93	3.456	3.904	4.032	3.776	3.904
0.8			11.58	3.072	3.52	3.648	3.328	3.328
0.9			10.62	2.752	3.2	3.264	3.008	3.2
1			14.14	2.56	2.88	3.008	2.816	2.816
1.1				2.368	2.688	2.752		

**Table 11.** Frequency data at 40 psig supply pressure for various resonance tube depths and spacings.

		p=40 psig						
d \ sp		0.1	0.2	0.3	0.4	0.5	0.6	0.7
0.1			136	137	149	135	151	134
0.15			152	154		138		
0.2			150	156				141
0.25			150	155				136
0.3			135	151		130	135	
0.35			126	157		131	139	
0.4				156	141	136	145	134
0.5				154		135	148	
0.6				154		135	147	
0.7				154	139	134	146	134
0.8				152	144	138	144	134
0.9				152	132	132	146	129
1				149	136	135	144	133
1.1				150	139	130	144	

**Table 12.** SPL data at 40 psig supply pressure for various resonance tube depths and spacings.

		p=42.5						
d \ sp		0.1	0.2	0.3	0.4	0.5	0.6	0.7
	0.1		15.81	11.46	16.38		12.8	17.73
	0.15		13.76	10.75	15.68	13.38	12.03	
	0.2		12.16	9.408		13.12	11.46	10.5
	0.25		11.07	8.32			8.256	10.3
	0.3		10.05	7.296			7.168	10.24
	0.35			6.592	6.528	6.912	6.464	7.616
	0.4			6.144	5.952	6.144	5.76	7.808
	0.5		16.45	5.056	5.12	5.504	5.056	4.992
	0.6		14.46	4.096	4.352	4.928	4.416	4.224
	0.7		12.8	3.456	3.84	4.096	3.776	3.84
	0.8		11.52	3.008	3.456	3.648	3.328	3.328
	0.9		10.5	2.752	3.136	3.328	3.008	3.136
	1		15.3	2.496	2.88	3.072	2.816	2.816
	1.1		14.14	2.368	2.624	2.816	2.56	

**Table 13.** Frequency data at 42.5 psig supply pressure for various resonance tube depths and spacings.

		p=42.5 psig						
d \ sp		0.1	0.2	0.3	0.4	0.5	0.6	0.7
0.1			144	140	147		153	133
0.15			154	155		138	155	
0.2			154	154			157	137
0.25			146	153			136	
0.3			129	152			140	
0.35				156	138	131	145	131
0.4				154	145	132	149	133
0.5				155	137	132	150	131
0.6				154	139	136	147	133
0.7				152	152	135	146	136
0.8				150	151	139	142	137
0.9				148	150	131	143	133
1				145	150	138	144	135
1.1				146	148	134	143	

**Table 14.** SPL data at 42.5 psig supply pressure for various resonance tube depths and spacings.

input frequency (kHz)	output frequency (kHz)	%error
2.5	2.56	2.40
3	3.008	0.27
4	4.023	0.57
5	4.992	0.16
6	6.144	2.40
7	6.976	0.34
8	8.046	0.57
9	9.216	2.40
10	10.3	3.00
11	11.65	5.91
12	12.42	3.50

**Table 15.** Frequency data for the lookup table method.

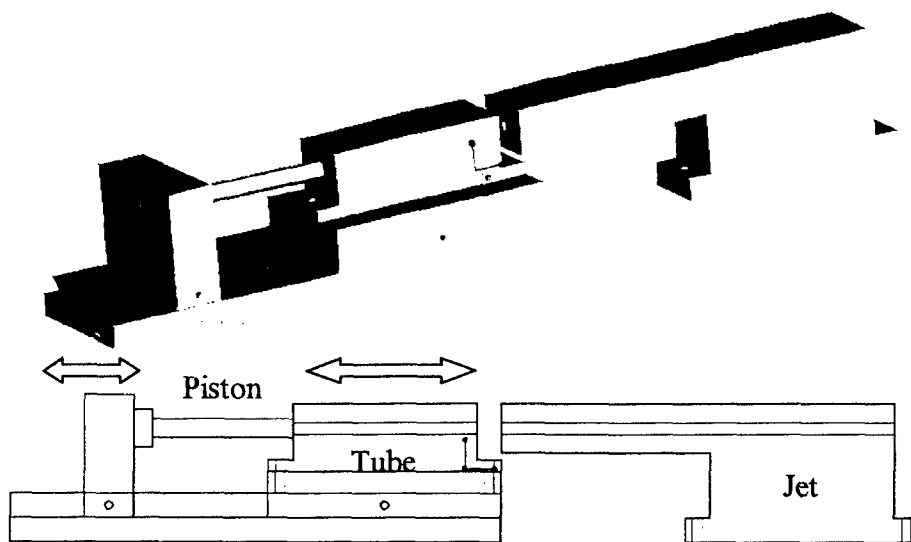


**Fig. 1.** Schematic drawing of a manually operated tunable high bandwidth resonance tube actuator.

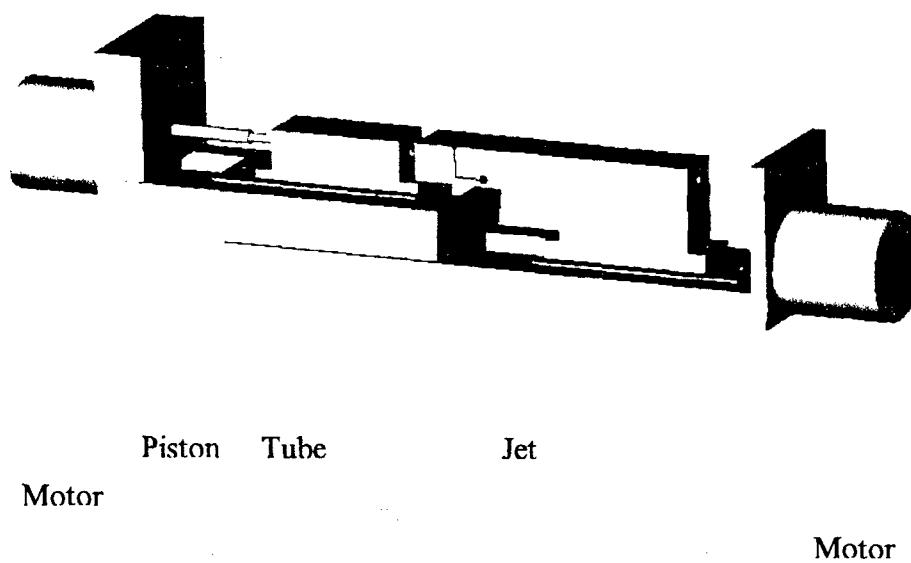


**Fig. 2.** Schematic drawing of a PC controlled high bandwidth resonance tube actuator.



**Fig. 3.** Photograph of the PC controlled high bandwidth resonance tube actuator.

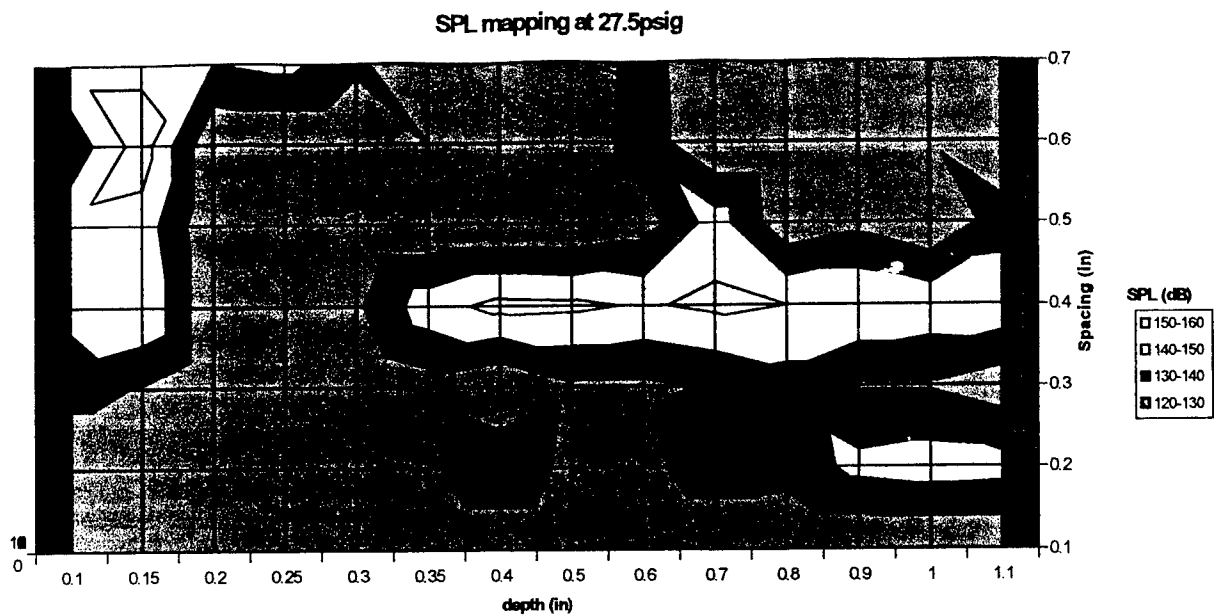


**Fig. 4.** Sound Pressure Level (SPL) mapping for various spacings (between the supply jet and the resonance tube) and resonance tube depths at a supply pressure of 27.5 psig.

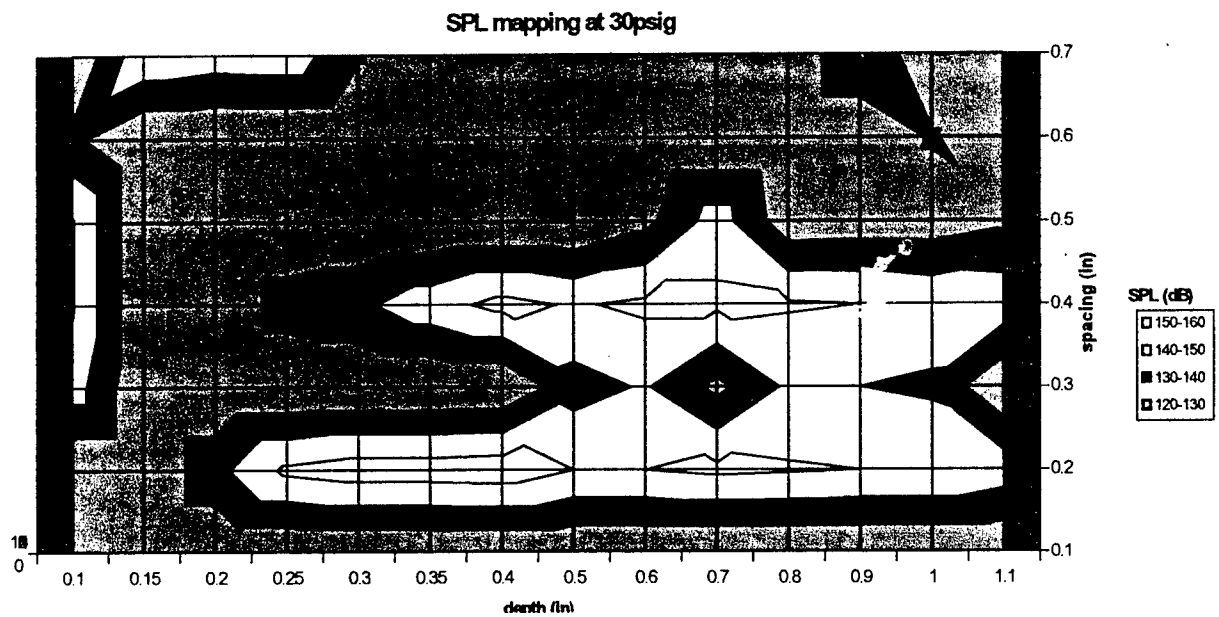


**Fig. 5.** Sound Pressure Level (SPL) mapping for various spacings (between the supply jet and the resonance tube) and resonance tube depths at a supply pressure of 30 psig.

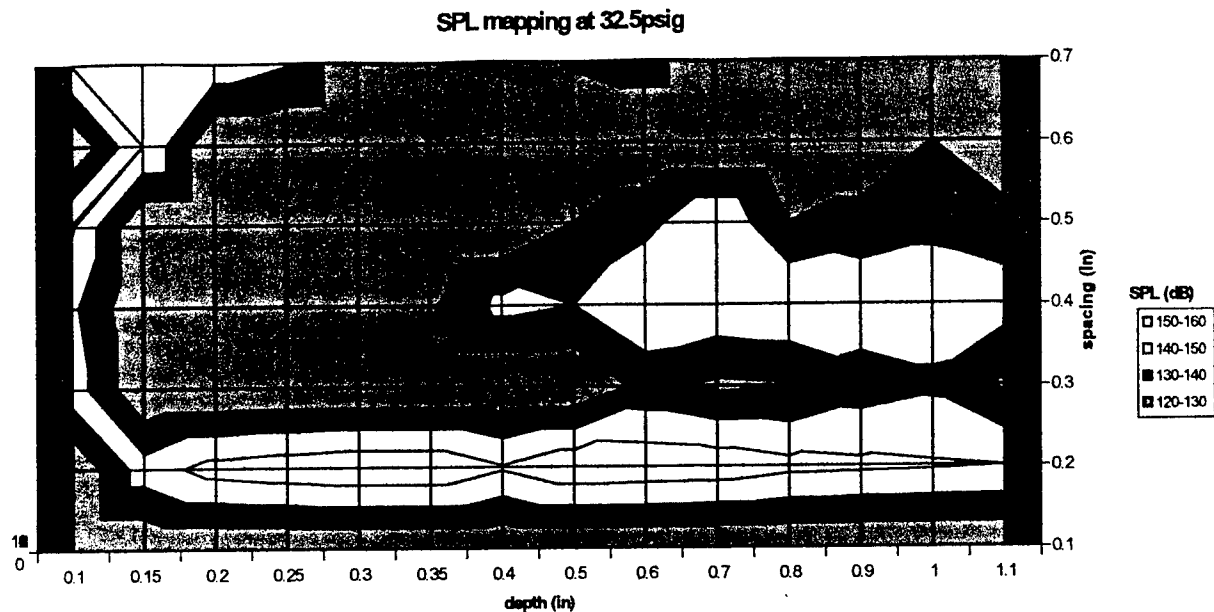


**Fig. 6.** Sound Pressure Level (SPL) mapping for various spacings (between the supply jet and the resonance tube) and resonance tube depths at a supply pressure of 32.5 psig.

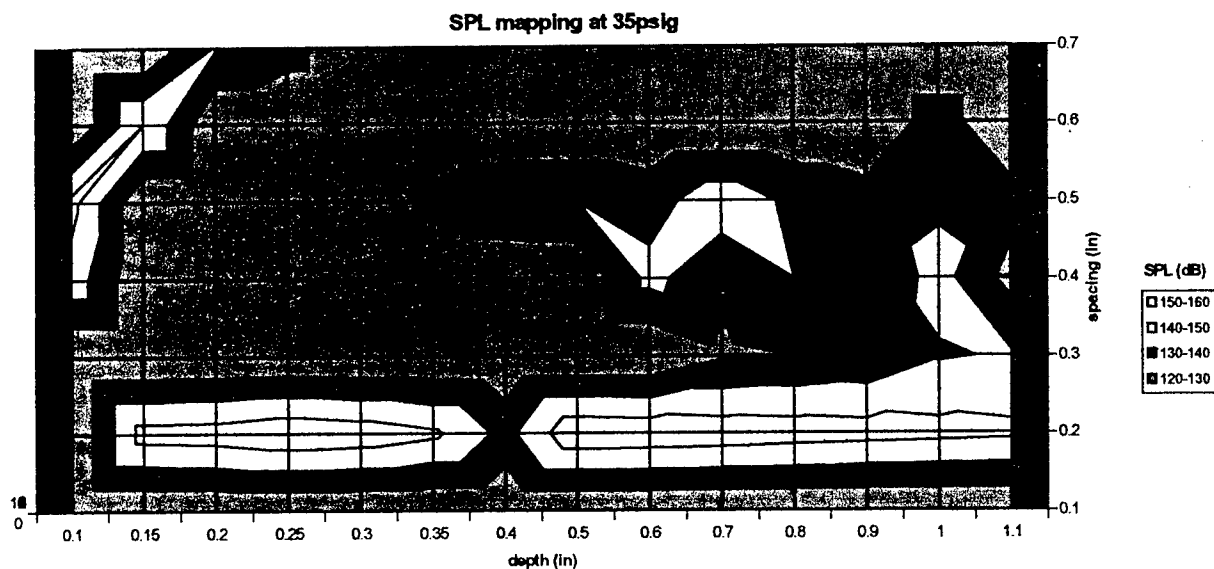


**Fig. 7.** Sound Pressure Level (SPL) mapping for various spacings (between the supply jet and the resonance tube) and resonance tube depths at a supply pressure of 35 psig.

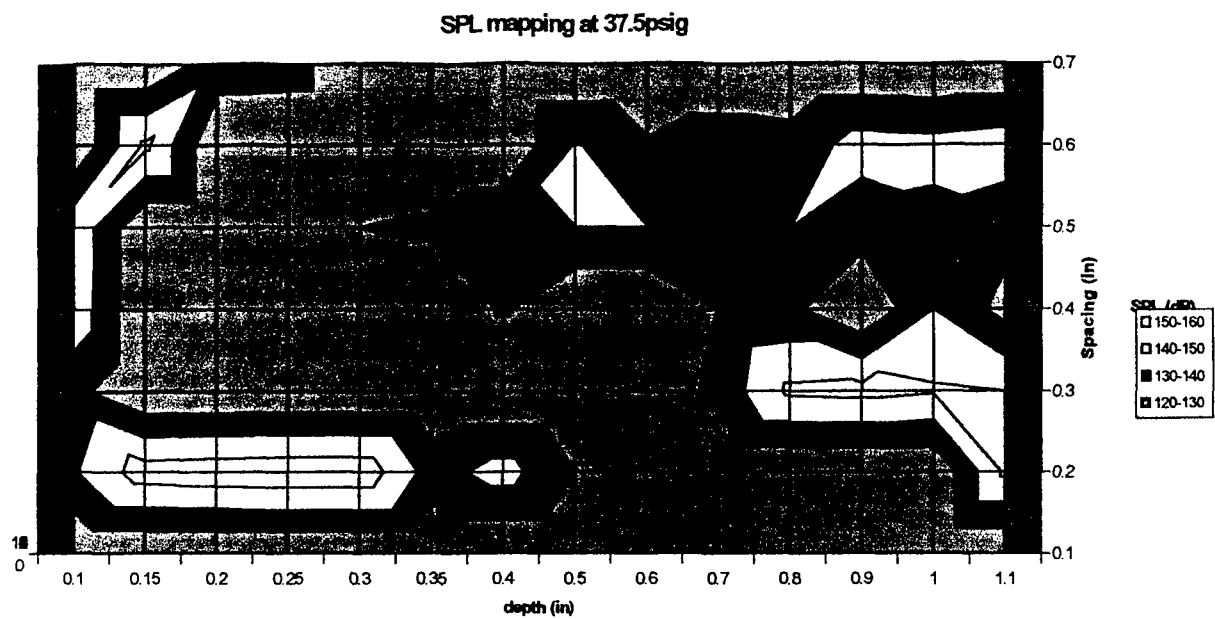


**Fig. 8.** Sound Pressure Level (SPL) mapping for various spacings (between the supply jet and the resonance tube) and resonance tube depths at a supply pressure of 37.5 psig.

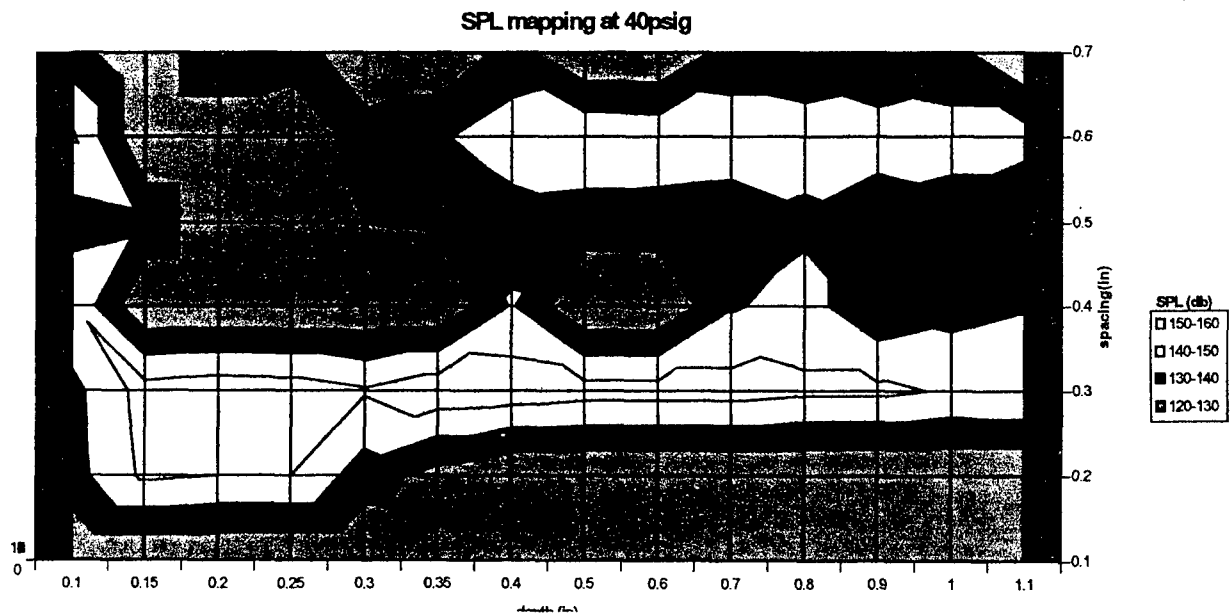


**Fig. 9.** Sound Pressure Level (SPL) mapping for various spacings (between the supply jet and the resonance tube) and resonance tube depths at a supply pressure of 40 psig.

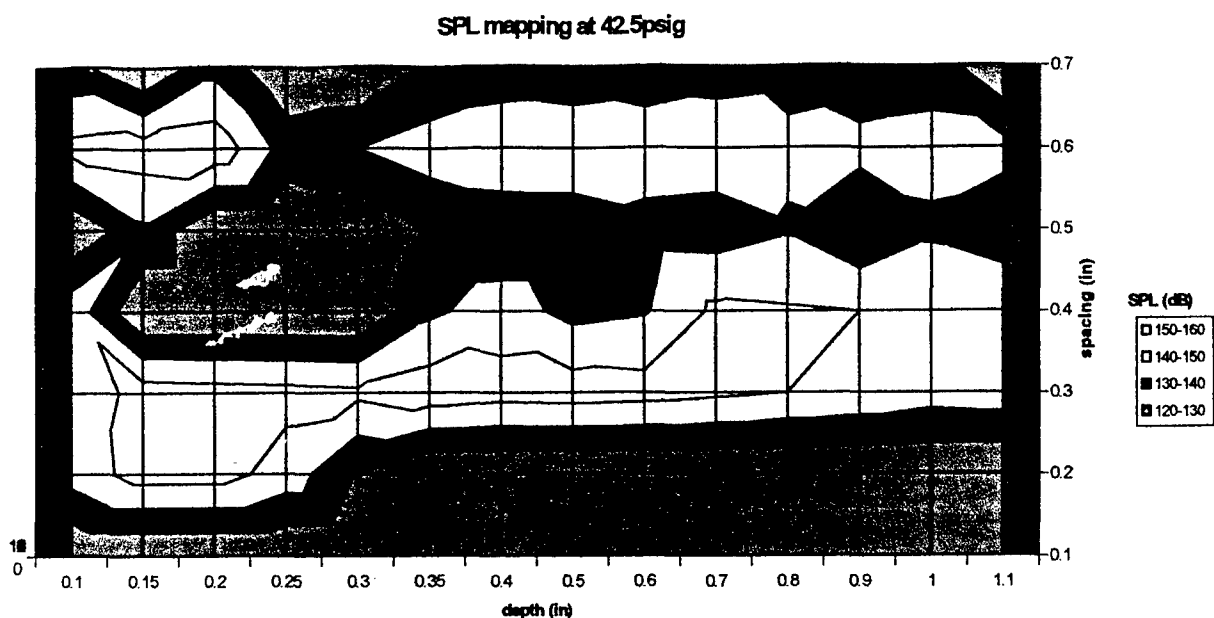


**Fig. 10.** Sound Pressure Level (SPL) mapping for various spacings (between the supply jet and the resonance tube) and resonance tube depths at a supply pressure of 42.5 psig.

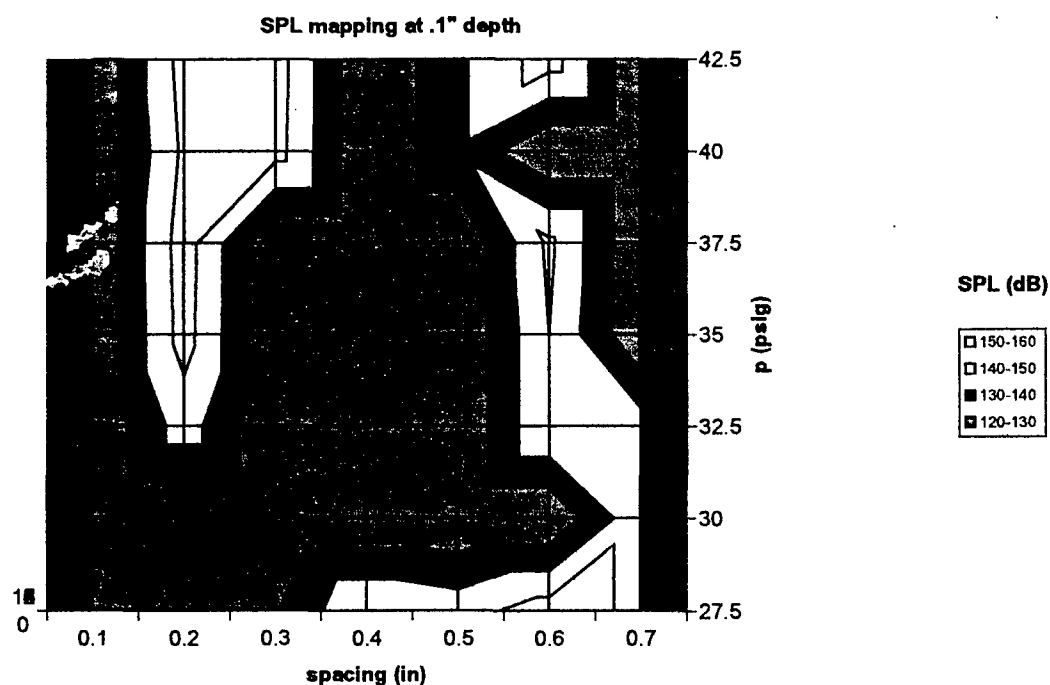


**Fig. 11.** Sound Pressure Level (SPL) mapping for various spacings (between the supply jet and the resonance tube) and supply pressures at a resonance tube depth of 0.1.

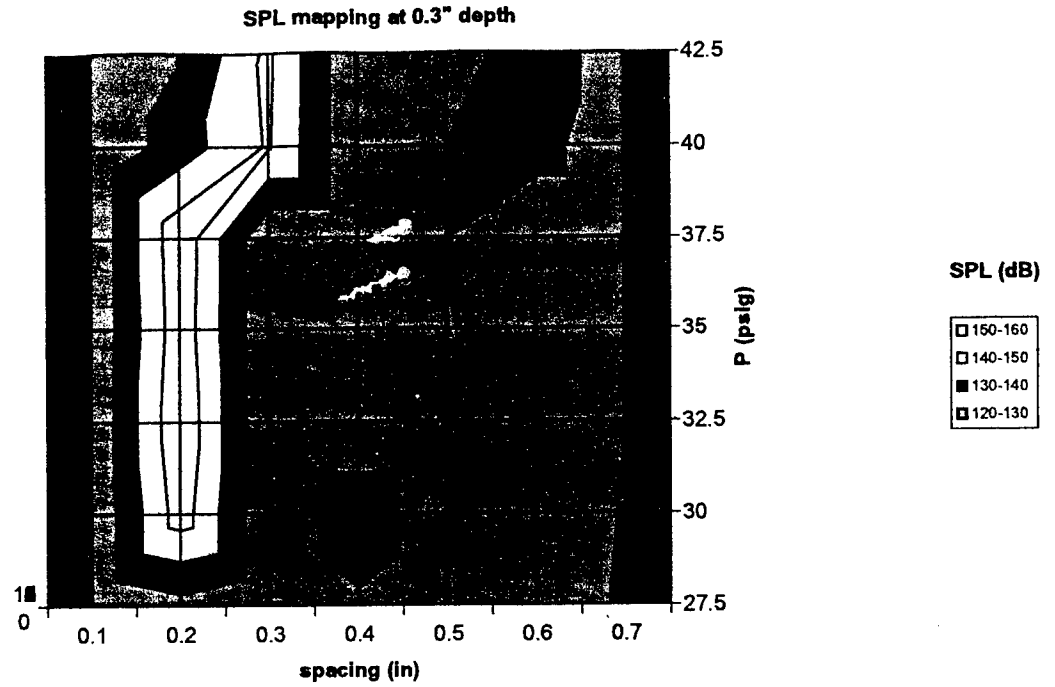


**Fig. 12.** Sound Pressure Level (SPL) mapping for various spacings (between the supply jet and the resonance tube) and supply pressures at a resonance tube depth of 0.3 inch.

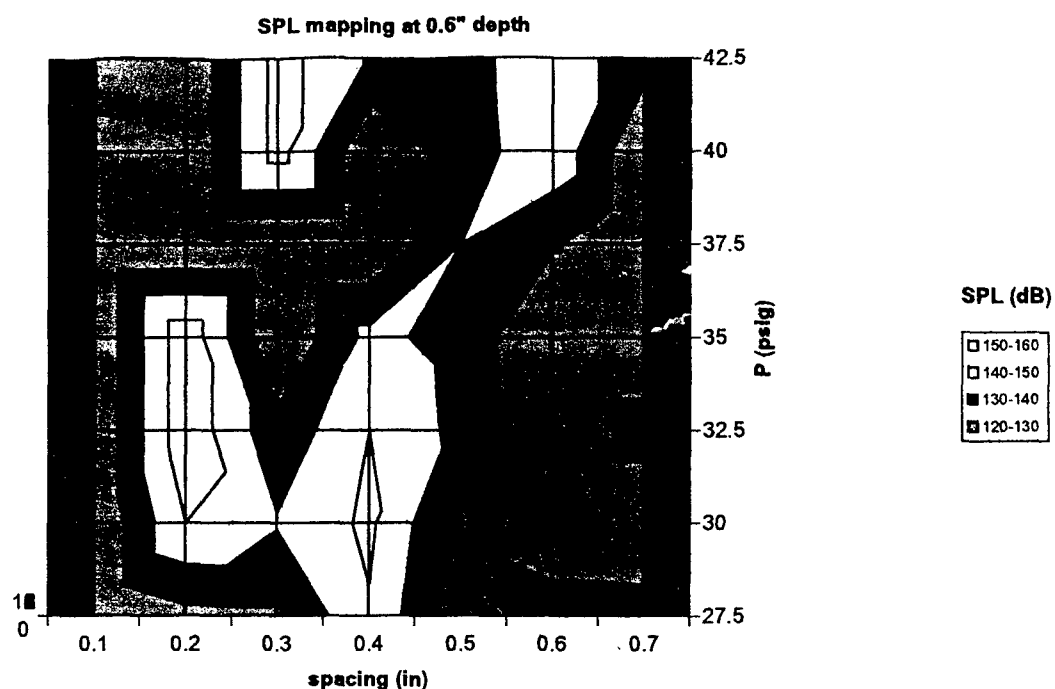


**Fig. 13.** Sound Pressure Level (SPL) mapping for various spacings (between the supply jet and the resonance tube) and supply pressures at a resonance tube depth of 0.6 inch.

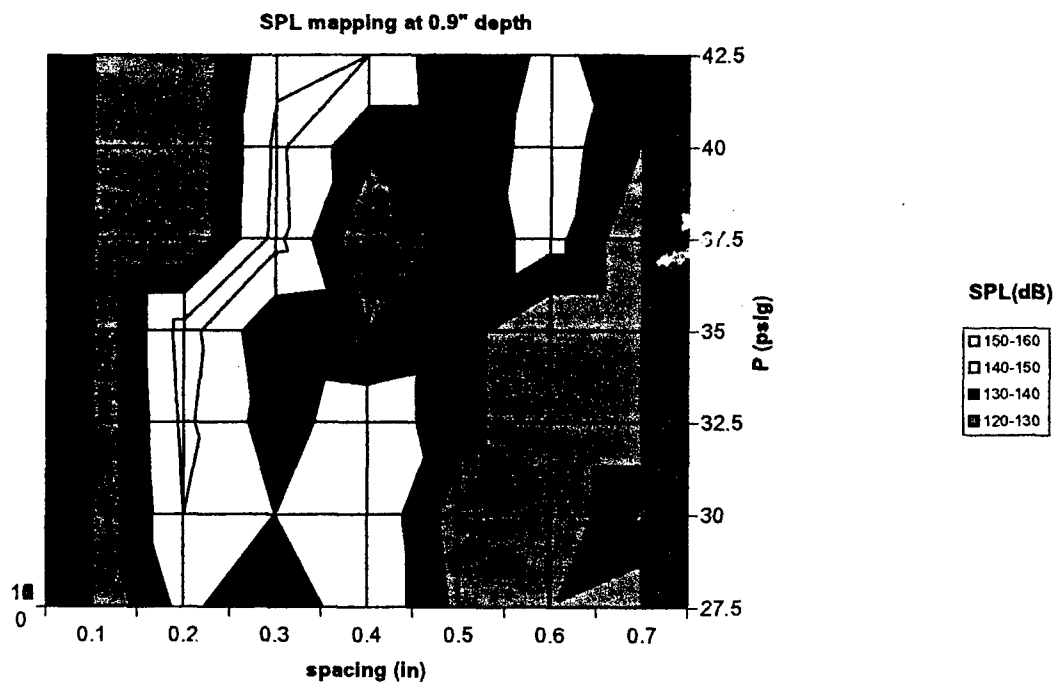


**Fig. 14.** Sound Pressure Level (SPL) mapping for various spacings (between the supply jet and the resonance tube) and supply pressures at a resonance tube depth of 0.9 inch.

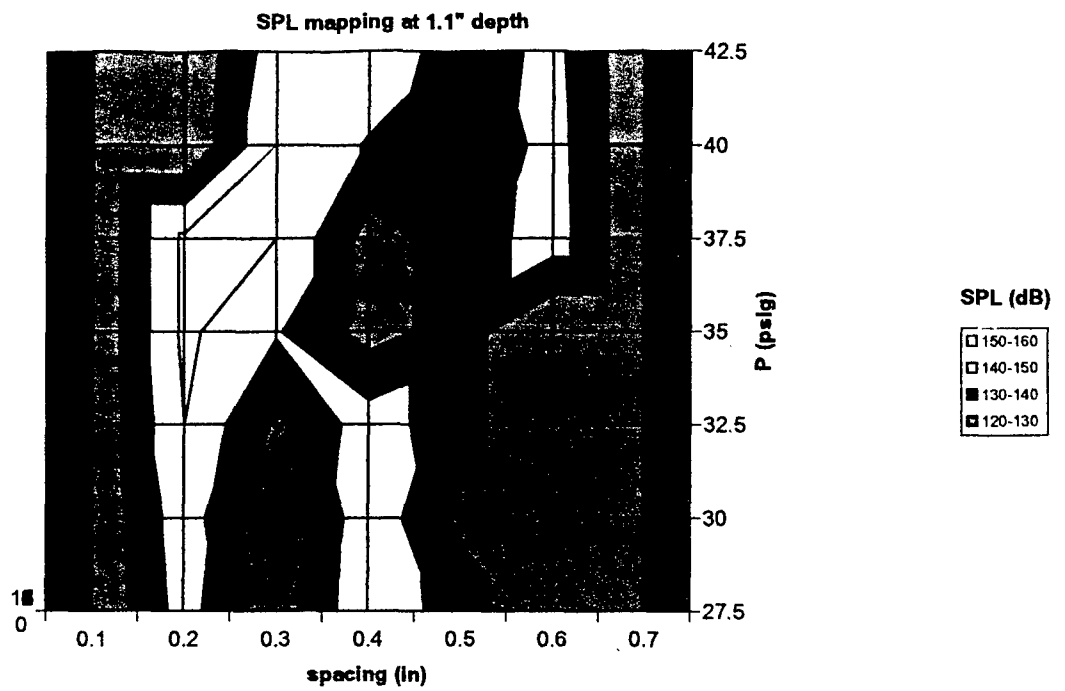


**Fig. 15.** Sound Pressure Level (SPL) mapping for various spacings (between the supply jet and the resonance tube) and supply pressures at a resonance tube depth of 1.1 inch.

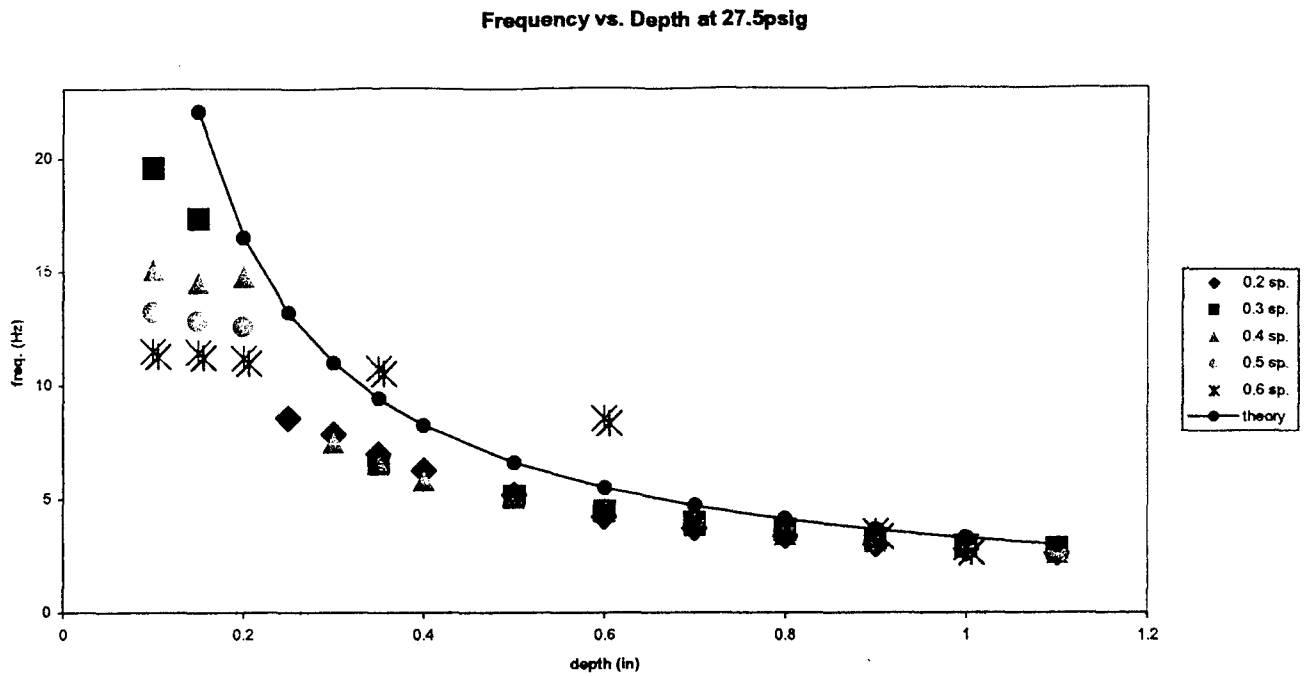


**Fig. 16.** Frequency vs. depth variation at 27.5 psig and various spacings.

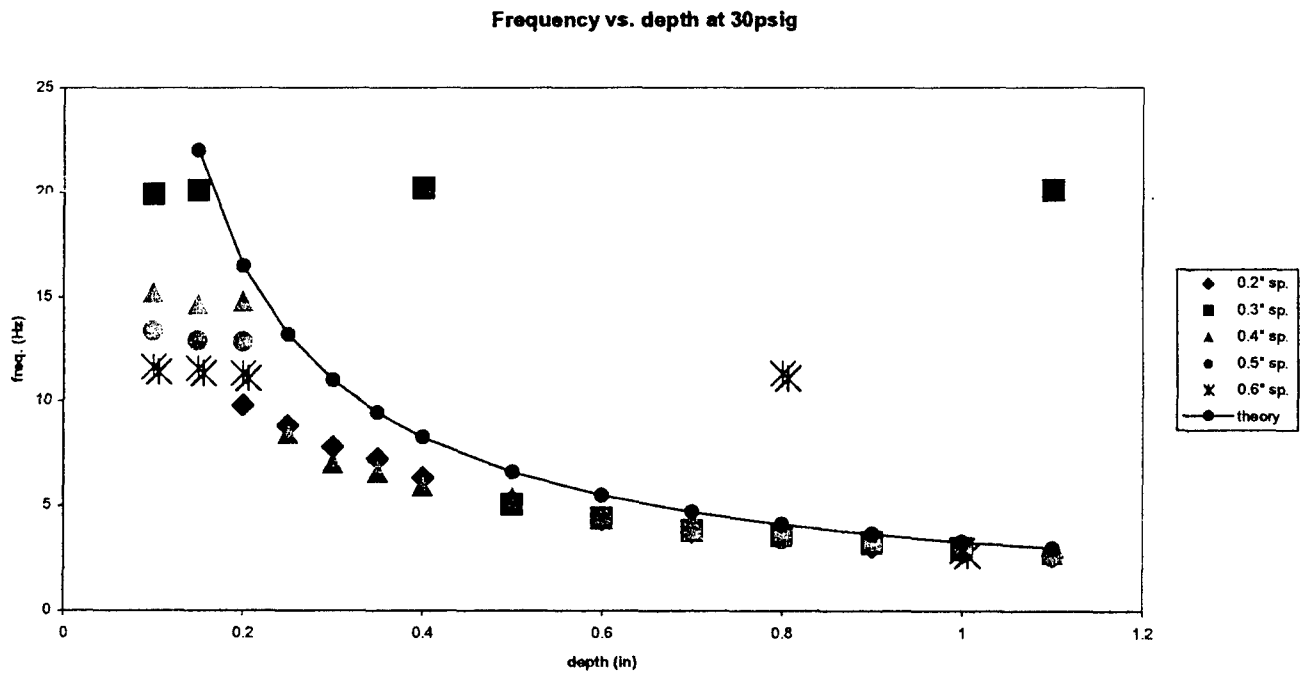


**Fig. 17.** Frequency vs. depth variation at 30 psig and various spacings.

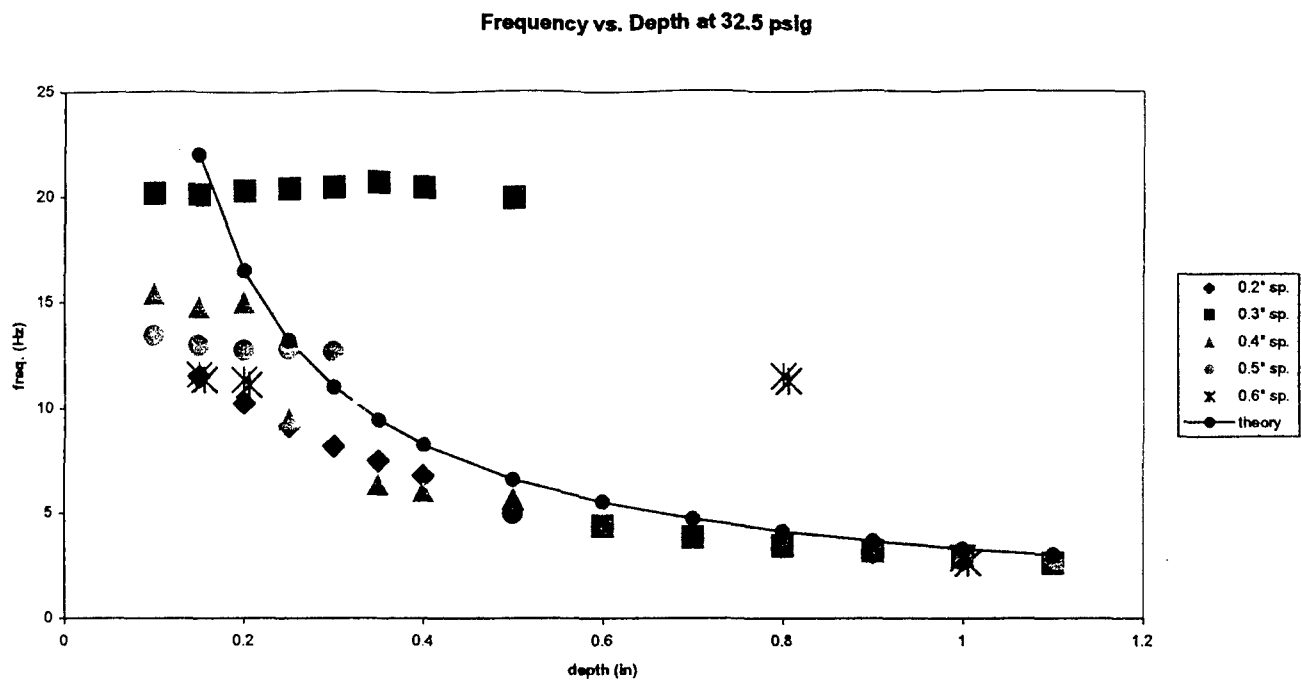


**Fig. 18.** Frequency vs. depth variation at 32.5 psig and various spacings.

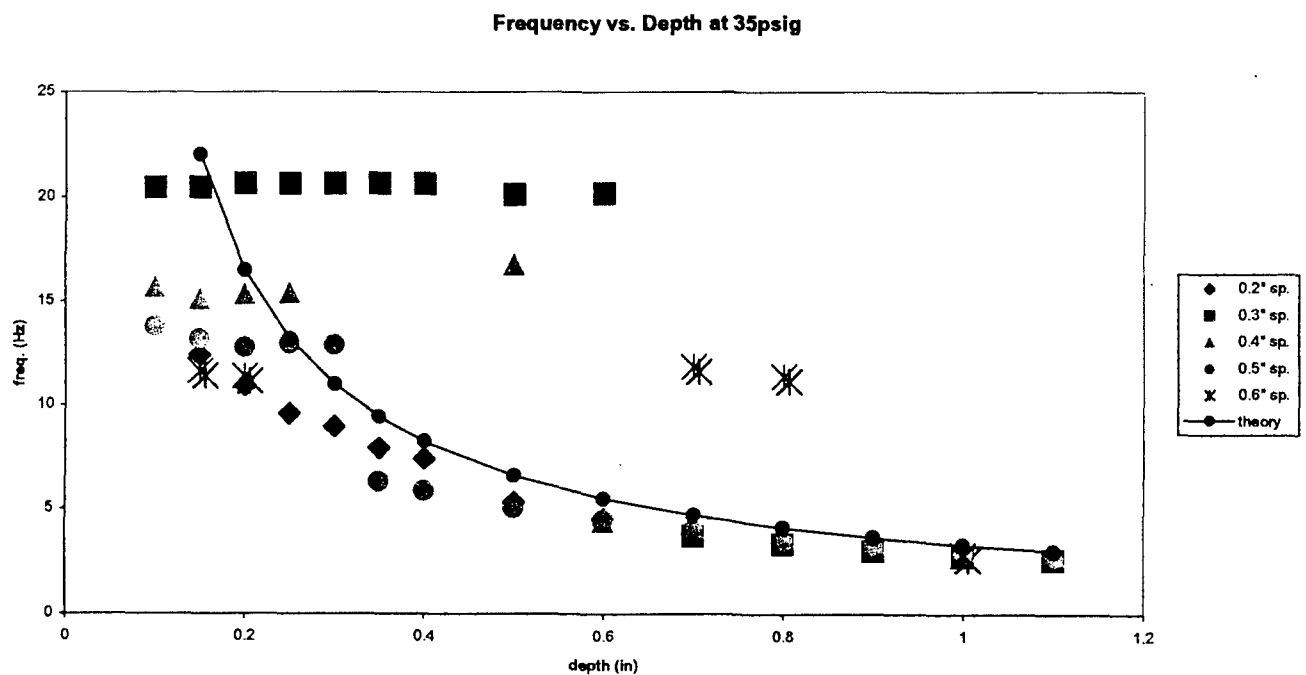


**Fig. 19.** Frequency vs. depth variation at 35 psig and various spacings.

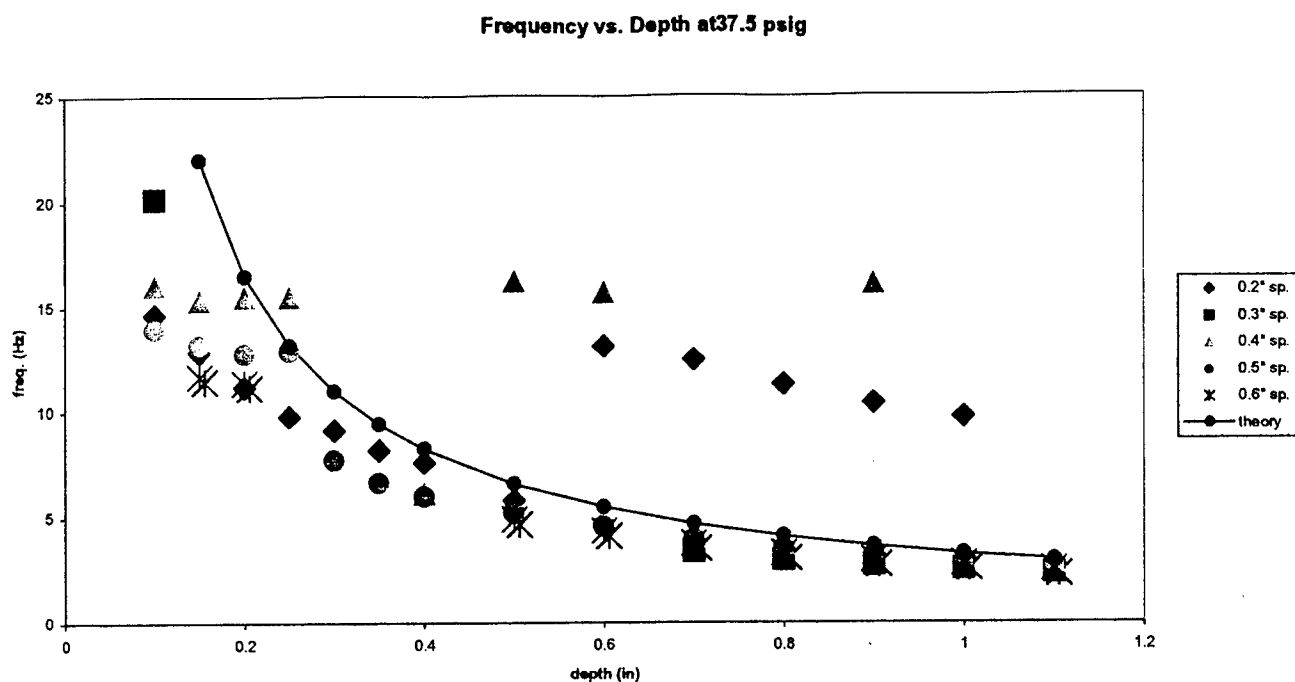


**Fig. 20.** Frequency vs. depth variation at 37.5 psig and various spacings.

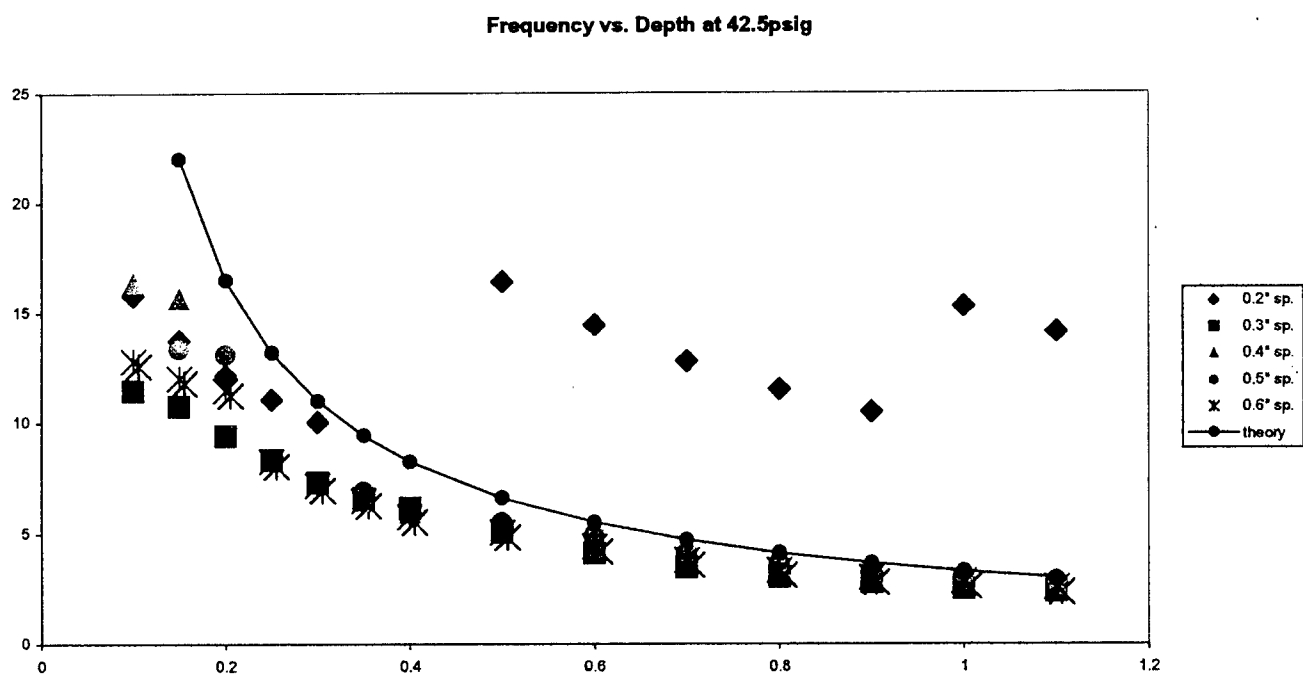


**Fig. 21.** Frequency vs. depth variation at 42.5 psig and various spacings.

**f vs d at .3" spacing and 37.5psi for 1/8" tube diameter**

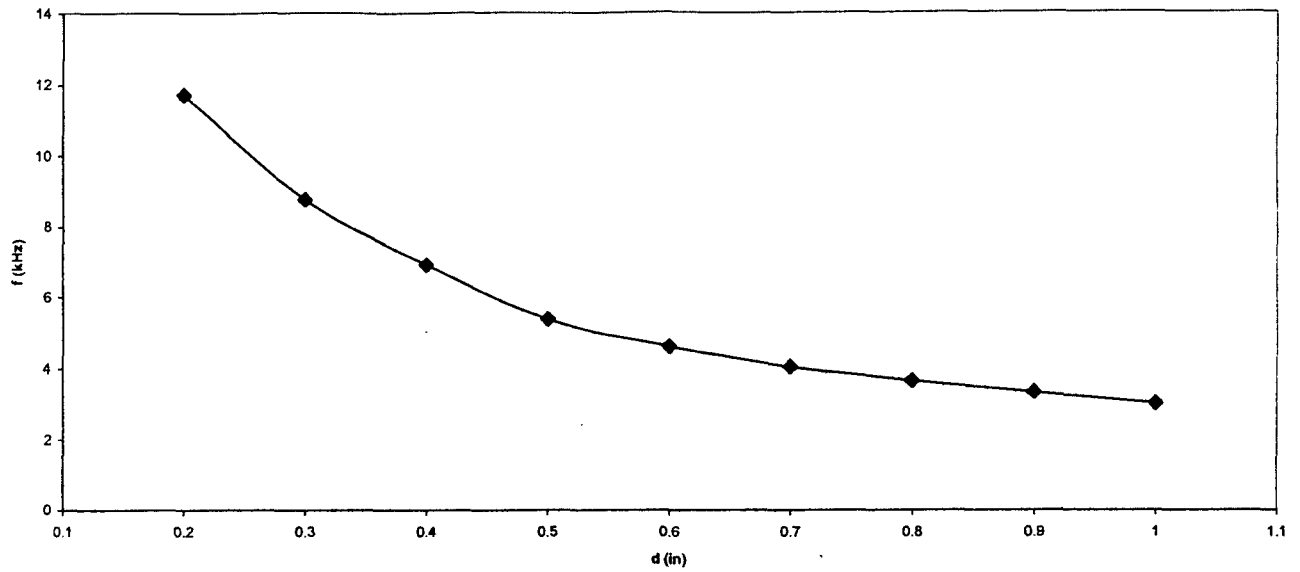


**Fig. 22.** Frequency vs. depth variation at 37.5 psig pressure, 0.3" spacing and 1/8" diameter.

**spl vs d for 1/8" tube, 37.5psi and .3" spacing**

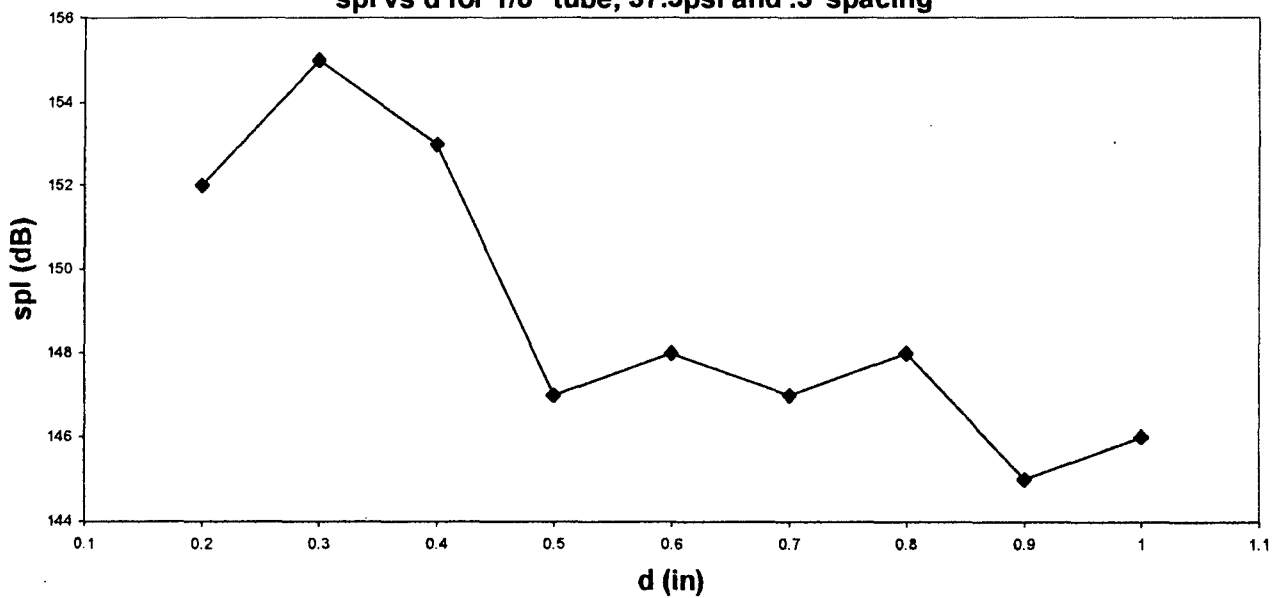


**Fig. 23.** SPL vs. depth variation at 37.5 psig pressure, 0.3" spacing and 1/8" diameter.

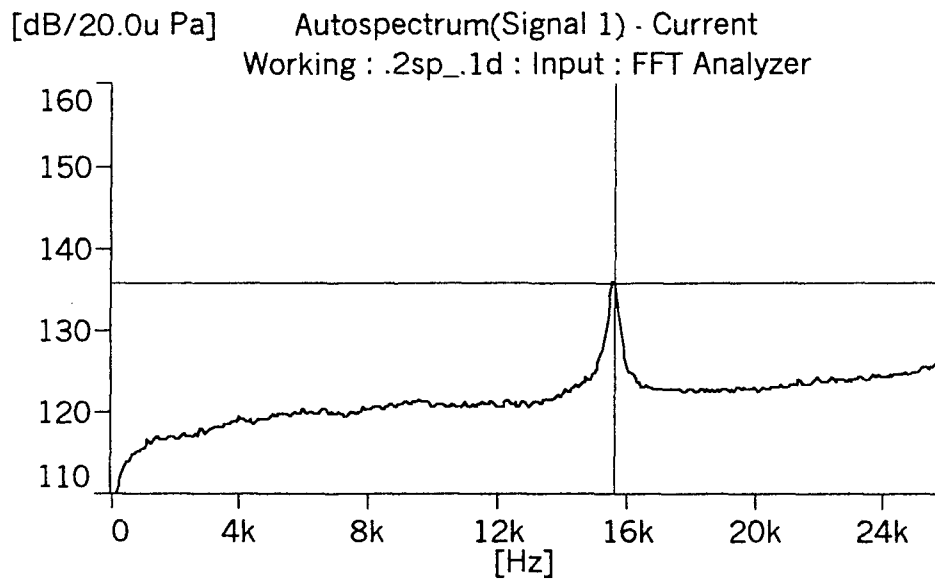


**Fig. 24.** Auto spectrum at 0.2" spacing, 0.1" depth and 40psig.

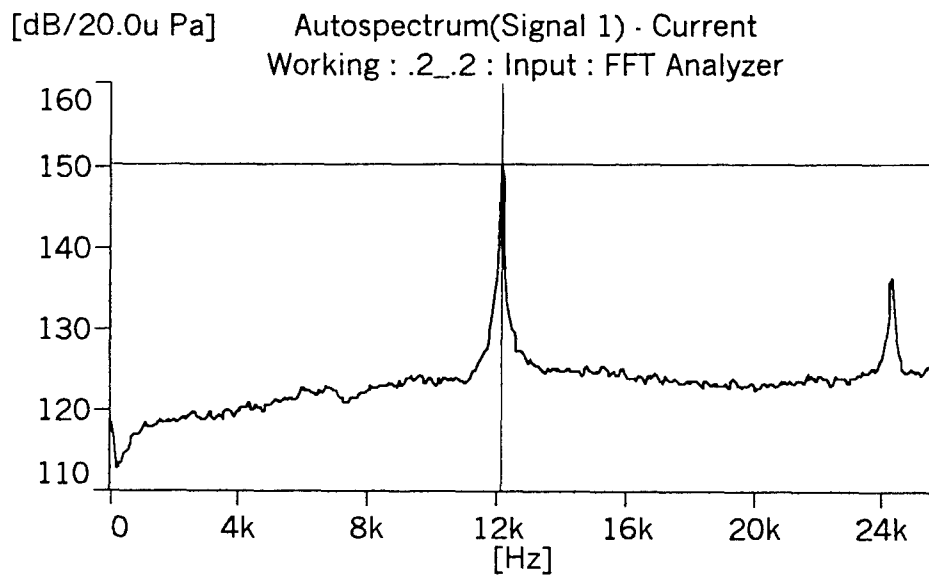


**Fig. 25.** Auto spectrum at 0.2" spacing, 0.2" depth and 40psig.

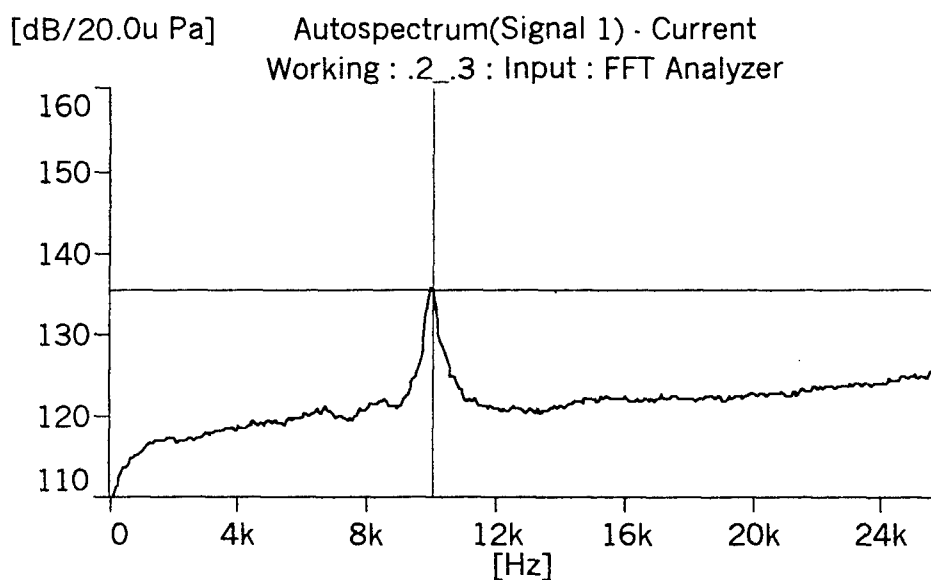


**Fig. 26.** Auto spectrum at 0.2" spacing, 0.3" depth and 40psig.

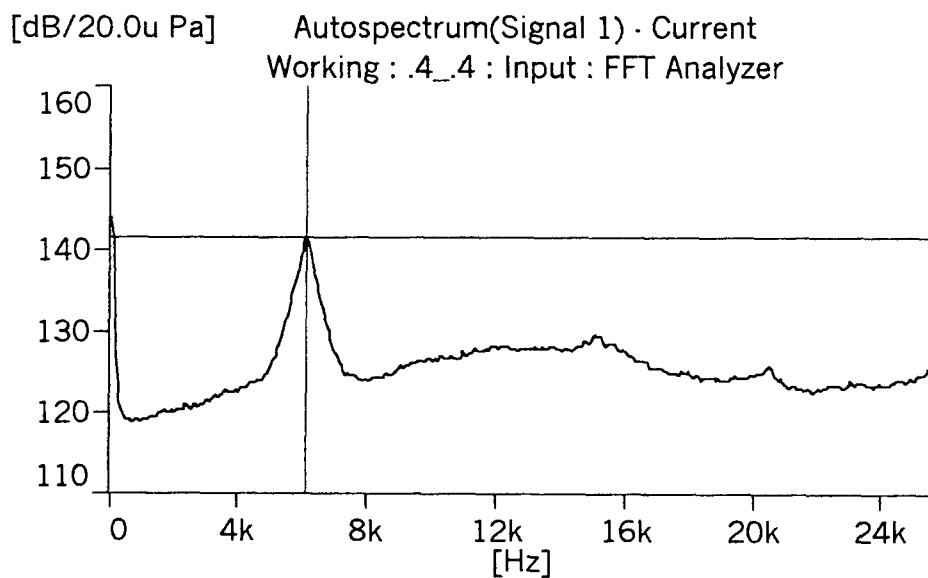


**Fig. 27.** Auto spectrum at 0.4" spacing, 0.4" depth and 40psig.

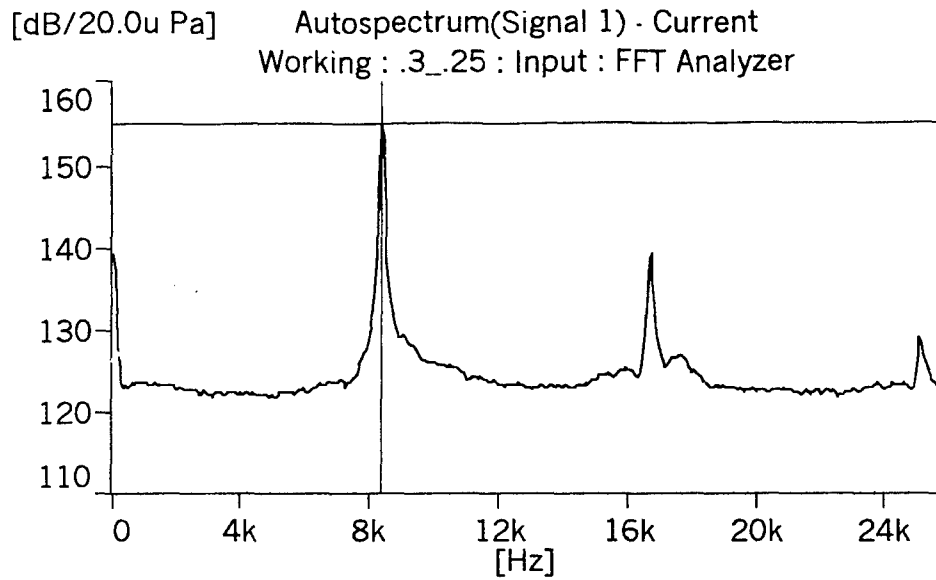


**Fig. 28.** Auto spectrum at 0.3" spacing, 0.25" depth and 40psig.

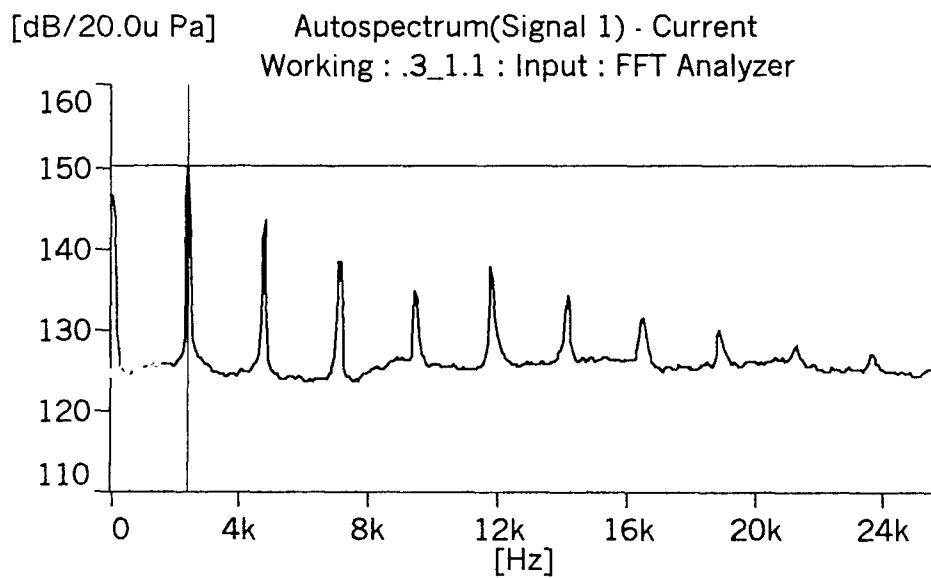


**Fig. 29.** Auto spectrum at 0.3" spacing, 1.1" depth and 40psig.

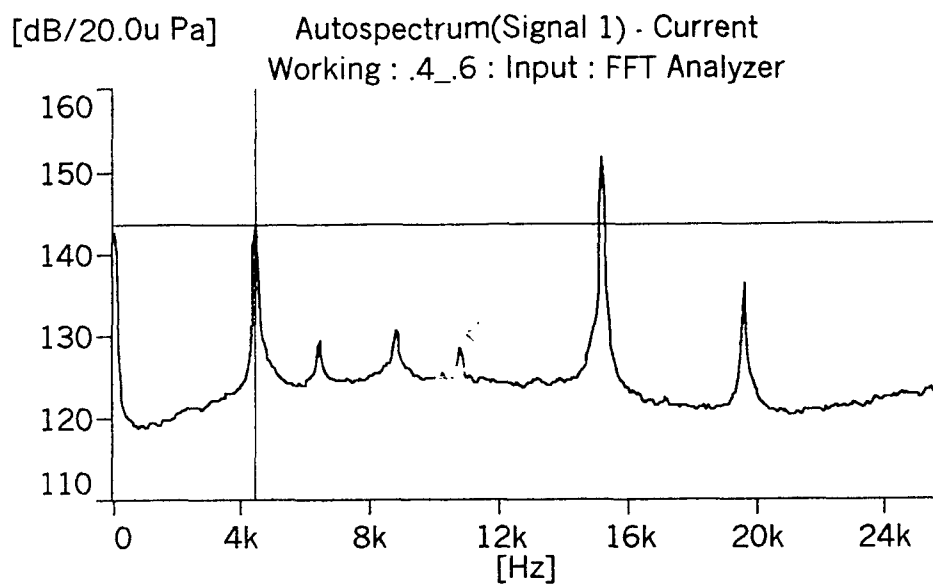


**Fig. 30.** Auto spectrum at 0.4" spacing, 0.6" depth and 35psig.

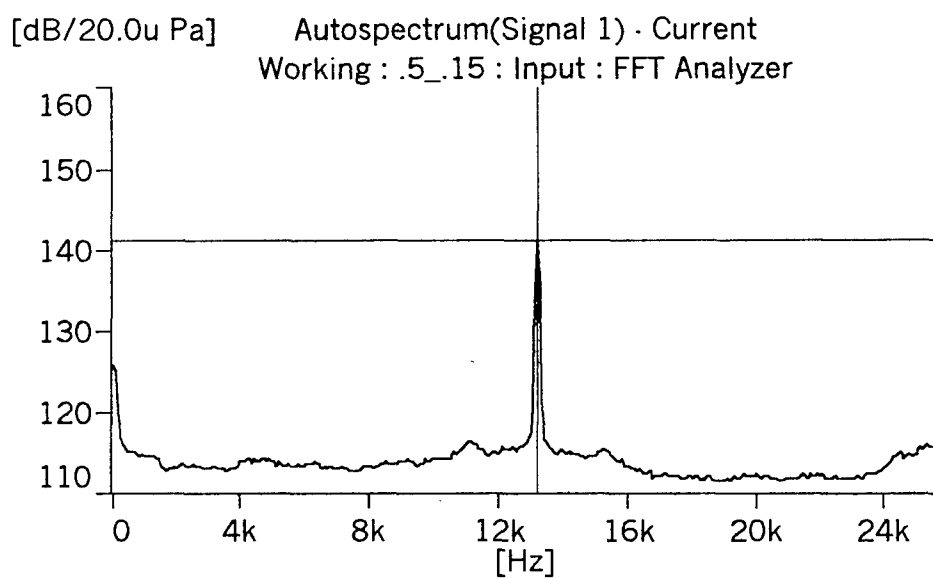


**Fig. 31.** Auto spectrum at 0.5" spacing, 0.15" depth and 35psig.

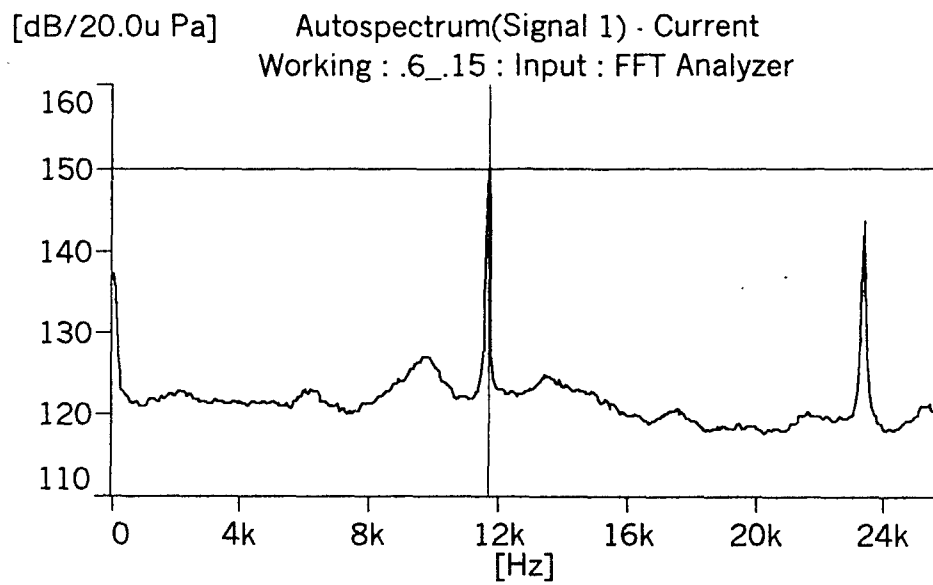


**Fig. 32.** Auto spectrum at 0.6" spacing, 0.15" depth and 35psig.

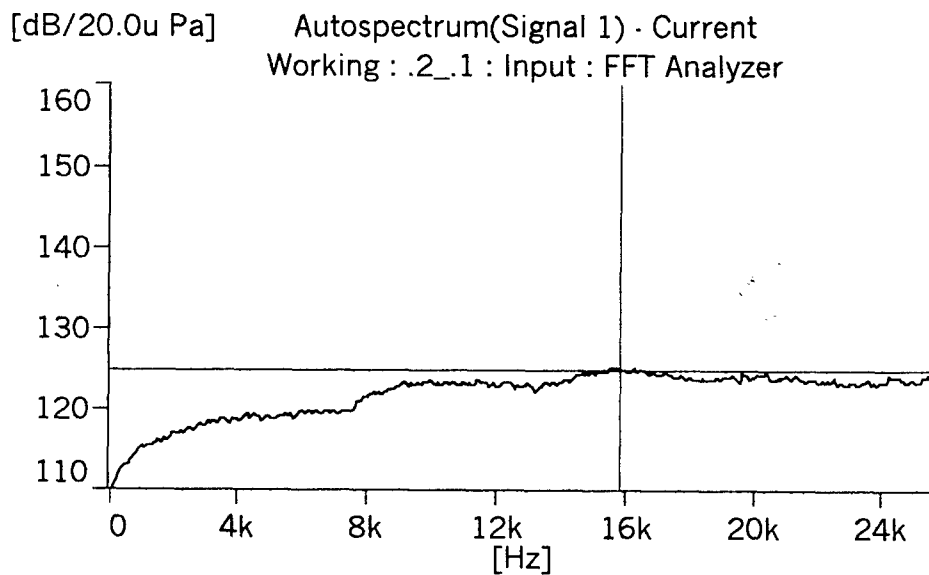


**Fig. 33.** Auto spectrum at 0.2" spacing, 0.1" depth and 30psig.

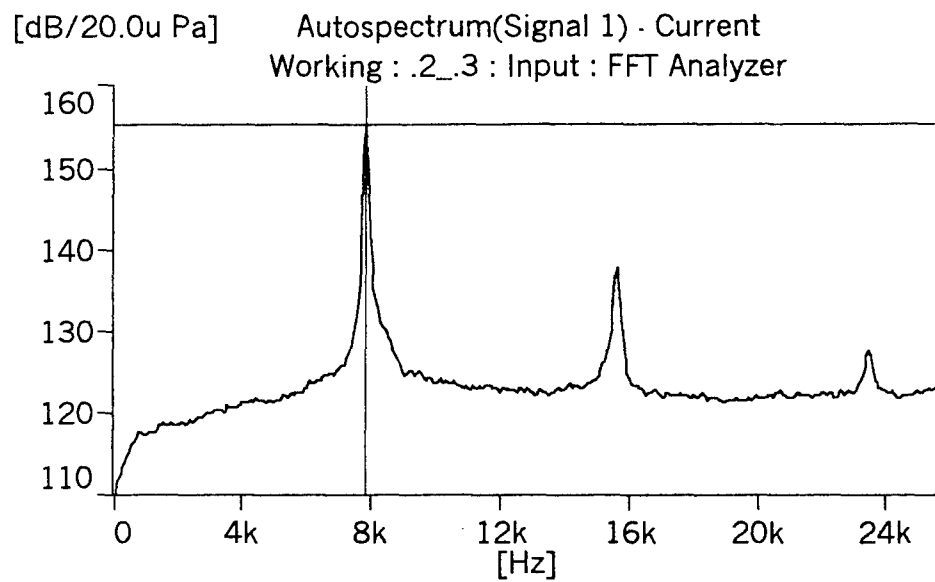


**Fig. 34.** Auto spectrum at 0.2" spacing, 0.3" depth and 30psig.

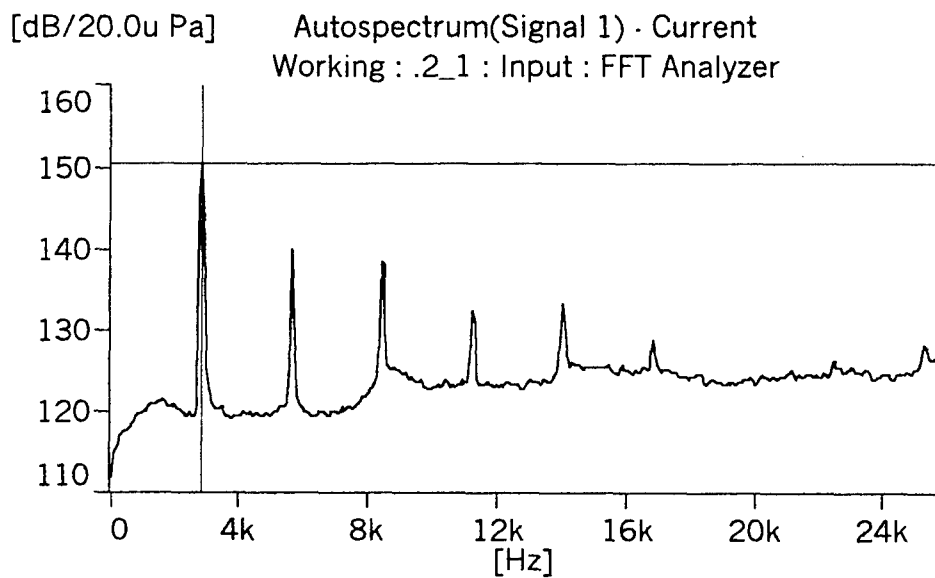


**Fig. 35.** Auto spectrum at 0.2" spacing, 1.0" depth and 30psig.

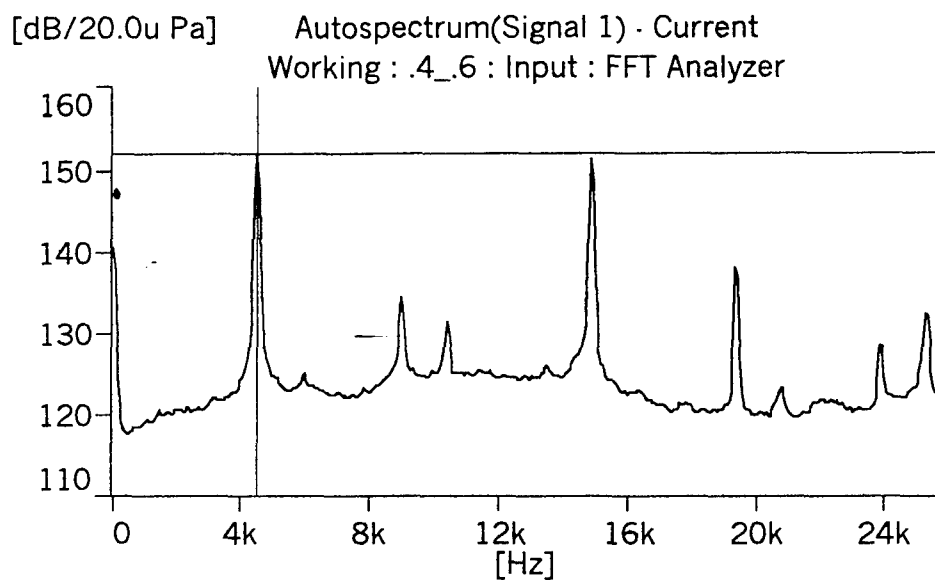


**Fig. 36.** Auto spectrum at 0.4" spacing, 0.6" depth and 30psig.

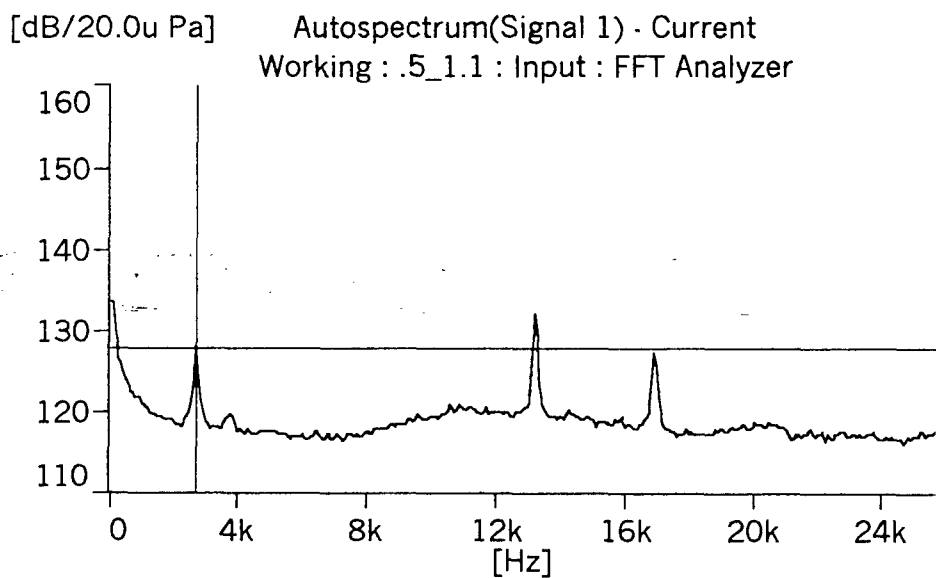


**Fig. 37.** Auto spectrum at 0.5" spacing, 1.1" depth and 30psig.